

https://dspace.org/

Classical and quantum entanglement: applications to quantum communication with structured photons

Ndagano, Bienvenu Irenge

2019
https://hdl.handle.net/10539/28904

Downloaded from a DSpace repository. https://dspace.org/

University of the Witwatersrand

Classical and Quantum Entanglement: Applications to Quantum Communication with Structured Photons

Author:
Bienvenu Irenge Ndagano
ORCID:
0000-0002-8063-6185

Supervisor:
Prof. Andrew Forbes
ORCID:
0000-0003-2552-5586

A thesis submitted in fulfilment of the requirements for the degree of Doctor of Philosophy

in the

School of Physics

13 March 2019



Declaration of Authorship

I, Bienvenu Irenge NDAGANO, declare that this thesis titled, 'Classical and Quantum Entanglement: Applications to Quantum Communication with Structured Photons' and the work presented in it is my own. I confirm that this work submitted for assessment is my own and is expressed in my own words. Any uses made within it of the works of other authors in any form (e.g., ideas, equations, figures, text, tables, programs) are properly acknowledged at any point of their use. A list of the references employed is included.

Signed: 

Date: 13 March 2019

Abstract

Generating, manipulating and sharing quantum states with maximal levels of entanglement are crucial steps when implementing quantum processes such as quantum key distribution, quantum teleportation or quantum computation. In this quest, realising entanglement in different degrees of freedom has opened avenues beyond the two-level quantum bit (qubit). Spatial modes, particularly those carrying orbital angular momentum (OAM), allow one to exploit the spatial properties of photons to realise high-dimensional entanglement. This is owing to their larger Hilbert space that allows one to pack more information onto photons. Interestingly, the exploration of entanglement in many degrees of freedom has led to a topical debate around the quantum nature of entanglement itself. Non-separability is a fundamental property of quantum entangled states. However it is not unique to quantum systems; classical states of light can exhibit non-separability in their degrees of freedom which, can then be said to be entangled. Due to the local nature of this entanglement, these classical correlations have come to be known as classical entanglement. Entanglement correlations are, however, fragile and susceptible to decay under the influence of external factors such as atmospheric turbulence or imperfections in optical fibres. Here we provide a toolbox to characterise entanglement dynamics, mitigate photon loss, and compensate for errors. On the characterisation aspect, we demonstrate for the first time, the equivalence of quantum and classical entanglement in a one-sided turbulent channel. By performing a state tomography of an entangled two-photon state and a classically entangled beam post-perturbation, we show that the decay of entanglement for both systems is identical. This opens the possibility for real-time measurement of the channel operator and mitigation of errors on the quantum state, using bright laser sources. This is complemented by a number of schemes to mitigate errors and losses incurred on the quantum state through the perturbing channel. (1) In a simulated quantum key distribution protocol, we demonstrate the effect of mode separation on the robustness of the protocol: the larger the separation in state space, the more robust the link. (2) Turbulence causes intermodal scattering and results in photon loss during post-selection of a particular subspace. We show that information scattered in a larger state space as a result of turbulence can be recovered by post-selecting higher-dimensional spaces. Using a theoretical model based on experimental observations, we provide bounds within which the scheme is effective, as well as an estimation of the efficiency of photon recovery. (3) We make use of the channel characterisation with bright classical light to implement a Procrustean filtering on entangled photons; that is, we perform local operations on the quantum state to increase its degree of entanglement. Unlike previous schemes, our filtering only requires the local operations to be performed on a single party in the entangled pair, as opposed to both. While this requires prior knowledge of the perturbed

state, the next scheme does not. (4) We demonstrate the concentration of entanglement by Hong-Ou-Mandel interference. We show that singlet Bell states can be distilled from an ensemble of pure states with near-zero levels of entanglement. The robustness of the filtering is such that the fidelities of the distilled states remain constant over a large range of turbulence conditions. (5) Lastly, we address the issue of photon loss arising from the nature of the detector in the context of quantum key distribution. We present a novel scheme to deterministically measure single photons in a high-dimensional space of classically entangled vector vortex modes. Our scheme, unlike common filter-based ones, does not suffer from dimension-dependent losses, allowing the sorting of vector vortex modes with, in principle, unit efficiency.

Acknowledgements

The work presented here is not only the fruit of years of work, it is also a testimony to the support I have had throughout. And while the results are fulfilling, the journey has been edifying. As such, I thank:

My supervisor Prof. Andrew Forbes. The number of years we have worked together has set me on a path to success, both personally and professionally. The perspective I have gained in the Structured Light Group is unique. I have had the singular honour to be part of a fantastic team that will certainly continue to flourish for many years to come.

My colleagues and collaborators. Working side-by-side with you all has shaped my journey and enabled this work.

My parents, siblings and friends. For your neverending support throughout the years, I am grateful to you all for being such an important part of my life.

Last but not least, I want to acknowledge the following entities for making this work a reality with their financial support: the **Maria-Mater Misericordiae Fondatio**, the **National Research Foundation of South Africa**, the **University of the Witwatersrand** and the **African Laser Centre.**

Contents

Declaration of Authorship i

Abstract ii

Acknowledgements iv

Contents v

List of Figures vii

List of Tables xiii

List of Publications xv

1 Introduction 1
- 1.1 The quantum bit . . . 2
- 1.2 The spatial qubit . . . 6
- 1.3 Entangled spatial modes . . . 9
- 1.4 Is entanglement intrinsically quantum? . . . 10
- 1.5 Classical entanglement . . . 11
- 1.6 Outline . . . 14

2 Tailoring and measuring classically entangled states 16
- 2.1 Generation of classically entangled light . . . 17
  - 2.1.1 Dynamic phase control . . . 17
  - 2.1.2 Geometric phase control . . . 18
  - 2.1.3 Vector mode decomposition . . . 20
- 2.2 Quantum state tomography . . . 22
- 2.3 Quantum state tomography of a single qubit . . . 24
- 2.4 Tomography of quantum entangled spatial modes . . . 28
- 2.5 Classical implementation of quantum state tomography . . . 30
- 2.6 Conclusion . . . 32

3 Characterising quantum channels with classically entangled light 33

3.1 The equivalence of classical and quantum entanglement . . . 34
3.2 Channel tomography with classically entangled light . . . 35
3.3 Decay of classical entanglement in turbulence. . . . 37
3.4 Experimental realisation . . . 38
3.4.1 Classical and quantum setup . . . 38
3.4.2 Modelling atmospheric turbulence . . . 39
3.5 Entanglement decay in turbulence . . . 40
3.6 Conclusion . . . 42

4 Mitigating information loss in quantum key distribution with entangled photons through turbulence 45
4.1 Quantum key distribution with entangled photons . . . 47
4.2 Turbulence-induced decay of QKD fidelity . . . 49
4.2.1 Theoretical model . . . 49
4.2.2 Experimental realisation . . . 50
4.3 Effect of mode separation on the QKD fidelity . . . 52
4.4 Mitigating information loss . . . 54
4.4.1 Recovery of information in additional subspaces . . . 54
4.4.2 Conversion of noise to losses . . . 57
4.5 Conclusion . . . 60

5 Entanglement concentration by Hong-Ou-Mandel interference 62
5.1 The concept . . . 63
5.2 Experimental realisation . . . 65
5.2.1 Production of antisymmetric states . . . 65
5.2.2 Calibration of the Hong-Ou-Mandel filter . . . 66
5.3 Tomography of the distilled states . . . 67
5.4 Conclusion . . . 71

6 A deterministic detector for vector vortex modes 72
6.1 High dimensional encoding with vector vortex modes . . . 73
6.2 Deterministic detection . . . 75
6.3 Deterministic and filter based detection . . . 78
6.4 Application to quantum key distribution . . . 80
6.5 Conclusion . . . 83

7 Conclusion 84

Bibliography 88

List of Figures

1.1 Intuitive description of the Poincaré sphere. (a) Control over the amplitude parameter θ allows one to continuously change the position of the qubit (indicated by the arrow) on the unit circle, resulting in a change of the relative amplitudes of left- and right-circular polarisation states. (b) Control over the phase parameter φ allows one to continuously rotate the qubit state at different positions around a circle at fixed relative amplitude between the basis states (fixed θ). This is demonstrated for $\theta = \pi/2$. (c) Simultaneous control of phase and amplitude results in a description of the general qubit in Eq. 1.2 on a unit sphere where the poles are the basis polarisation states. 3

1.2 Elementary rotations on the surface of the Poincaré sphere. The qubit state, indicated by the position vector (red arrow), can be rotated on the surface of the sphere about the (a) x-axis, (b) y-axis and (c) z-axis. 6

1.3 (a) Intensities and (b) phase-maps of OAM modes carrying, from left to right, $\ell = -3,\ -2, \cdots,\ +2$ and $+3$ units of OAM. 7

1.4 Bloch sphere description of an OAM qubit with $\ell_1 = -\ell_2 = 1$. Control over the amplitude parameter θ and phase parameter φ as shown in (a) and (b) respectively, leads to (c) a description of an arbitrary OAM qubit on the OAM sphere. 8

1.5 Description of qubit pairs on the higher-order Bloch sphere. States on the surface of the higher-order Bloch sphere are constructed from the tensor product of qubit states from two Bloch sphere, each describing a subsystem (photon). Depending on the way in which the eigenstates combine at the poles, one can construct two higher-order Bloch spheres for a system of qubit pair. 10

1.6 (a) Intensity and polarisation map of some vector beams. The non-separability of the space and polarisation degrees of freedom is reflected in the space variant (inhomogeneous) polarisation. (b) The non-separability of the two degrees of freedom manifests itself if one passes the beam through a rotating linear polariser and measures the resulting spatial mode on a camera, as shown here for two vector beams. 12

1.7 Description of hybrid states on the HOPS. States on the surface of the HOPS are constructed from the tensor product of OAM states from the Bloch sphere and polarisation states from the Poincaré sphere. Here, each sphere describes a degree of freedom. Depending on the way in which the eigenstates combine at the poles, one can construct two HOPS for a system of hybrid qubit states. The equator represents maximally entangled states whereas the poles represent non-entangled states. 13

2.1 An incident polarised laser beam is spatially divided in horizontal and vertical polarisation components using a polarising beam splitter (PBS), each of which is modulated by a single hologram encoded on an SLM, placed inside a Sagnac interferometer. The dove prism (DP) ensured that the two OAM modes produced have opposite charge ℓ. BS: 50:50 beam splitter; HWP: half-wave plate; QWP: quarter-wave plate. H, H', V and V' denote the polarisation paths before and after the SLM. 18
2.2 Experimental Modal decomposition of vector vortex modes in the $\ell = \pm 1$ subspace. Vector modes produced with a half-wave plate($\lambda/2$) and q-plate (qp) are analysed with a vector mode decomposition system. The measurement outcomes are collected at detectors D_1 to D_4 placed after polarisation beam-splitter (PBS). M1 and M2 are mirrors. 21
2.3 A QST attempts to reconstruct a potentially complex quantum state by a series of simple projective measurements. This is analogous to trying to reconstruct a complicated object by only considering its shadow from various angles. 23
2.4 (a) Representation of polarisation states on the Poincaré sphere. (b) Shows the normalised outcomes of projective measurements onto the eigenstates of the Pauli matrices, for given horizontally polarised state. (c) Representation of OAM qubit states on the OAM Bloch sphere. (d) From projective measurement onto spatial modes, one performs the quantum state tomography of an OAM state $(|1\rangle + |-1\rangle)/\sqrt{2}$. 27
2.5 Quantum state tomography of a two-photon state. (a) shows an experimental setup to generate entangled two-photon states through spontaneous parametric down-conversion in a non-linear crystal (NLC). The down-converted photons travel to two OAM analysers and their quantum states are measured in coincidence. (b) Shows a two-qubit QST where the projected state of each photon in the entangled pair is indicated by their phase map. The colour of each box represents the normalised coincidence counts for a given set of projection on the two-photon state. Using the tomographic data, the density matrix is computed and its real and imaginary components are shown in (c) and (d). The sum of the measurements enclosed by the red squares define the expectation value of the identity (probability conservation) 29
2.6 State tomography of a classical vector beam. (a) Shows the projective measurements on the polarisation and spatial mode degrees of freedom. (b) From these projections, the density matrix is reconstructed. 31

3.1 Illustration of the concept. (a) Alice generates two entangled photons using a SPDC process, and sends one photon (Photon A) to Bob through a free-space turbulent channel, which affects the quantum correlations due to perturbations to photon A. (b) Equivalently, Alice sends information to Bob using a classically entangled bright light field (laser beam). The spatial DoF (DoF A) is affected by the channel, while the polarisation (DoF B) is not. APD = avalanche photodiode, BBO = Beta Barium Borate (non-linear optical crystal), SLM = spatial light modulator and CCD = charge coupled device. 35

3.2 Experimental setup. (a) The entangled qubits were encoded using a q-plate and propagated through the turbulent conditions simulated with single Kolmogorov phase screens. The output state was analysed using a vector mode sorter that performs a decomposition into vector states. (b) Full state tomography of the perturbed state was performed by projecting polarisation states, selected with the quarter or half-wave plate, onto OAM states encoded on a spatial light modulator. The output of the projections were observed in the far-field using a camera. (c) Vector vortex modes are (de)multiplexed using two Mach-Zehnder interferometers, with the q-plates used to (de)encode hybrid qubits. 39

3.3 Evolution of classical entanglement in turbulence. (a) The measured concurrence variation after propagation through turbulence screens of various SR strengths (increasing from high to low SR values) for the classical (red markers) and quantum (blue markers) states, correctly follow the theoretical prediction for one of two entangled photons going through a turbulent channel (green dashed line). The fluctuations in SR arise from the statistical averaging of the turbulence screen for an encoded SR value. The inset shows the decay in fidelity of the output state with respect to a maximally entangled state, as a function of the turbulence strength. (b) The measured concurrence obeys the predicted linear mapping to the concurrence of the input state. Here we have shown this for three channels with SR = 1.00, 0.70 and 0.45. The error bars represent the standard errors in the averages over the multiple turbulence realisations. 41

3.4 Evolution of the mode spectrum in turbulence. (a)-(e) Show vector mode dispersion for the four vector vortex modes of the $|\ell| = 1$ subspace for average SR values of 1.0, 0.7, 0.5, 0.4 and 0.3 respectively. The matrices show the evolution of the power distribution among the four vector detector for a given input mode. (f) and (g) Show the effect of the turbulence on the spatial DoF, measured by modal decomposition of the $|-1\rangle|L\rangle$ and $|1\rangle|R\rangle$ input qubit states, respectively. The scattering of the OAM eigenstates is observed through a redistribution of energy between OAM modes with increasing SR. 42

3.5 Experimental results for data transmission over turbulent channel. (a) Using a four-bit encoding technique with four multiplexed vector modes, a 425×513 pixels image of Maxwell was transmitted through a turbulent channel with SR = 0.3, and demultiplexed at the receiver's end. A threshold at 15% of the maximum received signal was applied to the data to filter noise signals. By characterising the channel with a full tomography of the classically entangled light, we obtained (b). (c) The channel perturbation resulted in a distorted image at the receiver's end with a correlation coefficient of 64.2%. (d) Correcting the image with the inverse channel matrix increased the correlation coefficient to 98.9%. . . . 43

4.1 (a) Alice generates a pair of entangled photons (A and B) using a pumped non-linear crystal (NLC) and sends one of the photons to Bob through a turbulent channel. Alice and Bob enact a quantum key distribution protocol, whereby they perform joint measurements on the photon pair using spatial light modulators (SLMs) in order to build the key. (b) Shows the experimental realisation where one SLM is used to encode the spatial projections of both Alice and Bob. Turbulence is encoded as a phase screen, superimposed on the tomography holograms as shown on the inset. The plane of the BBO crystal was relayed onto the SLM and then the fibers using 4f imaging systems. F = 10 nm bandpass filters; L1 = 10 mm; L2 = 750 mm; FC = fiber coupler with 2 mm focal length lens integrated; SMF = single mode fiber; DM = dichroic mirror. 47

4.2 Fidelity decay in turbulence. Alice and Bob perform joint measurements on the two-photon state for an entanglement based six-state protocol with OAM states carrying $\hbar$ of OAM per photon. These tomographic measurements are shown (a) in the absence of turbulence (SR = 1) and (b) in the presence of turbulence with SR = 0.5 for a mode size $\omega_0 = 800$ μm. The regions enclosed by the red dashed lines (top left corner) show the measurements required for the traditional BB84. (c) Shows both the simulated and experimental measurements of the decay of fidelity as a function of turbulence for OAM states with $|\ell| = 1$ and post-selected beam width $\omega_0 = 200$ μm. 51

4.3 a) Simulated measurement of fidelity decay as a function of turbulence for OAM states with $\ell = 2$, 4, 6, 8, 10 and 20. The minimum secure key rate $R_{\min} = 0$ is attained for a fidelity of 0.89, while the mutual information I_{AB} vanishes for $F = 0.5$. b) Simulated measurement of fidelity decay as a function of turbulence for OAM states with $\ell = 2$, 4, 6, 8, 10 and 20 with the modes all renormalised to the same size. 53

4.4 Recovering information in higher OAM subspaces. (a) To increase photon recovery during QKD, Bob uses a quantum router to separate photon states according to their parity, and post-selects two OAM subspaces: $|\ell| = 1$ and $|\ell| = 2$. (b) Shows the measurement fidelity of Alice and Bob, normalised to each of the two subspaces (dotted blue line). The range of turbulence parameter b for which information recovery is still possible is shown as the green shaded region enclosed by the R_{max}, R_{min} and the fidelity curve. (c) Shows the impact of turbulence on the relative photon detection probability in two measuring subspaces for Alice and Bob. . . . 56

4.5 Noise to loss conversion scheme with classical light. (a) Single photons, together with a bright classical beam are sent through the same channel and analyzed separately. A state tomography of the classical beam is performed to reconstruct the channel operator. The classical data are subsequently used to perform a Procrustean filtering on the quantum state in real-time. (b) The detection fidelity is computed from the measured two-photon density matrix in the presence of turbulence (uncorrected data). The channel matrix is reconstructed using a bright classical source and used to engineer a filter that cancels out the effect of turbulence, increasing the fidelity to unit (corrected). 59

5.1 Experimental setup for entanglement distillation. By pumping a 3 mm thick, non-linear type-I BBO crystal with a 355 nm laser, we produced through SPDC, pairs of entangled photons with wavelength 710 nm. The photons are sent down two paths, one containing a delay line and another with two dove prisms (DP) to manipulate the SPDC state symmetry. A turbulence phase plate (TPP) in path A perturbs the state before the photon paths are recombined at a 50:50 beam-splitter (BS). Lenses L_1 (f_1 = 100 mm) and L_2 (f_2 = 750 mm) relay the plane of the BBO crystal onto the spatial light modulator (SLM). The two photons are probed using digital holograms encoded on the SLM, passed through 10 nm bandpass filters (F), and then coupled to single mode fibres (SMF). (b) Shows the range of phase fluctuations across the turbulence phase plate. 64

5.2 Hong-Ou-Mandel interference signal for (anti)symmetric states. Delaying one photon with respect to the other leads to (a) a dip and (b) a peak in coincidence counts for the symmetric ($\ell = 0$) and antisymmetric $\ell = \pm 1$ states, respectively. In the presence of turbulence, the visibility of the HOM interference decays in both subspaces, together with the coincidence counts. 68

5.3 Quantum state tomography of two-photon state with HOM filter OFF/ON. (a) Shows the normalised tomographic measurement performed with the HOM filter OFF in the absence of turbulence. (b) We introduced the turbulence plate in the path of photon A and show the effect of turbulence on the state tomography measurement outcomes. We repeated the measurements, this time with the HOM filter ON (c) in the absence of turbulence and (d) for the same locations across the turbulence plate. . . 69

5.4 Distillation of singlet states. With the HOM filter in the OFF state (outside the dip) the fidelity of the measured state with respect to the singlet Bell state decays with increasing perturbations of the turbulence phase plate. Switching the filter to the ON state results in the distillation of states with high-fidelity with respect to the singlet Bell state. This is shown within the (a) $\ell = \pm 1$ and (b) $\ell = \pm 3$ subspaces. 70

6.1 High–order Poincaré sphere (HOPS). We show the HOPS for the cases: (a) $\ell = 1$, (b) $\ell = -1$, (c) $\ell = 10$ and (d) $\ell = -10$. (e) and (f) show mutually unbiased vector and scalar vortex modes from, the $\ell = \pm 1$ and $\ell = \pm 10$ subspaces, respectively. The insets show the azimuthally varying phase profile of the scalar/OAM modes. Observe that the modes corresponding to the maximally entangled local local Bell states occur on the equator of the HOPS. 74

6.2 Deterministic detection of vector vortex modes. (a) A vector beam is generated by shaping attenuated light from a He-Ne laser with geometric phase optics: half-wave plates (HWP1 and HWP2) and a q-plate (QP). A polarisation grating (PG) maps circular polarisation to two paths, a and b, which are then interfered at a 50:50 beam-splitter (BS). Subsequently the OAM states are measured using mode sorters (MS1 and MS2) that map OAM to position. The output ports (c or d) of the BS and the lateral locations ($|\ell\rangle$ or $|-\ell\rangle$) deterministically indicate the Bell state being measured by the detectors F1–F4. Experimental results from the spatial sorting of vector modes are shown in (b) for $\ell = \pm 1$ and (c) for $\ell = \pm 10$, with crosstalk matrices for these subspaces shown in (d) and (e). M1 and M2 are mirrors; L1 and L2 are lenses, and F1–F4 are multimode fibers. . 76

6.3 Detection of superpositions of vector states. The two graphs show detection (normalised intensity) of superpositions of states from our vector basis. The superpositions were created by changing the HWP angle γ_1 (cp. Table 6.1). Each point was generated by averaging 30 measurements. The dashed lines represent the theoretical curve. 78

6.4 (a) Photon efficiency as a function of dimension for a deterministic and filter-based measurement scheme. (b) Effective key rate as a function of dimension shown experimentally (data points) for two measurement approaches, namely, filtering and deterministic detection. Data points show measurements in the subspaces of $\ell = \pm 1$ and $\ell = \pm 10$ for $d = 2$,3 and 4. The measurement fidelities for $\ell = \pm 1$ and $\ell = \pm 10$ were measured to be 0.96 and 0.97, respectively. The solid curves are theoretical bounds on the effective key rate assuming a fidelity of 1. 79

6.5 High dimensional QKD with vector modes. (a) Schematic of the inner product measurements performed between the vector states and their mutually unbiased counterparts, (b) theoretical scattering probabilities among the vector and scalar modes following the measurement procedure in (a), and experimental results for the (c) $\ell = \pm 1$ and (d) $\ell = \pm 10$ subspaces. (e) Alice and Bob agree on bit values for the vector and scalar modes. (f) Alice sends a random sequence of vector and scalar modes, which Bob randomly measures using either a vector analyser (VA) or a scalar analyser (SA). Alice and Bob, upon communication of the encoding and decoding bases through a classical channel, discard bit values for modes prepared and measured in complementary bases. (g) Shows a simple encryption/-decryption of an image using a 98 bit long key, sifted from a total of 200 transmitted bits. Photo courtesy photos-public-domain.com. 81

7.1 Historical trends in photonic entanglement engineering and control. 85

List of Tables

1.1 Linear polarisation states produced for $\theta = \pi/2$. 2

2.1 Eigenvectors and eigenvalues of the identity and Pauli matrices in the polarisation basis. 25
2.2 Eigenvectors and eigenvalues of the identity and Pauli matrices in the OAM basis. 26

6.1 Requirements for the generation of each of the four local local Bell states in the two subspaces of $|\ell| = 1$ and $|\ell| = 10$. The input state is a linearly polarised Gaussian beam and all angles are defined with respect to the horizontal axis. The experimental arrangements of the wave plates and q-plates is shown in Fig. 6.2(a). 75
6.2 Summary of the security analysis on the high dimensional protocol showing the experimental and theoretical values of the detection fidelity (F), mutual information I_{AB} between Alice and Bob, Eve's cloning fidelity (F_E) and mutual information with Alice I_{AE}, as well as the quantum error rate Q and information capacity per photon R in bits per photon. . 83

Asante mama na baba kwa kila kitu ambacho umenipa kwa hatua hii. Mungu awabariki.

List of Publications

Peer-reviewed Journal papers:

1. Ermes Toninelli, **Bienvenu Ndagano**, Adam Vallés, Bereneice Sephton, Isaac Nape, Antonio Ambrosio, Federico Capasso, Miles J. Padgett, and Andrew Forbes. "Concepts in quantum state tomography and classical implementation with intense light: a tutorial". *Advances in Optics and Photonics*, **11**:67, 2019

2. **Bienvenu Ndagano** and Andrew Forbes: "Entanglement distillation by Hong-Ou-Mandel interference with orbital angular momentum states". *Applied Physics Letters: Photonics*, **4**:016103, 2019.

3. **Bienvenu Ndagano**, and Andrew Forbes. "Characterization and mitigation of information loss in a six-state quantum-key-distribution protocol with spatial modes of light through turbulence". *Physical Review A*, 98:062330, 2018

4. Andrew Forbes, Andrea Aiello, and **Bienvenu Ndagano**. "Classically entangled light". In press in *Progress in Optics*, https://doi.org/10.1016/bs.po.2018.11.001.

5. Carmelo Rosales-Guzmán, **Bienvenu Ndagano**, and Andrew Forbes. "A review of complex vector light fields and their applications". *Journal of Optics*, 20:123001, 2018

6. Eileen Otte, Carmelo Rosales-Guzmán, **Bienvenu Ndagano**, Cornelia Denz, and Andrew Forbes. " Entanglement beating in free space through spin–orbit coupling". *Light: Science & Applications*, 7:18009, 2018

7. Martin P. J. Lavery, Mojtaba Mansour Abadi, Ralf Bauer, Gilberto Brambilla, Ling Cheng, Mitchell A. Cox, Angela Dudley, Andrew D. Ellis, Nicolas K. Fontaine, Anthony E. Kelly, Christoph Marquardt, Selaelo Matlhane, **Bienvenu Ndagano**, Francesco Petruccione, Radan Slavík, Filippo Romanato, Carmelo Rosales-Guzmán, Filippus S. Roux, Kobus Roux, Jian Wang, and Andrew Forbes. "Tackling Africa's digital divide". *Nature Photonics*, 12:249, 2018

8. **Bienvenu Ndagano**, Isaac Nape, Mitchell A. Cox, Carmelo Rosales-Guzman, and Andrew Forbes. "Creation and detection of vector vortex modes for classical and quantum communication". *Journal of Lightwave Technology*, 36:292, 2018

9. **Bienvenu Ndagano**, Isaac Nape, Benjamin Perez-Garcia, Stirling Scholes, Raul I. Hernandez-Aranda, Thomas Konrad, Martin P. J. Lavery, and Andrew Forbes. "A deterministic detector for vector vortex states". *Scientific Reports*, 7:13882, 2017

10. **Bienvenu Ndagano**, Nokwazi Mphuthi, Giovanni Milione, and Andrew Forbes. "Comparing mode-crosstalk and mode-dependent loss of laterally displaced orbital angular momentum and Hermite–Gaussian modes for free-space optical communication". *Optics Letters*, 42:4175, 2017

11. Isaac Nape, **Bienvenu Ndagano**, and Andrew Forbes. "Erasing the orbital angular momentum information of a photon". *Physical Review A*, 95:053859, 2017

12. **Bienvenu Ndagano**, Benjamin Perez-Garcia, Filippus S. Roux, Melanie McLaren, Carmelo Rosales-Guzman, Yingwen Zhang, Othmane Mouane, Raul I. Hernandez-Aranda, Thomas Konrad, and Andrew Forbes. "Characterizing quantum channels with non-separable states of classical light". *Nature Physics*, 13:397, 2017

13. **Bienvenu Ndagano**, Hend Sroor, Melanie McLaren, Carmelo Rosales-Guzmán, and Andrew Forbes. "Beam quality measure for vector beams". *Optics Letters*, 41:3407, 2016

14. Abderrahmen Trichili, Carmelo Rosales-Guzmán, Angela Dudley, **Bienvenu Ndagano**, Amine Ben Salem, Mourad Zghal, and Andrew Forbes. "Optical communication beyond orbital angular momentum". *Scientific Reports*, 6:27674, 2016

15. Robert Brüning, **Bienvenu Ndagano**, Melanie McLaren, Siegmund Schröter, Jens Kobelke, Michael Duparré, and Andrew Forbes. "Data transmission with twisted light through a free-space to fiber optical communication link". *Journal of Optics*, 18:03LT01, 2016

16. **Bienvenu Ndagano**, Robert Brüning, Melanie McLaren, Michael Duparré, and Andrew Forbes. "Fiber propagation of vector modes". *Optics Express*, 23:17330, 2015

Conference Proceedings:

1. Giovanni Milione, **Bienvenu Ndagano**, Nokwazi Mphuthi, and Andrew Forbes. "Using Hermite-Gaussian modes for free-space optical communication". *Complex Light and Optical Forces XII*, 10549:105490C, 2018

2. Isaac Nape, **Bienvenu Ndagano**, Benjamin Perez-Garcia, Raul I Hernandez-Aranda, Filippus S Roux, Thomas Konrad, and Andrew Forbes. "Hybrid entanglement for quantum information and communication applications". *Optical Trapping and Optical Micromanipulation XIV*, 10347:1034711, 2017

3. Isaac Nape, **Bienvenu Ndagano**, and Andrew Forbes. "Taking the quantum eraser to the abstract world". *Quantum Communications and Quantum Imaging XV*, 10409:1040906, 2017

4. Lucas Gailele, Loyiso Maweza, Angela Dudley, **Bienvenu Ndagano**, Carmelo Rosales-Guzman, and Andrew Forbes. "Multiplexing of spatial modes in the mid-IR region". *Laser Resonators, Microresonators, and Beam Control XIX*, 10090:100900Z, 2017

5. Carmelo Rosales-Guzmán, Abderrahmen Trichili, Angela L Dudley, **Bienvenu Ndagano**, Amine Ben Salem, Mourad Zghal, and Andrew Forbes. "Free-space communication with over 100 spatial modes". *Laser Resonators, Microresonators, and Beam Control XIX*, LTh1B. 4, 2016

6. Hend Sroor, **Bienvenu Ndagano**, Melanie McLaren, Carmelo Rosales-Guzman, and Andrew Forbes. "Vector quality measure for vector beams". *Laser Beam Shaping XVII*, 9950:99500F, 2016

7. Carmelo Rosales-Guzmán, Abderrahmen Trichili, Angela Dudley, **Bienvenu Ndagano**, Amine Ben Salem, Mourad Zghal, and Andrew Forbes. "Optical communications beyond orbital angular momentum". *Laser Beam Shaping XVII*, 9950:99500C, 2016

8. Abderrahmen Trichili, Angela Dudley, Amine Ben Salem, **Bienvenu Ndagano**, Mourad Zghal, and Andrew Forbes. "Encoding information using Laguerre Gaussian modes". *Laser Beam Shaping XVI*, 9581:95810F, 2015

Chapter 1

Introduction

Entanglement is one of the most acclaimed features of quantum theory. Exploiting entanglement as a resource has enabled multiple quantum processes that are poised to cause a leap in technological prowess in the field of communication, computing, imaging and sensing. The concept of entanglement is intertwined with that of non-separability. Through "spooky action at a distance" the states of two systems can be coupled in a non-separable manner, such that they can no longer be described independently from each other, regardless of how far apart they are located. The textbook example of entangled spins of two particles has now taken flesh and stature: it is at the heart of quantum information theory [1], and is driving progress towards a universal quantum computer [2–4] and long distance quantum communication [5–7]. Novel avenues have been explored to extend entanglement to more systems and higher dimensions. However, how does the nature of the entangled parties come into the description of entanglement? Certainly the textbook example of entangled spins of quantum particles describe entanglement correlations as existing between two distinct systems that can be physically separated. However, is there a physical requirement for it? Can non-quantum systems exhibit entanglement correlations? These questions have become topical recently [8–11]. In this section we will present our view on the issue and more interestingly, explain the origins of a fascinating and controversial idea: classical entanglement.

1.1 The quantum bit

The quantum bit (qubit) is the fundamental unit of quantum information. Unlike a classical bit that assumes one of two distinct states, 0 or 1, the quantum bit is a weighted superposition of two orthogonal states of a given degree of freedom, for example

$$|\psi\rangle = \alpha\,|0\rangle + \beta\,|1\rangle, \tag{1.1}$$

with complex weighting factors α and β such that $|\alpha|^2 + |\beta|^2 = 1$. Spin states are the most common example of qubits currently explored to realise quantum computation and communication. For photons these spin states correspond to left- and right-circular polarisation states [12]. In general, one can express the state of a polarisation qubit as

$$|\psi\rangle = \cos(\theta/2)\,|R\rangle + \exp(i\varphi)\sin(\theta/2)\,|L\rangle, \tag{1.2}$$

where $|R\rangle$ and $|L\rangle$ represent the right- and left-circular polarisation states, respectively. The parameter $\varphi \in [0, 2\pi]$ is the phase difference between the polarisation states while θ is the weighting factor. In the special cases of $\theta = 0$ and $\theta = \pi$, the qubit state $|\psi\rangle$ corresponds to the polarisation eigenstates $|R\rangle$ and $|L\rangle$, respectively. By manipulating both θ and φ, one can produce arbitrary polarisation states. For example, for $\theta = \pi/2$, one prepares the qubit in the linear polarisation states depicted graphically in Table 1.1.

TABLE 1.1: Linear polarisation states produced for $\theta = \pi/2$.

phase φ	0	$\pi/2$	π	$3\pi/2$
Qubit state $\|\psi\rangle$	$\leftrightarrow$	$\nwarrow\!\!\searrow$	$\updownarrow$	$\swarrow\!\!\nearrow$

The definition of the qubit state in Eq. 1.2 has an intuitive representation as a point on a sphere, commonly referred to as the Poincaré sphere. First let us look at the effect of tuning the amplitudes, by varying θ. Normalisation of the quantum state requires conservation of probability; that is, the probability of finding the qubit $|\psi\rangle$ in any of its eigenstates must be 1 (the qubit must be in some state after all). Mathematically, this is expressed as

$$\langle\psi|\psi\rangle = \cos^2(\theta/2) + \sin^2(\theta/2) = 1. \tag{1.3}$$

By visual examination, one notices that Eq. 1.3 describes a circle of radius 1, where θ parametrises the position on the circle, as shown in Fig. 1.1(a). Let us refer to this as the amplitude circle.

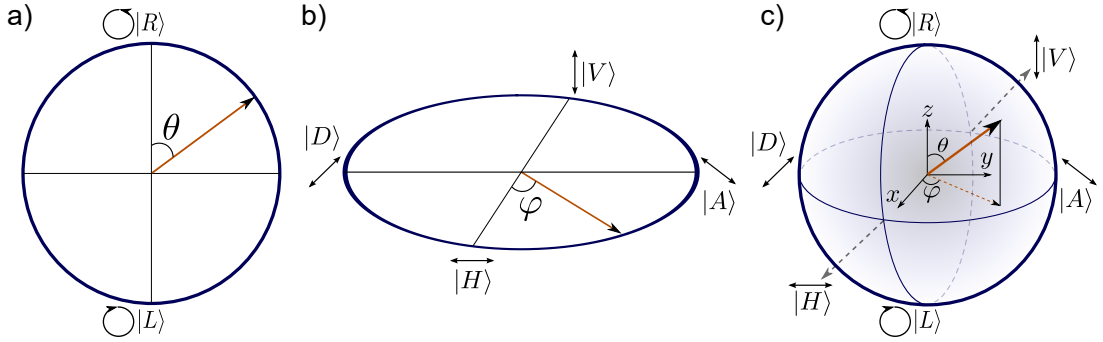


FIGURE 1.1: Intuitive description of the Poincaré sphere. (a) Control over the amplitude parameter θ allows one to continuously change the position of the qubit (indicated by the arrow) on the unit circle, resulting in a change of the relative amplitudes of left- and right-circular polarisation states. (b) Control over the phase parameter φ allows one to continuously rotate the qubit state at different positions around a circle at fixed relative amplitude between the basis states (fixed θ). This is demonstrated for $\theta = \pi/2$. (c) Simultaneous control of phase and amplitude results in a description of the general qubit in Eq. 1.2 on a unit sphere where the poles are the basis polarisation states.

The phase term $\exp(i\varphi)$ is an oscillatory function, whose variable φ can be bounded in the interval $[0, 2\pi]$. By plotting this oscillatory function on the complex plane, one realises that the angle φ maps to angular position on a circle. The polarisation state rotates as the state vector precesses around the circle as a function of φ. This is shown in Fig. 1.1(b) for linearly polarised states ($\theta = \pi/2$). We will refer to this circle as the phase circle.

The Poincaré sphere brings the description of amplitude and phase variation into a single picture. Place a point on the amplitude circle by fixing θ, rotate it around the phase circle by an angle φ, and one has the recipe for describing a general qubit state on the surface of the Poincaré sphere. Thus an arbitrary qubit state parametrised by a unique set of coordinates (θ, φ) can be mapped to a point on the unit sphere as shown in Fig. 1.1(c). In the Poincaré sphere representation, the qubit state lives on the surface of a sphere, and motion on the sphere transforms one qubit state into another. This description is, however, specific to pure states. A more general description of a qubit state is provided through the density matrix formalism.

The density matrix description of quantum states is more general than the state vector description of Eq. 1.2. This is because density matrices allow one to describe the actual outcome of measurements, and pertinently, for both pure and mixed states. Imagine we have an ensemble of K independent single photons, each prepared in the qubit state $|\psi_n\rangle$ with $n = \{1, 2, ..., K\}$. If all the photons are identical, that is, they are prepared in the same state $|\psi_n\rangle = |\psi\rangle$, then every photon can be described using a single state vector $|\psi\rangle$ as in Eq. 1.2. The state of an arbitrary photon in the ensemble is then said to be pure. Conversely, if some (or all) of the K photons are prepared in different states, the

result is a statistical mixture of pure states. A photon randomly chosen in the ensemble can be found to be in a given pure state $|\psi_n\rangle$ with a certain probability. Consequently, the formalism in Eq. 1.2 cannot appropriately describe such a mixture. A density matrix is a useful tool to overcome this hurdle.

Assume that the state of a single photon in the aforementioned ensemble can be described by a 2×2 matrix, ρ, which we call the density matrix. In general, ρ can be decomposed in terms of its eigenvectors and eigenvalues:

$$\rho = \sum_m c_m |\psi_m\rangle\langle\psi_m|. \tag{1.4}$$

In this description each c_m is real, positive, and corresponds to the probability of measuring a photon prepared in the eigenstate $|\psi_m\rangle$. Conservation of probabilities requires that $\sum_m c_m = 1$. By construction, density matrices must be Hermitian; that is, $\rho^\dagger = \rho$, where superscript $\dagger$ (called "dagger") refers to the complex conjugation + transpose operation. This can be easily verified as $(|\psi_m\rangle\langle\psi_m|)^\dagger = |\psi_m\rangle\langle\psi_m|$.

The density matrix in Eq. 1.4 describes a statistical mixture of pure qubit states $|\psi_m\rangle\langle\psi_m|$. Hence we refer to ρ as a mixed state density matrix. In the special case where all photons are identically prepared (pure state), there exists only one eigenstate with unit eigenvalue. The pure state density matrix then reads $\rho = 1|\psi_m\rangle\langle\psi_m| = |\psi\rangle\langle\psi|$. For the pure state in Eq. 1.2, the density matrix is expressed as follows:

$$\begin{aligned}\rho = |\psi\rangle\langle\psi| = &\cos^2(\theta/2)|R\rangle\langle R| + \sin^2(\theta/2)|L\rangle\langle L| + \\ &\cos(\theta/2)\sin(\theta/2)\exp(-i\varphi/2)|R\rangle\langle L| + \\ &\cos(\theta/2)\sin(\theta/2)\exp(i\varphi/2)|L\rangle\langle R|.\end{aligned} \tag{1.5}$$

One can now provide a matrix representation of ρ by assigning coordinate vectors to the basis states. For example, assume the following representation of the polarisation states: $|R\rangle \equiv (1\ 0)^T$ and $|L\rangle \equiv (0\ 1)^T$ where the superscript T refers to matrix transpose. The density matrix thus assumes the following matrix representation:

$$\rho = \begin{pmatrix} \cos^2(\theta/2) & \cos(\theta/2)\sin(\theta/2) \\ \cos(\theta/2)\sin(\theta/2) & \sin^2(\theta/2) \end{pmatrix}. \tag{1.6}$$

For density matrices, the conservation of probability in Eq. 1.3 is expressed as $\mathrm{tr}\,(\rho) = 1$, where tr is the trace operation:

$$\mathrm{tr}\,(\rho) = \cos^2(\theta/2) + \sin^2(\theta/2) = 1. \tag{1.7}$$

This is a physical requirement for any density matrix. However one can decide whether it corresponds to a pure or a mixed state by computing the purity

$$\begin{aligned} \mathrm{tr}\left(\rho^2\right) &= \mathrm{tr}\left(\sum_m \sum_n c_m c_n |\psi_m\rangle\langle\psi_m||\psi_n\rangle\langle\psi_n|\right) && (1.8) \\ &= \sum_m \sum_n c_m c_n |\left\langle\psi_m|\psi_n\right\rangle|^2. && (1.9) \end{aligned}$$

It follows that $|\left\langle\psi_m|\psi_n\right\rangle|^2 \leq 1$; this is because the probability of measuring a state $|\psi_m\rangle$ given that we prepared $|\psi_n\rangle$ is in general less than 1, except when $|\psi_m\rangle = |\psi_n\rangle$, in which case the overlap is 1. We can then bound Eq. 1.9 as follows

$$0 \leq \sum_m \sum_n c_m c_n |\left\langle\psi_m|\psi_n\right\rangle|^2 \leq \sum_m c_m \sum_n c_n = 1, \tag{1.10}$$

where we have used the fact that $\sum_m c_m = 1$. One then arrives at the following criterion for purity:

$$\begin{cases} \mathrm{tr}\left(\rho^2\right) = 1 \quad \text{for } c_m = c_n = 1 \Rightarrow \rho \text{ is pure} \\ 0 \leq \mathrm{tr}\left(\rho^2\right) < 1 \quad \text{for } c_m, c_n < 1 \Rightarrow \rho \text{ is mixed.} \end{cases} \tag{1.11}$$

In order to be useful in a quantum application, it is necessary to be able to manipulate and characterise the qubit state. This requires locating the qubit on the sphere and moving it to a different position. Given that the geometry is spherical, we simply require a reference point on the sphere and a set of rotation transformations about the origin. In 3 dimensions, one needs a set of rotations about the x-, y- or z-axis, as shown in Fig. 1.2. If the initial state is known, the final state can be uniquely determined by evaluating the amplitudes of the relative rotations. And that is the objective of a quantum state tomography (QST) [13, 14]. Given that the motion of our qubit state is restricted to rotations on the Poincaré sphere, the density matrix can thus be expressed in terms of rotation operators about the x-, y- and z-axes. In two-dimensions, these rotation operators are the Pauli matrices, σ_i, plus the identity

$$\sigma_1 = \begin{pmatrix} 0 & 1 \\ 1 & 0 \end{pmatrix}; \quad \sigma_2 = \begin{pmatrix} 0 & -i \\ i & 0 \end{pmatrix}; \quad \sigma_3 = \begin{pmatrix} 1 & 0 \\ 0 & -1 \end{pmatrix}; \quad \mathbb{I} = \begin{pmatrix} 1 & 0 \\ 0 & 1 \end{pmatrix}.$$

The Pauli matrices are traceless operators ($\mathrm{tr}(\sigma_i) = 0$) that obey the following trace relations

$$\mathrm{tr}\left(\sigma_i \sigma_j\right) = 2\delta_{i,j}, \qquad \text{for } i, j = 1, 2 \text{ or } 3. \tag{1.12}$$

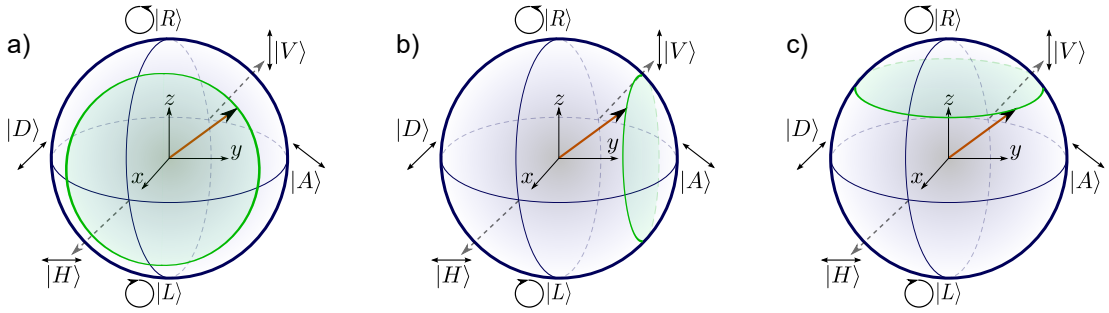


FIGURE 1.2: Elementary rotations on the surface of the Poincaré sphere. The qubit state, indicated by the position vector (red arrow), can be rotated on the surface of the sphere about the (a) x-axis, (b) y-axis and (c) z-axis.

This is an expression of the completeness relation between the matrices. Unlike the other Pauli matrices, the identity operator is not traceless, but obeys the trace relations

$$\mathbb{I} = \sigma_0 = \begin{pmatrix} 1 & 0 \\ 0 & 1 \end{pmatrix}; \qquad \mathrm{tr}\left(\sigma_0\sigma_0\right) = 2\ ; \qquad \mathrm{tr}\left(\sigma_0\sigma_i\right) = \mathrm{tr}\left(\sigma_i\sigma_0\right) = \mathrm{tr}\left(\sigma_j\right) = 0.$$

That the σ_i matrices form a complete set means that one can express the density matrix ρ as a linear combination of our four σ_i matrices

$$\rho = \frac{1}{2}\sum_{n=0}^{3} \rho_n \sigma_n, \tag{1.13}$$

where ρ_n are the expectation values of the matrices σ_n, and are obtained as follows

$$\mathrm{tr}\left(\rho\sigma_n\right) = \frac{1}{2}\mathrm{tr}\left(\sum_{m=0}^{3} \rho_m \sigma_m \sigma_n\right) = \frac{1}{2}\sum_{m=0}^{3} \rho_m \mathrm{tr}\left(\sigma_m\sigma_n\right) = \sum_{m=0}^{3} \rho_m \delta_{m,n} = \rho_n. \tag{1.14}$$

Thus, determining the values ρ_n fully characterises an arbitrary qubit state ρ.

1.2 The spatial qubit

An alternative (to polarisation) and topical degree of freedom is the spatial mode of photons [15–20]. The term spatial mode refers to transverse solutions of the wave equation in the paraxial limit; that is, when the variation in transverse momentum is negligible when compared its longitudinal counterpart. In this regime, a family of solutions arises: Hermite-Gaussian, Laguerre-Gaussian and Bessel-Gaussian modes, just to name a few. Some of these modes carry discrete units of a fundamental quantum number: the orbital angular momentum (OAM). Conserved at the single photon level [21], the OAM degree of freedom is particularly attractive to quantum information and quantum

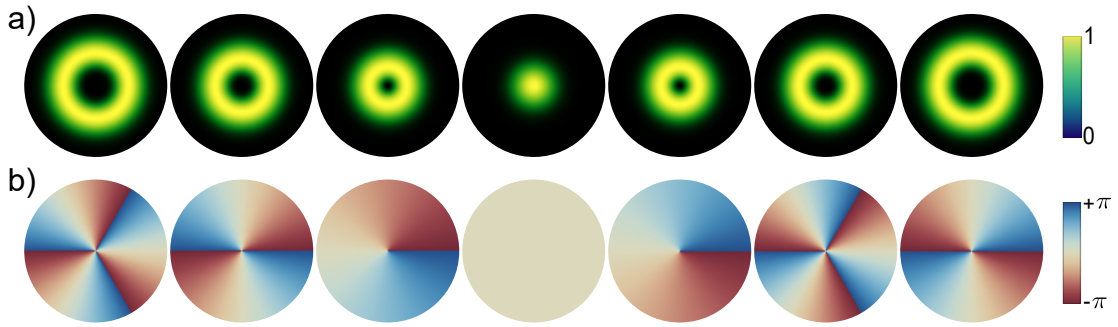


FIGURE 1.3: (a) Intensities and (b) phase-maps of OAM modes carrying, from left to right, $\ell = -3,\ -2, \cdots,\ +2$ and $+3$ units of OAM.

computation. Unlike polarisation, the state space of OAM modes is infinitely large, allowing more information to be encoded in photons [22–26].

Recall the polarisation qubit state in Eq. 1.2. An analogous description can be provided in terms of spatial modes that carry OAM:

$$|\psi\rangle = \cos(\theta/2)\,|\ell_1\rangle + \exp(i\varphi)\sin(\theta/2)\,|\ell_2\rangle, \tag{1.15}$$

where the ket $|\ell\rangle$ refers to a paraxial field that carries $\ell\hbar$ units of OAM. The electric field of a photon carrying OAM can be expressed in cylindrical coordinates (r, ϕ, z) as follows:

$$|\ell\rangle \equiv A(r, z)\exp(i\ell\phi), \tag{1.16}$$

where $A(r, z)$ is an amplitude term that varies transversally and longitudinally. The intensity and phase distributions of some OAM modes of the Laguerre-Gaussian type are shown in Fig. 1.3. The azimuthal phase creates a twisted wavefront with a central discontinuity where the phase is undefined, resulting in a null intensity in the centre.

Observe that the field of the OAM mode is separable in both amplitude and azimuthal phase; that is, the amplitude and azimuthal phase can be factorised. Thus it is trivial to show the orthogonality of OAM modes at a given z-plane (say $z = z_0$) may be expressed by

$$\begin{aligned}\langle \ell_1|\ell_2\rangle &= \int_0^\infty dr\ rA_1^*(r, z_0)A_2(r, z_0)\int_0^{2\pi} d\phi\exp(i(\ell_2 - \ell_1)\phi)\\ &= \delta_{\ell_1,\ell_2}\ 2\pi\int_0^\infty dr\ rA_1^*(r, z_0)A_2(r, z_0).\end{aligned} \tag{1.17}$$

OAM modes form an orthogonal basis in which information can be encoded. Note that the basis can be made orthonormal through appropriate choice of amplitude function A.

Similarly to polarisation, OAM qubits can be represented on the surface of a sphere, the OAM Bloch sphere [27], as shown in Fig. 1.4 for $\ell_1 = -\ell_2 = 1$. Here the states at the

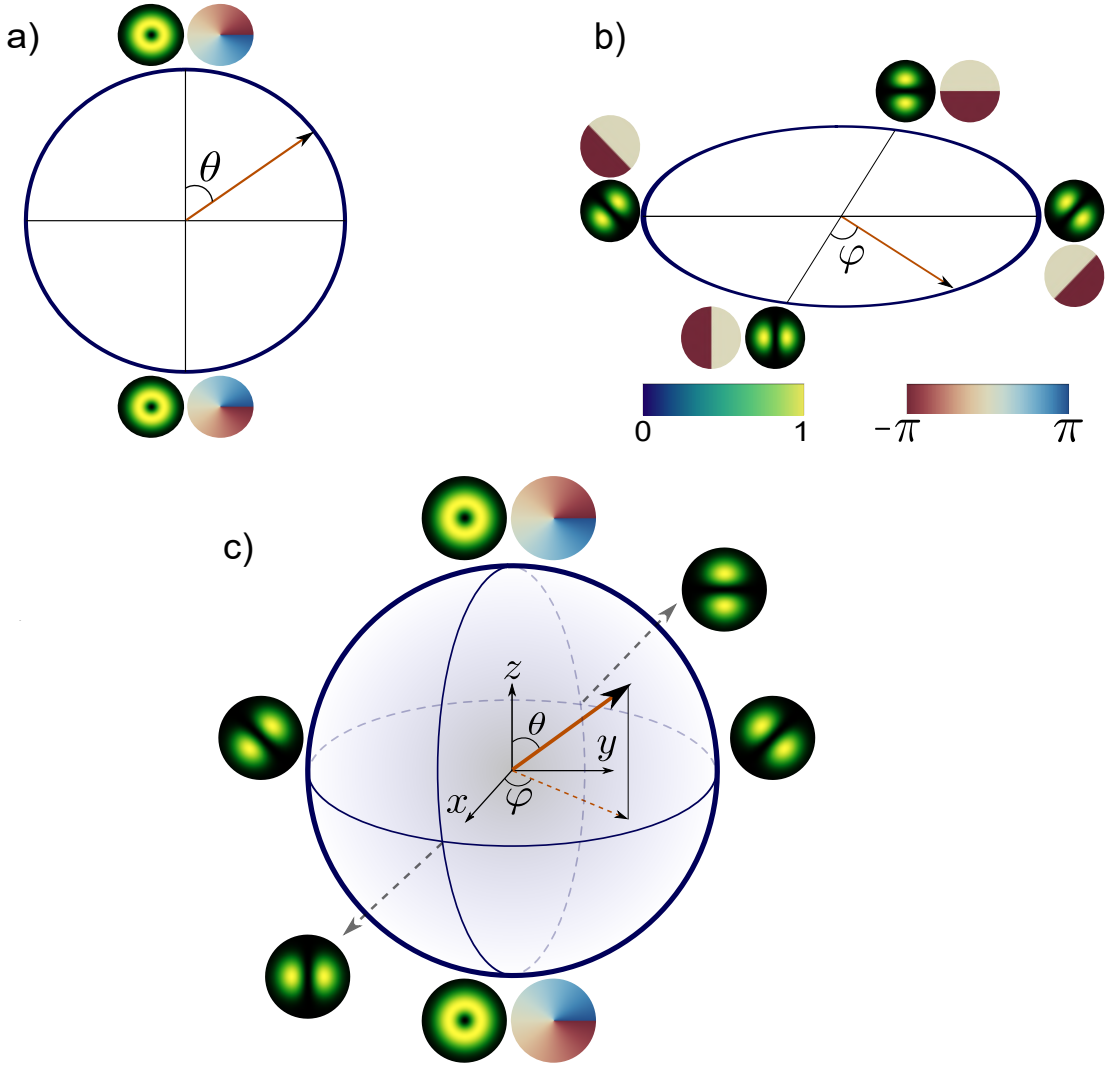


FIGURE 1.4: Bloch sphere description of an OAM qubit with $\ell_1 = -\ell_2 = 1$. Control over the amplitude parameter θ and phase parameter φ as shown in (a) and (b) respectively, leads to (c) a description of an arbitrary OAM qubit on the OAM sphere.

poles are the OAM states. Observe that the superposition of two oppositely charged OAM states leads to azimuthal fringes on the equator of the OAM Bloch sphere. These fringes rotate with the intermodal phase φ in a similar fashion to the linear polarisation states in Fig. 1.1.

The density matrix formalism we laid out for polarisation qubits can equally be applied to spatial qubits, together with the method to characterise the qubit on the surface of the sphere by computing the expectation values of the Pauli matrices. The Poincaré and Bloch sphere description will be useful in describing multi-photon states, as we do in the next section. In particular, going beyond the single qubit picture allows for multi-particle correlations and thus, entanglement.

1.3 Entangled spatial modes

We start by describing a general two-particle system with a density matrix ρ as

$$\rho = \sum_m c_m |\psi_m\rangle\langle\psi_m|, \tag{1.18}$$

where the pure states $|\psi_m\rangle$ are now two-particle qubit states, described by

$$|\psi_m\rangle = \sum_{i,j} \alpha_m^{ij} |i\rangle_A \otimes |j\rangle_B. \tag{1.19}$$

The states $|i\rangle$ and $|j\rangle$ are eigenstates of the systems A and B respectively, with associated complex coefficients α_m^{ij} that define the m^{th} state $|\psi_m\rangle$. The symbol $\otimes$ is a tensor product operation which, in essence, is a way to multiply two state vectors of dimension d_1 and d_2 respectively, to form a joint state vector that lives in a Hilbert space with dimension $d_1 \times d_2$. In the case of a two-qubit state, the joint system is four-dimensional. The state of each qubit can be characterised with the set of rotation matrices (Pauli matrices) plus the identity matrix. The joint state, therefore, follows a tensor product construction as follows:

$$\rho = \left(\frac{1}{2}\sum_{m=0}^{3} \rho_m \sigma_m\right)_A \otimes \left(\frac{1}{2}\sum_{n=0}^{3} \rho_n \sigma_n\right)_B = \frac{1}{4}\sum_{m,n=0}^{3} \rho_{mn}\ \sigma_m \otimes \sigma_n. \tag{1.20}$$

The above construction naturally leads to the description of the qubit pair on the surface of a higher-order Bloch sphere, as shown in Fig. 1.5. In this description, the states on the sphere follow the same tensor product construction as that in Eq. 1.19. While there are many tensor product combinations of single photon qubit states that are allowed, there is only one rule for constructing the higher-order Bloch sphere: The states at the pole of the sphere must be orthogonal. For example, one cannot construct a higher-order Bloch sphere with the states $|\ell\rangle\,|-\ell\rangle$ and $|\ell\rangle\,|\ell\rangle$ at the poles. This is because any two-qubit pair formed as a linear superposition of these two qubit states factorises with respect to each subsystem. This simply means that one can write the two-qubit state as $|\psi\rangle = (\cdot)_A \otimes (\cdot)_B$:

$$|\psi\rangle = \cos(\theta/2)\,|\ell\rangle_A\,|-\ell\rangle_B + \exp(i\varphi)\sin(\theta/2)\,|\ell\rangle_A\,|\ell\rangle_B, \tag{1.21}$$

$$\Rightarrow |\psi\rangle = |\ell\rangle_A \otimes \Big(\cos(\theta/2)\,|-\ell\rangle + \exp(i\varphi)\sin(\theta/2)\,|\ell\rangle\Big)_B. \tag{1.22}$$

Observe that the two-qubit state is parametrised by θ and φ, and can be entirely characterised by single qubit rotation on subsystem B alone. We thus say that the two subsystems are separable. The notion of separability will be treated in more detail a little later. The higher-order Bloch sphere description is much richer because an arbit-

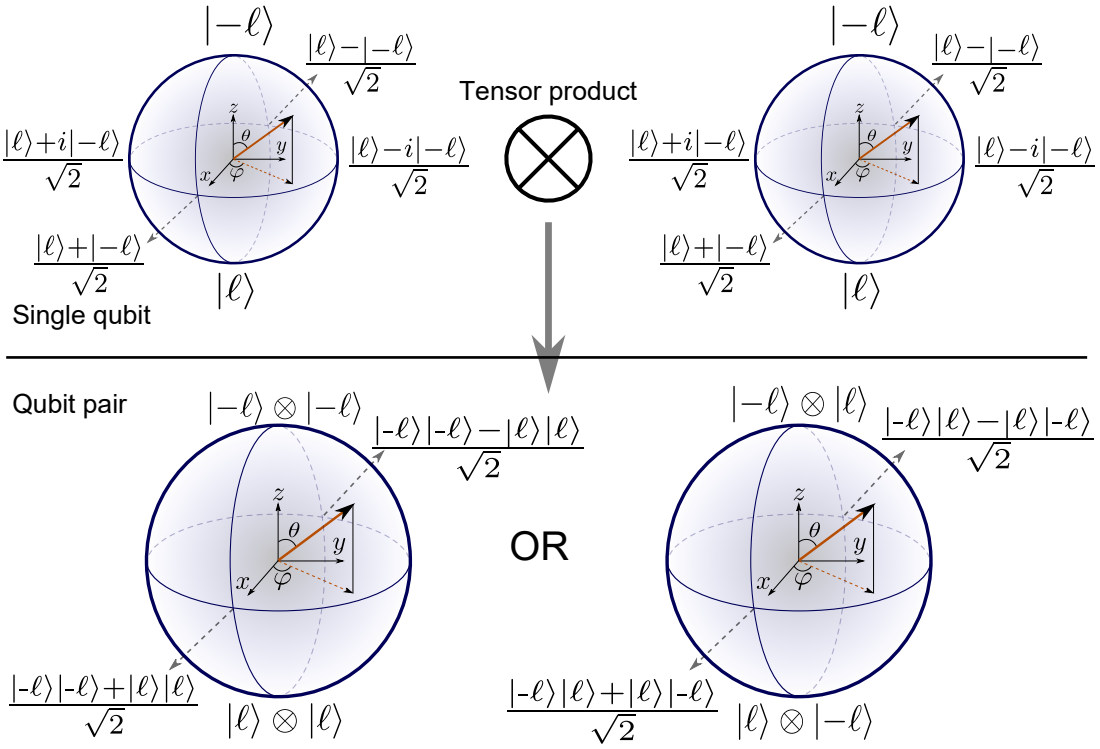


FIGURE 1.5: Description of qubit pairs on the higher-order Bloch sphere. States on the surface of the higher-order Bloch sphere are constructed from the tensor product of qubit states from two Bloch sphere, each describing a subsystem (photon). Depending on the way in which the eigenstates combine at the poles, one can construct two higher-order Bloch spheres for a system of qubit pair.

rary state on the surface cannot, in general, be characterised by single qubit rotations on one subsystem alone. In other words, the higher-order Bloch sphere describes states that are in general non-separable, and that can be represented as follows

$$|\psi\rangle = \cos(\theta/2)\,|\ell_1\rangle\,|\ell_2\rangle + \exp(i\varphi)\sin(\theta/2)\,|-\ell_1\rangle\,|-\ell_2\rangle. \tag{1.23}$$

A bi-photon state described as in Eq. 1.23 is in general non-separable (except for $\theta = 0$ or π) and one would say that the photons are quantum entangled. But does the "quantumness" of entanglement naturally arises from Eq. 1.23?

1.4 Is entanglement intrinsically quantum?

The quintessential property of entanglement is non-separability. The notion that two systems cannot be described independently from each other, or put another way, that a measurement on one system affects the outcome of the other. Mathematically we say that the joint state does not factorise; that is, given two systems A and B, the

joint density matrix ρ_{AB} cannot be expressed as the tensor product of the individual density matrices ρ_A and ρ_B. Thus any state that is not separable is said to be entangled. Note at this point that we have not specified anything about the nature of the systems A and B (whether they are classical or quantum). Yet, we have logically arrived at a condition for separability and entanglement. So where does the 'quantumness' of entanglement originate? The reason is none other than context. We believe the issue lies in understanding what is entangled.

Suppose you were to deliver pairs of identically prepared entangled photons to two experimentalists, Alice and Bob, who are both tasked to test for violation of the Bell-CHSH inequality. One way to test the 'quantumness' of entanglement correlations is through the Bell-CHSH inequality, and this has successfully been demonstrated experimentally [28–34]. However, Alice and Bob cannot agree on what to measure: Alice wishes to perform her measurement in polarisation while Bob prefers to do it in the spatial degree of freedom. They both proceed and return their result to a third party, Eve, as one of 2 possibilities: "entangled" or "not entangled". Eve can draw the following conclusions:

1. *Both or None of Alice and Bob show violation of the CHSH inequality.* In this case, both experimentalists agree and Eve can logically confirm or rebuke entanglement.

2. *Either Alice or Bob shows violation of the CHSH inequality.* Now Eve is in a difficult position. Not knowing that Alice and Bob measured different degrees of freedom, she is faced with conflicting results and thus cannot make a decision.

It is imperative that one specifies the degree of freedom in which the photons are entangled. This brings us back to the question of what it is that is entangled: are the photons entangled? or are the states of the photons entangled? From the mini game earlier, it is clear that it is the latter, it is the states that are entangled and not the objects that happen to carry those states. This is an important distinction because it brings us to a current topical issue, that of classical entanglement: can a classical state of light be entangled? We can now reformulate the question in terms of our criteria for separability: can one construct a classical state of light that is non-separable? If yes then the classical state can be said to be entangled in the non-separable degree(s) of freedom.

1.5 Classical entanglement

Optical fields may be scalar or vector, with vector beams now topical classical states of light [35–37]. The vector nature of these beams stems from the fact that they possess a

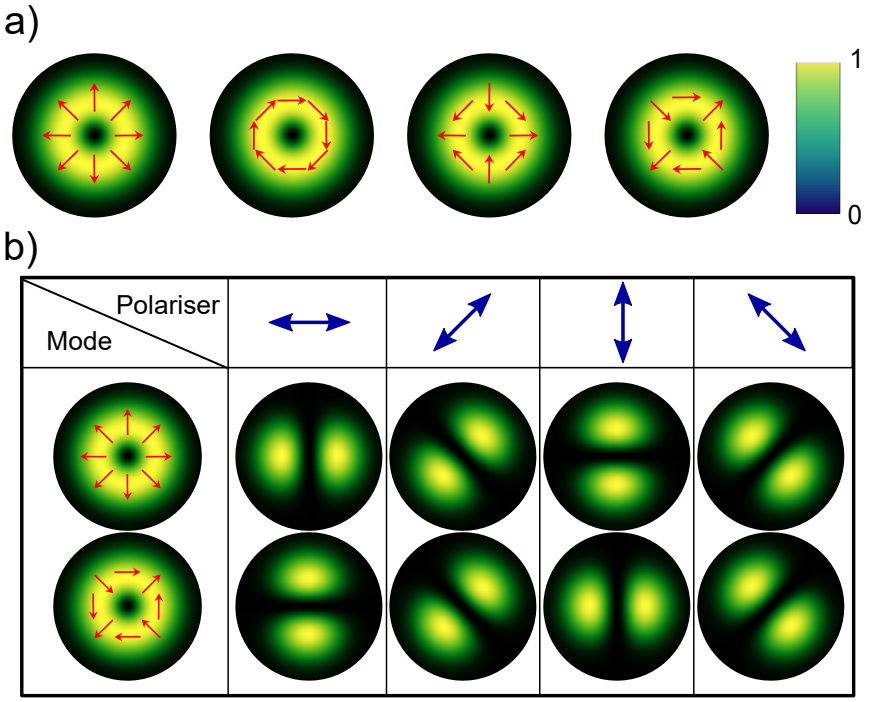


FIGURE 1.6: (a) Intensity and polarisation map of some vector beams. The non-separability of the space and polarisation degrees of freedom is reflected in the space variant (inhomogeneous) polarisation. (b) The non-separability of the two degrees of freedom manifests itself if one passes the beam through a rotating linear polariser and measures the resulting spatial mode on a camera, as shown here for two vector beams.

spatially varying polarisation state across the transverse plane. This coupling of space to polarisation can be expressed as a non-separable superposition of spatial modes and polarisation. To see what this means, consider the sample of vector beams shown in Fig. 1.6 (a). If one of them, say the first on the left (radially polarised light), was passed through a linear polariser, the pattern of light seen on a camera would change as one rotates the polariser. We understand this as filtering out only particular polarisation directions from the field. Put into the language of quantum mechanics: a measurement on one system affects the outcome of a measurement on the other. The measurement on the spatial mode (with the camera) was affected by the prior choice of a measurement on the polarisation. In contrast this does not happen with scalar beams, which are completely separable. Here the camera may get more or less light according to the angle of the polariser, but the pattern of light on the camera will not change. The vector beams shown in Fig. 1.6 (a) can be conveniently expressed using braket notation:

$$|\psi\rangle = \cos(\theta/2)\,|\ell\rangle_A\,|R\rangle_B + \exp(i\varphi)\sin(\theta/2)\,|-\ell\rangle_A\,|L\rangle_B. \tag{1.24}$$

Note that this expression of a vector beam is reminiscent of that in Eq. 1.23, which we used to describe an arbitrary state on the surface of the higher-order Bloch sphere. One

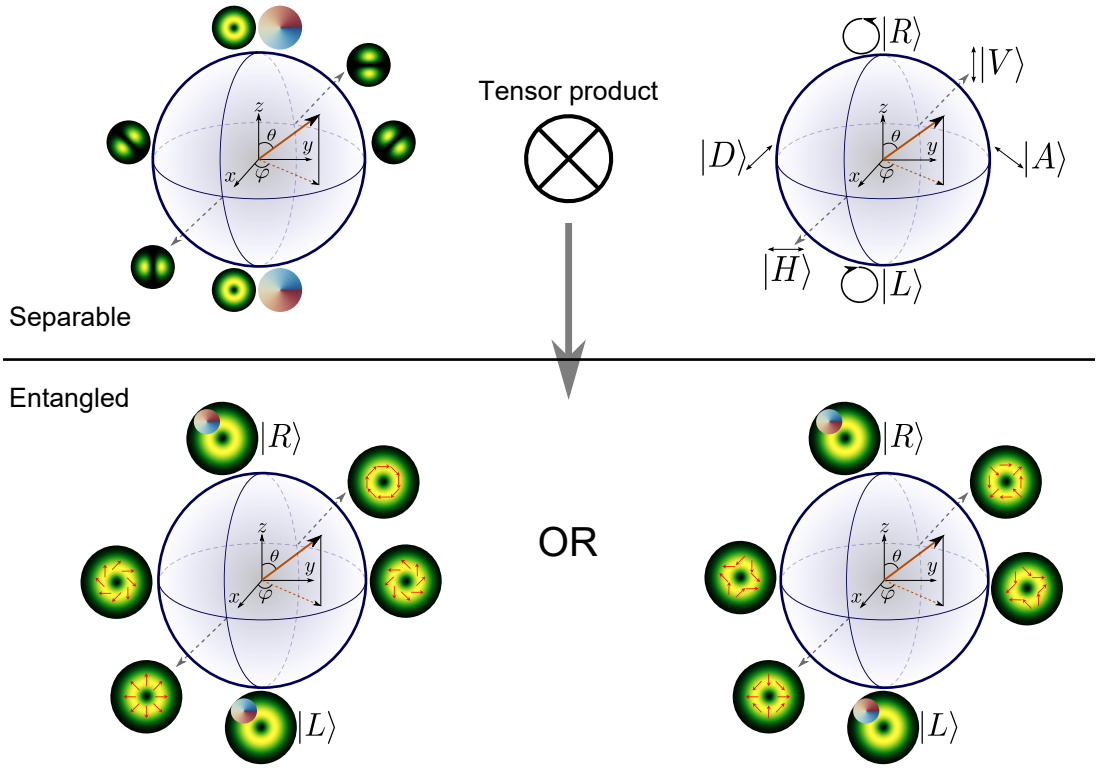


FIGURE 1.7: Description of hybrid states on the HOPS. States on the surface of the HOPS are constructed from the tensor product of OAM states from the Bloch sphere and polarisation states from the Poincaré sphere. Here, each sphere describes a degree of freedom. Depending on the way in which the eigenstates combine at the poles, one can construct two HOPS for a system of hybrid qubit states. The equator represents maximally entangled states whereas the poles represent non-entangled states.

of the conclusions we drew regarding the state in Eq. 1.23 was it was non-separable and therefore entangled. Here we have only one intense beam of light that is non-separable in two degrees of freedom, spatial mode and polarisation. Once again we highlight that entanglement is a correlation between states. Thus we can conclude that vector beams also carry a form of entanglement in their degrees of freedom, albeit local, and called classical entanglement.

The state in Eq. 1.24 can be described as a point on the surface of a new sphere, the higher-order Poincare sphere (HOPS) [38–40]. The sphere is constructed from the tensor product of the eigenstates of the individual subsystems, as shown in Fig. 1.7. Analogous to the higher-order Bloch sphere, we can express the density matrix of a state on the HOPS as follows:

$$\rho = \left(\frac{1}{2}\sum_{m=0}^{3}\rho_m\sigma_m\right)^{\text{orbit}} \otimes \left(\frac{1}{2}\sum_{n=0}^{3}\rho_n\sigma_n\right)^{\text{spin}} = \frac{1}{4}\sum_{m,n=0}^{3}\rho_{mn}\ \sigma_m^{\text{orbit}} \otimes \sigma_n^{\text{spin}}, \qquad (1.25)$$

where σ_m^{orbit} and σ_m^{spin} refer to the Pauli and identity matrices, whose eigenstates correspond to OAM and polarisation states, respectively.

Indeed entanglement between the quantum states of two particles exhibit non-locality: it persists even when the particles are spacelike separated; that is, the particles are sufficiently far apart that in the event of a joint measurement, a field would need to propagate faster than light from one detector to the other in order to influence the measurement outcome. It is because of this non-locality that entanglement cannot be classified as exchange of information between the correlated particles; measuring the OAM of one photon in the OAM entangled pair does not result in a signal travelling to the other photon that tells it to assume a particular state. Such non-locality does not exist in the classically entangled fields we are describing here.

The degrees of freedom of a vector beam are defined locally and thus cannot exhibit non-local correlations. So can one still maintain that vector beams are entangled states? Yes, because the definition of entanglement was linked to the separability of the state and made no mention of non-locality. The issue of non-locality only arose when we added additional constraints to the description of the system: we specified the nature of the carriers of the entangled states. It is only after assigning the entangled states to particles that emerged the non-local aspect of entanglement. When we did the same with an inherently local system, there was naturally no chance of non-local correlations. However, in both systems, entanglement correlations exist. It is thus useful to make a distinction between these two flavours of entanglement. Because non-local correlations are inherently quantum, we can logically refer to entanglement of quantum particles as quantum entanglement and that of local classical systems, such as vector beams, as classical entanglement.

1.6 Outline

In the following chapters, we will introduce the theoretical framework and experimental tools that have been employed to produce the many contributions detailed thereafter. In Chapter 2 we describe methods to generate non-separable states of light through dynamic and geometric phase control. By reversing the generation step, we demonstrate theoretically and experimentally the vector mode decomposition through inner product measurement. This allows one expand an arbitrary field in a basis of non-separable states of light. Finally, we borrow tools from the quantum realm and demonstrate quantum state tomography adapted to classically entangled light.

In Chapter 3 we apply the tools developed in Chapter 2 to demonstrate the equivalence of quantum and classical entanglement in a one-sided turbulent channel. By performing a state tomography of the classical and quantum systems after propagating through a one-sided turbulent channel, we show the decay of entanglement correlations in both systems to be identical. This would allow for real-time error correction on the quantum state using bright classical sources. Furthermore we prove the existence of channel-state duality in the form of the Choi-Jamiolkowski isomorphism for classical entanglement. In particular we show that the entanglement decay of a quantum state with arbitrary degree of entanglement can be predicted from knowledge of the decay of a classical maximally entangled state.

In Chapter 4 we explore means to increase the robustness of quantum communication links and mitigate errors and photon loss in the measurement process. Our premise is a quantum key distribution protocol with entangled OAM modes through turbulence. We show that the robustness of the link is increased as the separation on the modes in state space increases. Given that turbulence leads to photon loss during post-selection, we show that probing additional subspaces at the measurement stage increases both the photon and information recovery. In addition, we demonstrate a Procrustean filtering method whereby local operations on one party in the entangled pair increase the degree of entanglement of the perturbed state. This method makes use of the characterisation process presented in Chapter 3 to obtain the channel operator necessary to perform the filtering.

In Chapter 5 we build on the concept of entanglement concentration introduced in Chapter 4 in the form of Procrustean filtering. We introduce a process of entanglement distillation that does not require prior knowledge of the channel operator. We use the Hong-Ou-Mandel interference as a filer to distil singlet Bell states from a sample of pure states with near-zero degree of entanglement. The result is total conversion of noise from turbulence into loss of photon counts. An additional benefit of this scheme lies in its robustness, as the fidelity of the distilled states does not decay with increasing turbulence.

In Chapter 6 we address the issue of photon loss in high-dimensional quantum key distribution with classically entangled states. We present a deterministic detector for vector vortex modes that maps spatial modes to position. Unlike common detection schemes for vector modes, our approach does not carry the penalty of dimension dependent losses that result in lower sifting rates with increasing dimension. We illustrate our technique by performing a four-dimensional quantum key distribution protocol.

Finally, we conclude by summarising the findings of our research and place them in perspective with regards to current trends in the field.

Chapter 2

Tailoring and measuring classically entangled states

This Chapter contains extracts from three publications by **Bienvenu Ndagano** *et al.*

1. "Creation and detection of vector vortex modes for classical and quantum communication". Journal of Lightwave Technology, 36:292, 2018.
2. "A review of complex vector light fields and their applications". *Journal of Optics*, 20:123001, 2018.
3. "Concepts in quantum state tomography and classical implementation with intense light: a tutorial". *Advances in Optics and Photonics*, **11**:67, 2019

In this Chapter we describe methods to generate and measure classically entangled states of light. We review some modern techniques to produce vector vortex beams through dynamic phase control with spatial light modulators, and geometric phase control with q-plates. Exploiting the linearity of the generation process, we explain and demonstrate the measurement of vector beams by vector mode decomposition; that is, we expand an arbitrary vector field in a basis of classically entangled modes. This provides the means to quantitatively analyse and reconstruct arbitrary vector fields. Lastly we exploit the similarities between quantum and classical entanglement and borrow tools from the quantum realm to show quantum state tomography applied to classical light. We build the approach from single to two-qubit state, before introducing the adaptation to classically entangled light.

2.1 Generation of classically entangled light

Vector vortex beams have long been created internal to lasers by exploiting gain competition in birefringent laser crystals [18] and more recently with geometric phase [41] and with structured materials in on-chip solutions [42–46]. While we acknowledge that such custom solutions exist, they are not common to most laboratories. Here we consider more standard and accessible approaches to the creation of such modes.

2.1.1 Dynamic phase control

A general vector vortex beam can be expressed in the following manner:

$$|\psi\rangle = \cos(\theta/2)\,|\ell\rangle\,|R\rangle + \exp(i\varphi)\sin(\theta/2)\,|-\ell\rangle\,|L\rangle. \tag{2.1}$$

From Eq. 2.1, one deduces that in order to generate a vector beam though dynamic phase manipulation requires a device that can independently modulate the two polarisation components. This can be achieved using a spatial light modulators (SLMs); These are liquid crystal displays that can manipulate, through appropriate modulation, both the amplitude and phase of light. Using SLMs, the optical phase of the incident light is spatially controlled by adjusting the voltage across each pixel on the SLM display. This in turn changes the orientation of the liquid crystals and hence the induced phase by virtue of birefringence. For every pixel, the locally induced phase modulation is given by [47]

$$\phi(V) = \frac{2\pi}{\lambda} d\,[n_e(V) - n_o]\,, \tag{2.2}$$

where λ is the wavelength of the incident light and d is the thickness of the pixel. The extraordinary refractive index, n_e, varies with the applied voltage V, while the ordinary refractive index, n_o, is constant. By spatially controlling the refractive index of the pixels on the SLM display, one can spatially tailor the optical phase incurred on an incident laser beam. Additionally, through appropriate modulation schemes, one can program the SLM to shape the light not only in phase, but also in amplitude [48]. A review of the techniques used to tailor optical fields in both phase and amplitude with computer generated holograms encoded on SLMs is presented in Refs. [18, 49]. The birefringent liquid crystals only allow phase modulation of one polarisation component and so special tricks are needed to overcome this for vector beam generation [49]. Note that it has been shown that spatial modes can also be generated with digital micromirrors [50–52].

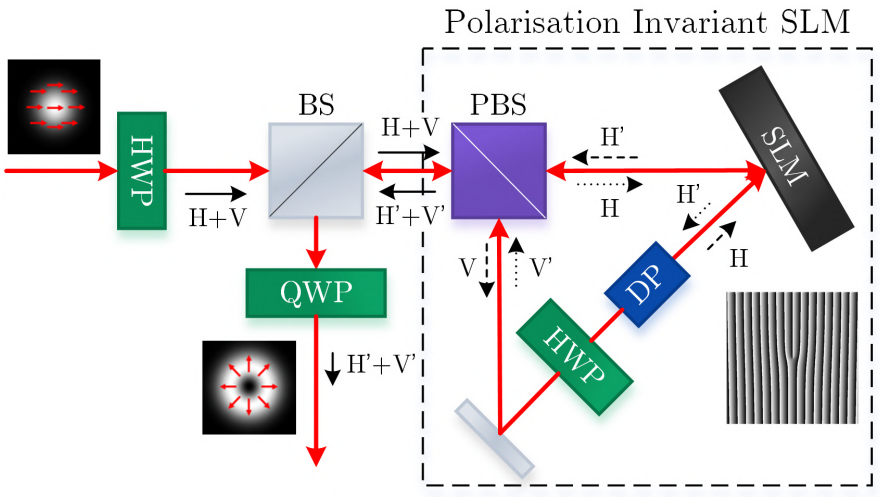


FIGURE 2.1: An incident polarised laser beam is spatially divided in horizontal and vertical polarisation components using a polarising beam splitter (PBS), each of which is modulated by a single hologram encoded on an SLM, placed inside a Sagnac interferometer. The dove prism (DP) ensured that the two OAM modes produced have opposite charge ℓ. BS: 50:50 beam splitter; HWP: half-wave plate; QWP: quarter-wave plate. H, H', V and V' denote the polarisation paths before and after the SLM.

Early use of SLMs to tailor vector vortex beams involved placing them inside an interferometer, as first demonstrated by Neil *et al.* [53]. By splitting the beam into orthogonal polarisations, one can align the polarisation axes of the two beams to match the SLM, independently modulate the two beams before recombination at a later stage, as shown in Fig. 2.1. Due to the difference in the number of reflections after the beam interacting with the hologram encoded on the SLM, each polarisation component acquires opposite OAM values. This approach was later generalised in [54]. Other variants of the generation of vector modes with SLMs involve a double pass on each of the two different hologram [55]. In between each pass, the polarisation is rotated to allow modulation of only one polarisation component.

Spatial light modulators have the inconvenience of high losses, since only the first diffracted order contains the desired modulation. The independent modulation could be realised with the use of spiral phase plates. However, they are non-trivial to manufacture for optical wavelengths and are offer no versatility in terms of operating wavelength and spatial mode produced (unlike an SLM).

2.1.2 Geometric phase control

From the early work of Beth it was known that spin angular momentum (circular polarisation) could be transferred to matter, which he demonstrated by passing circularly polarised light through an anisotropic birefringent plate [12]. Much later it was shown

that optical orbital angular momentum could be transferred to matter [56, 57]. Interestingly, both spin and orbital angular momentum can be coupled in a medium that is both anisotropic and inhomogeneous, inducing spatially variant polarisation transformations. It was shown by Bomzon *et al.* that space-variant polarisation control can be achieved using sub-wavelength gratings [58]. Since the period of the grating is smaller than the wavelength of the incident light, each groove acts as a polariser where the transmission axis varies across the profile of the beam.

Later, Biener *et al.* showed that the spatially varying polarisation transformations are accompanied by an optical phase change resulting from the geometry of the sub-wavelength structure [59]. This is a manifestation of the Pancharatnam-Berry geometric phase [60, 61]. Biener *et al.* expressed the electric field $|E_{out}\rangle$ at the output of the subwavelength dielectric grating, given an input arbitrary polarised plane wave $|E_{in}\rangle$, as follows

$$|E_{out}\rangle = \sqrt{\eta_E}\,|E_{in}\rangle + \sqrt{\eta_R}\exp(i2\theta(r,\omega))\,|R\rangle + \sqrt{\eta_L}\exp(-i2\theta(r,\omega))\,|L\rangle, \tag{2.3}$$

where η_E, η_R and η_L are the polarisation order coupling efficiencies. Interestingly, the right- and left-circular polarisation component acquire conjugate optical phase. Through appropriate design of the grating structure it is possible to have $\eta_E \to 0$ and $\theta = q\phi$, where ϕ is the azimuthal angle. The resulting optical element becomes one that performs the following polarisation-to-OAM coupling:

$$E_{in}\,|R\rangle \;\to\; E_{in}\exp(-i2q\phi)\,|L\rangle, \tag{2.4}$$

$$E_{in}\,|L\rangle \;\to\; E_{in}\exp(+i2q\phi)\,|R\rangle. \tag{2.5}$$

Given an input (left-) right-circularly polarised state incident on such an optical element, the result is a total polarisation conversion to an output beam that is (right-) left-circularly polarised and carries a topological charge $2q$. The design of such an element, commonly known as a q-plate, was demonstrated by Marrucci *et al.* [62]. Instead of sub-wavelength gratings, Marrucci *et al.* used birefringent liquid crystals that can be dynamically aligned with an external electric, magnetic or optical field. A detailed discussion on the manufacturing process is reported in Ref. [63].

Since their invention, q-plates have simplified the generation of vector beams. For example, suppose one illuminates the q-plate with a field that is a superposition of the input fields in Eqs. 2.4 and 2.5: $|E_{in}\rangle = E_{in}\left(\sqrt{\alpha}\,|R\rangle + \sqrt{1-\alpha}\exp(i\gamma)\,|L\rangle\right)$, with $0 \le \alpha \le 1$.

The resulting field can be expressed as follows:

$$E_{out} = E_{in}\left[\sqrt{\alpha}\exp(-i2q\phi)\,|L\rangle + \sqrt{1-\alpha}\exp(i\gamma)\exp(i2q\phi)\,|R\rangle\right], \tag{2.6}$$

Thus, by controlling the phase γ and the charge q, one can generate a wide variety of vector vortex beams. For a given q value, the space of vector modes described by Eq. 2.6 can be mapped on a higher-order Poincaré sphere [38, 40].

Two of the limitations of the q-plate is that the spin-orbit coupling is only applicable for input circular polarisation states, and the output spatial frequencies on the left- and right-circular polarisation states are constrained to be conjugate of each of other. Recently, these were overcome with the design of a metamaterial J-plate, that performs arbitrary spin-orbit coupling independently of the input polarisation state [64, 65]. The sub-wavelength structure allows for near continuous control of spatial phase shifts, birefringence and the orientation of the fast axis. This results in the design of an optical element capable of the following transformation

$$E_{in}\,|\sigma^{+}\rangle \;\rightarrow\; E_{in}\exp(im\phi)\,|(\sigma^{+})^{*}\rangle, \tag{2.7}$$

$$E_{in}\,|\sigma^{-}\rangle \;\rightarrow\; E_{in}\exp(in\phi)\,|(\sigma^{-})^{*}\rangle, \tag{2.8}$$

where $|\sigma^{\pm}\rangle$ are the eigenstates of polarisation in an arbitrary basis (linear or circular). The fact that it is metamaterial-based also makes it attractive for integration onto small scale devices. For a good review of vector beams and their applications, see Ref [66].

2.1.3 Vector mode decomposition

The modal decomposition of an arbitrary electric field has been extensively demonstrated in the case of scalar (uniformly polarised) modes [18, 67–69]. An arbitrary electric field can be represented as a superposition of any orthonormal and complete basis. Measuring the coefficients in the expansion of the basis is the aim of modal decomposition. From this all physical properties of the optical field can be inferred quantitatively, such as the OAM density, Poynting vector, intensity, wavefront, phase and so on. In previous work, this approach has been performed with scalar basis states (Laguerre-Gaussian modes, vortex modes, etc). Given that vector modes combine both spatial modes and polarisation, the basis states can naturally be constructed from the product of basis

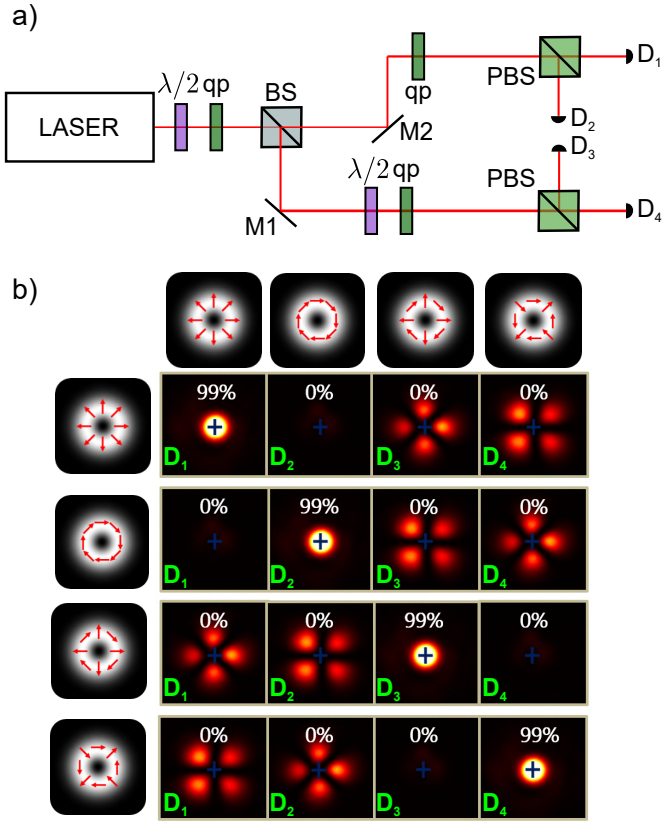


FIGURE 2.2: Experimental Modal decomposition of vector vortex modes in the $\ell = \pm 1$ subspace. Vector modes produced with a half-wave plate($\lambda/2$) and q-plate (qp) are analysed with a vector mode decomposition system. The measurement outcomes are collected at detectors D_1 to D_4 placed after polarisation beam-splitter (PBS). M1 and M2 are mirrors.

states of the two degrees of freedom. One can write

$$E_{in}(\mathbf{r}) = \sum_{m=-\infty}^{\infty} c_m \psi_m(\mathbf{r})\hat{\sigma}^+ + \sum_{n=-\infty}^{\infty} c_n \psi_n(\mathbf{r})\hat{\sigma}^-, \tag{2.9}$$

where $\hat{\sigma}^{\pm}$ are polarisation states and $\{\psi_m\}$ is an orthonormal basis. By measuring the coefficients c_m and c_n, one can reconstruct the input vector beam E_{in}. Alternatively, one can take advantage of the superposition principle: if $\psi_m(\mathbf{r})\hat{\sigma}^{\pm}$ is an eigenstate of E_{in}, then a normalised superposition of these eigenstates also forms a basis for E_{in}. As such, one can construct a basis where the eigenstates are vector modes Ψ_ℓ:

$$\Psi_{\ell,\gamma}(\mathbf{r}) = \frac{1}{\sqrt{2}}\left[\psi_\ell(\mathbf{r})\hat{\sigma}^+ + \exp(i\gamma)\psi^*_\ell(\mathbf{r})\hat{\sigma}^-\right], \tag{2.10}$$

with $\gamma = \{0, \pi\}$. The input vector mode in Eq. 2.9 can thus be expressed as follows:

$$E_{in}(\mathbf{r}) = \sum_{\ell=-\infty}^{\infty} c_{\ell,\gamma}\Psi_{\ell,\gamma}(\mathbf{r}), \tag{2.11}$$

where the magnitude of the coefficients in the expansion can be obtained through an inner product measurement. This is performed by (i) passing the incident beam through a modal filter $\Psi^{\dagger}_{k,\gamma}$, (ii) Fourier transforming the output and (iii) measuring the on-axis intensity:

$$E_{in} \rightarrow \Psi^{\dagger}_{k,\gamma} E_{in} \rightarrow \int d\mathbf{r}\ E_{in}(\mathbf{r}) \Psi^{*}_{k,\gamma}(\mathbf{r}) \exp(i\mathbf{K}\cdot\mathbf{r}) \rightarrow \left| \int d\mathbf{r}\ E_{in}(\mathbf{r}) \Psi^{*}_{k,\gamma}(\mathbf{r}) \right|^2 = |c_{k,\gamma}|^2 \tag{2.12}$$

This approach was reported in [70] and is shown in Fig. 2.2. In practice, the on-axis position would correspond to a few pixels on a CCD camera. An alternative to the camera would be to use a single-mode fibre to collect the light at the on-axis position. This method was used by Milione *et al.* [71] to demonstrate 20 Gbits/s information transfer over 4 multiplexed vector beams.

2.2 Quantum state tomography

Quantum state tomography (QST) as we know it was introduced in the late 80s to obtain the Wigner distribution by tomographic measurements of quadrature amplitudes [72], taking into account the direct correspondence between the Wigner function and the density matrix of any desired quantum state [73, 74]. Other methods to determine the quantum state were proposed [75, 76], studying also the open question of the impossibility to determine the probability distributions of a superposition quantum state with a direct measurement [77].

The QST projective measurement has been vastly used to characterise a myriad of quantum states [78–84]. Importantly, QST has become essential in the characterisation of entanglement sources from a qualitative point of view, e.g. entanglement sources using photons [85–91], atoms [92, 93], and even with molecular vibrational modes [94]. However, the polarisation of a photon is the most commonly known degree of freedom (DoF) used to encode a quantum state, due to the great variety and availability of high efficiency polarisation control elements. Consequently many experimental milestones in quantum optics have been accomplished by using the polarisation degree of freedom [95–98].

Although QSTs have been performed on many quantum systems, in this Thesis we will consider photonic quantum states, exploiting the spatial mode and polarisation DoFs of light. QSTs have been performed extensively on the latter (see for example [87, 90, 99, 100]) while other DoFs are becoming more prevalent these days, e.g., entangled spatial modes [101, 102] for improved communication security [25, 103, 104] and

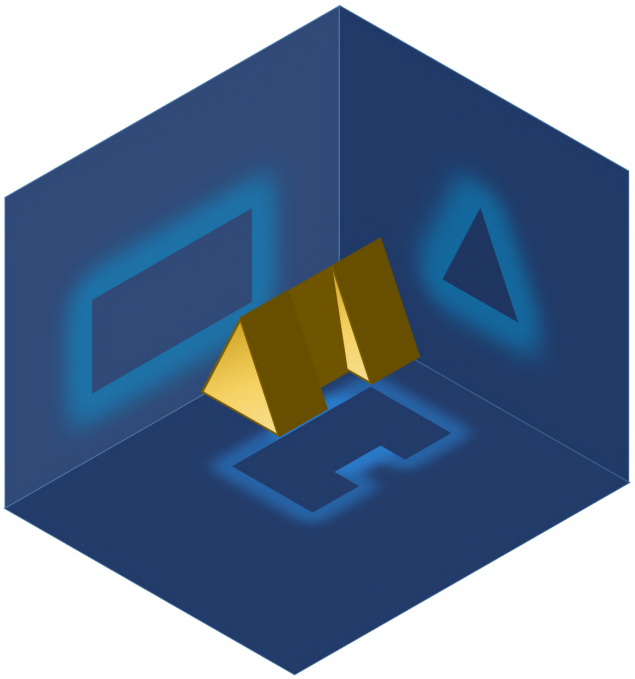


FIGURE 2.3: A QST attempts to reconstruct a potentially complex quantum state by a series of simple projective measurements. This is analogous to trying to reconstruct a complicated object by only considering its shadow from various angles.

high-dimensional entanglement [105, 106]. Although high-dimensional quantum state generation is increasingly relevant nowadays, the characterisation of such systems is extremely complex due to the exponential increase of projections with dimension. Nevertheless, QSTs have been successfully demonstrated on high-dimensional spatial mode entanglement using various projection approaches [107–109].

Examining an unknown quantum state is a tricky business [110–112], primarily due to the measurement problem in quantum mechanics [113, 114]. First, a measurement destroys the information of the state, or at the very least perturbs it [115], so multiple measurements on the same state is not possible [116]. Second, it is not possible to clone the state one wishes to study so that the measurements can be made on exact copies [167]. Third, the state is in general unknown – it could be pure or mixed, high-dimensional or low-dimensional – and so a choice of basis and measurement sequence is not trivial [117–120]. The consequence is that we can infer only a little information at a time by probing a particular aspect of a quantum state [121]: only one question can be asked (a measurement) from which we get one piece of information (the measurement outcome). The standard tool to do this, i.e., unravel some quantum state by multiple measurements, is a quantum state tomography (see [14, 110] for good reviews). The so-called projective measurements are very similar to the well-known computed tomography "CT" scans in medicine [122]: once many measurements are made, each probing a particular aspect of the possible state, the complete quantum state is built up through a

tomographic process. In essence, each unknown quantum state is "sliced" and completely characterised through a series of projective measurements in different bases, retrieving the information of a new dimension for each measurement [123]. It is akin to building up an image of a complex object by making only simple projections of its shadow, as illustrated in Fig. 2.3. From all the shadows we see, we can work out the shape of the object. In the quantum case the outcome is a complete set of observables whose probabilistically weighted outcome fully describes the quantum state [13]. This then becomes an inverse problem: knowing the outcome of every question (the outcomes of our measurements), can we work out what the "object" is? In the quantum world this often translates into determining a density matrix for the quantum state from which all other required information can be inferred [123–125].

2.3 Quantum state tomography of a single qubit

The objective of a QST is to reconstruct the density matrix of an arbitrary state using an appropriate set of measurements, regardless of whether the state is pure or mixed [87, 117, 126, 127]. It is this broad applicability that makes QST such a powerful tool in quantum information and communication. The procedure behind a QST for two-dimensional quantum states consists of locating the qubit state on the Poincaré/Bloch sphere; that is, as mentioned before, characterising the rotation angles about the x-, y- and z-axes. Recall the expression of a single qubit density matrix in terms of Pauli matrices:

$$\rho = \frac{1}{2}\sum_{n=0}^{3} \rho_n \sigma_n, \tag{2.13}$$

where ρ_n are the expectation values of the matrices σ_n, and are obtained from

$$\mathrm{tr}\left(\rho\sigma_n\right) = \frac{1}{2}\mathrm{tr}\left(\sum_{m=0}^{3}\rho_m\sigma_m\sigma_n\right) = \frac{1}{2}\sum_{m=0}^{3}\rho_m \mathrm{tr}\left(\sigma_m\sigma_n\right) = \sum_{m=0}^{3}\rho_m\delta_{m,n} = \rho_n. \tag{2.14}$$

Thus providing that one can obtain the expectation values, ρ_n, it is then trivial to reconstruct the density matrix of the system. However, one first needs to clarify the measurement procedure that leads to the computation of ρ_n. To do so, it is useful to express the matrices σ_n in terms of eigenvalues and eigenvectors which, as we will show, correspond to physical states that can be measured directly.

The matrices σ_n each have two eigenvectors, $\left|\lambda_n^0\right\rangle$ and $\left|\lambda_n^1\right\rangle$, with eigenvalues α_n^0 and α_n^1, and thus can be expressed as

$$\sigma_n = \alpha_n^0|\lambda_n^0\rangle\langle\lambda_n^0| + \alpha_n^1|\lambda_n^1\rangle\langle\lambda_n^1|. \tag{2.15}$$

TABLE 2.1: Eigenvectors and eigenvalues of the identity and Pauli matrices in the polarisation basis.

Matrices σ_n	α_n^0	$\lvert\lambda_n^0\rangle$	α_n^1	$\lvert\lambda_n^1\rangle$
σ_0	1	$\lvert L\rangle \equiv \begin{pmatrix}0\\1\end{pmatrix}$	1	$\lvert R\rangle \equiv \begin{pmatrix}1\\0\end{pmatrix}$
σ_1	-1	$\lvert V\rangle \equiv \frac{1}{\sqrt{2}}\begin{pmatrix}1\\-1\end{pmatrix}$	1	$\lvert H\rangle \equiv \frac{1}{\sqrt{2}}\begin{pmatrix}1\\1\end{pmatrix}$
σ_2	-1	$\lvert A\rangle \equiv \frac{-i}{\sqrt{2}}\begin{pmatrix}1\\-i\end{pmatrix}$	1	$\lvert D\rangle \equiv \frac{-i}{\sqrt{2}}\begin{pmatrix}1\\i\end{pmatrix}$
σ_3	-1	$\lvert L\rangle \equiv \begin{pmatrix}0\\1\end{pmatrix}$	1	$\lvert R\rangle \equiv \begin{pmatrix}1\\0\end{pmatrix}$

Based on this decomposition, we can express the expectation values in Eq. 2.14 as

$$\rho_n = \mathrm{tr}\,(\rho\sigma_n) = \alpha_n^0 \,\langle\lambda_n^0|\,\rho\,|\lambda_n^0\rangle + \alpha_n^1 \,\langle\lambda_n^1|\,\rho\,|\lambda_n^1\rangle. \tag{2.16}$$

The matrices $|\lambda_n\rangle\langle\lambda_n|$ are called projectors; these are Hermitian and positive operators that form a complete orthonormal set [1]. This is a rather dense description so let us go through each property one by one.

1. *Hermiticity*: Projectors are self-adjoint operators, i.e., they are equal to their own conjugate transpose, and have real expectation values. This is a fundamental requirement for projectors to be physical observables.

2. *Positivity*: Positive operators have expectation values greater or equal to 0. This is a natural requirement for projectors given that their expectation values correspond to probabilities.

3. *Completeness*: $\sum_m |\lambda_n^m\rangle\langle\lambda_n^m| = \sigma_0$. This is a requirement for conservation of probability.

4. *Orthonormality*: $|\lambda_n^m\rangle\langle\lambda_n^m||\lambda_n^l\rangle\langle\lambda_n^l| = |\lambda_n^m\rangle\langle\lambda_n^m|\delta_{l,n}$. This is not a physical requirement but implies that the eigenstates of two projectors within a complete set have no overlap.

From their definition, one can easily compute the eigenvalues of the matrices σ_n and show that they are ± 1, as shown in Table 2.1. Interestingly, the eigenvectors correspond to the polarisation states on the surface of the Poincaré sphere, previously shown in Fig. 1.1. We now have the recipe to compute the expectation values of the σ_n matrices in terms of direct measurement that can be performed on the quantum state, and it is

as follows:

$$\rho_0 = \mathrm{tr}\,(\rho\sigma_0) = \langle L|\,\rho\,|L\rangle + \langle R|\,\rho\,|R\rangle, \tag{2.17}$$

$$\rho_1 = \mathrm{tr}\,(\rho\sigma_1) = \langle H|\,\rho\,|H\rangle - \langle V|\,\rho\,|V\rangle, \tag{2.18}$$

$$\rho_2 = \mathrm{tr}\,(\rho\sigma_2) = \langle D|\,\rho\,|D\rangle - \langle A|\,\rho\,|A\rangle, \tag{2.19}$$

$$\rho_3 = \mathrm{tr}\,(\rho\sigma_3) = \langle L|\,\rho\,|L\rangle - \langle R|\,\rho\,|R\rangle. \tag{2.20}$$

Observe however that the measurements required to compute ρ_0 are the same as that of ρ_3. In fact, $\mathrm{tr}\,(\rho\sigma_0)$ is an expression of the conservation of probability. Given that projectors of a given Pauli matrices form a complete set, the conservation of probability is independent of the measurement basis. Thus one can deduce that ρ_0 can be obtained in a similar manner from the projective measurements of ρ_1 and ρ_2. Thus the state tomography of a single qubit requires a total of 6 projective measurements: $d(d+1)$ as mentioned in the introduction, for $d = 2$.

A QST of an OAM qubit follows the same procedure as that outlined for polarisation qubit. The density matrix is expanded in terms of Pauli matrices and the identity, however, the eigenvectors now take a different meaning; rather than polarisation states, they now correspond to OAM modes and their superpositions, as shown in Table 2.2.

TABLE 2.2: Eigenvectors and eigenvalues of the identity and Pauli matrices in the OAM basis.

Matrices σ_n	α_n^0	$\lvert\lambda_n^0\rangle$	α_n^1	$\lvert\lambda_n^1\rangle$
σ_0	1	 $\equiv \begin{pmatrix}0\\1\end{pmatrix}$	1	 $\equiv \begin{pmatrix}1\\0\end{pmatrix}$
σ_1	-1	 $\equiv \frac{1}{\sqrt{2}}\begin{pmatrix}1\\-1\end{pmatrix}$	1	 $\equiv \frac{1}{\sqrt{2}}\begin{pmatrix}1\\1\end{pmatrix}$
σ_2	-1	 $\equiv \frac{-i}{\sqrt{2}}\begin{pmatrix}1\\-i\end{pmatrix}$	1	 $\equiv \frac{-i}{\sqrt{2}}\begin{pmatrix}1\\i\end{pmatrix}$
σ_3	-1	 $\equiv \begin{pmatrix}0\\1\end{pmatrix}$	1	 $\equiv \begin{pmatrix}1\\0\end{pmatrix}$

Means to perform projective measurements on these spatial modes have been extensively reported for quantum [128] and classical light [18, 68, 69, 129–131]. Progress in liquid crystal technology and digital micromirror devices has made it possible to generate and detect arbitrary spatial modes using digital holograms (see [18] and [49] for a comprehensive review and tutorial). This has opened avenues for an all-digital realisation of QST with spatial modes. The core idea is to consider the pattern creation step but in reverse. If a particular hologram were to convert a Gaussian mode into a desired pattern, then in reverse the same hologram will convert the pattern into a Gaussian. As Gaussians are the only modes that couple into single-mode fibre (SMF),

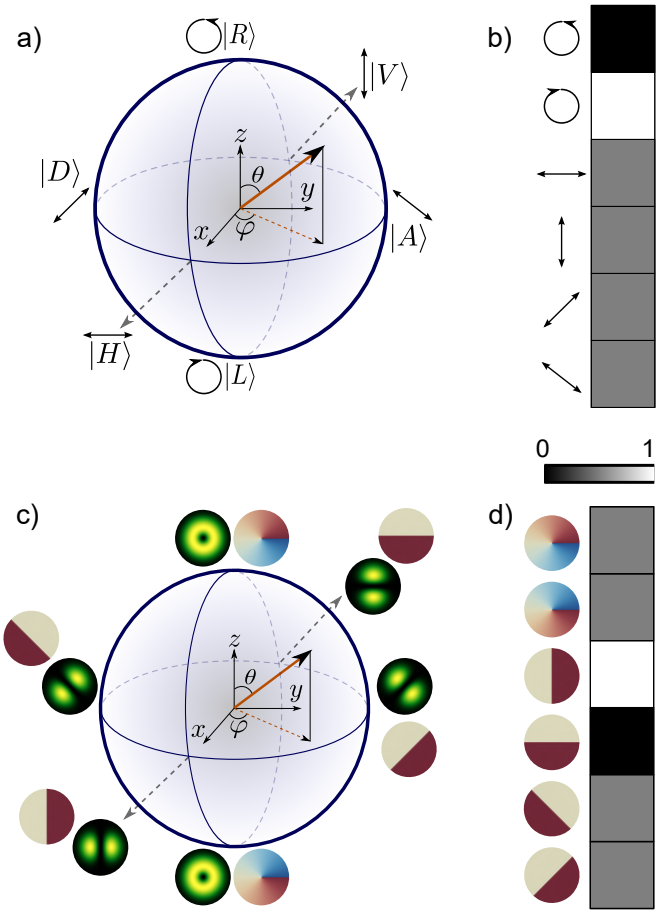


FIGURE 2.4: (a) Representation of polarisation states on the Poincaré sphere. (b) Shows the normalised outcomes of projective measurements onto the eigenstates of the Pauli matrices, for given horizontally polarised state. (c) Representation of OAM qubit states on the OAM Bloch sphere. (d) From projective measurement onto spatial modes, one performs the quantum state tomography of an OAM state $(|1\rangle + |-1\rangle)/\sqrt{2}$.

we have the means of a "pattern sensitive" detector. Sample QST measurements are shown in Fig. 2.4 for a left-circularly polarised qubit state and an OAM superposition state $(|\ell = 1\rangle + |\ell = -1\rangle)/\sqrt{2}$.

Notice that we approximate the projective measurement of superposition states on the equator of the OAM Bloch sphere as $\arg[|\ell\rangle + \exp(i\varphi)\,|-\ell\rangle]$, producing a binary phase pattern rather than an amplitude function. This is why all the Pauli matrices in Table 2.2 are phase-only patterns. In general the OAM example can be replaced with arbitrary modes by substituting $|\ell\rangle \rightarrow |M_1\rangle$ and $|-\ell\rangle \rightarrow |M_2\rangle$ everywhere in the above analysis.

2.4 Tomography of quantum entangled spatial modes

Recall the expression of a two-qubit density matrix in terms of Pauli matrices:

$$\rho = \left(\frac{1}{2}\sum_{m=0}^{3}\rho_m\sigma_m\right)_A \otimes \left(\frac{1}{2}\sum_{n=0}^{3}\rho_n\sigma_n\right)_B = \frac{1}{4}\sum_{m,n=0}^{3}\rho_{mn}\ \sigma_m\otimes\sigma_n. \tag{2.21}$$

Once again, the task of a QST is to realise direct measurements to compute the expectation values ρ_{mn}. We follow the same tensor product construction of the expectation value to express ρ_{mn} in terms of eigenvalues and eigenvectors of the basis operators for the joint system, $\sigma_m \otimes \sigma_n$, with

$$\sigma_m\otimes\sigma_n = \left(\alpha_m^0|\lambda_m^0\rangle\langle\lambda_m^0| + \alpha_m^1|\lambda_m^1\rangle\langle\lambda_m^1|\right)\otimes\left(\alpha_n^0|\lambda_n^0\rangle\langle\lambda_n^0| + \alpha_n^1|\lambda_n^1\rangle\langle\lambda_n^1|\right). \tag{2.22}$$

By expanding the expression above, the measurements required in a QST can be directly read:

$$\begin{aligned}\sigma_m\otimes\sigma_n =& \alpha_m^0\alpha_n^0|\lambda_m^0\rangle\langle\lambda_m^0|\otimes|\lambda_n^0\rangle\langle\lambda_n^0| + \alpha_m^1\alpha_n^1|\lambda_m^1\rangle\langle\lambda_m^1|\otimes|\lambda_n^1\rangle\langle\lambda_n^1| + \\ & \alpha_m^1\alpha_n^0|\lambda_m^1\rangle\langle\lambda_m^1|\otimes|\lambda_n^0\rangle\langle\lambda_n^0| + \alpha_m^0\alpha_n^1|\lambda_m^0\rangle\langle\lambda_m^0|\otimes|\lambda_n^1\rangle\langle\lambda_n^1|.\end{aligned} \tag{2.23}$$

The projectors $|\lambda_m\rangle\langle\lambda_m|$ have been discussed in the previous section and we have shown that they can be realised through direct measurement on the quantum state. In the case of two qubits, the tensor product $|\lambda_m\rangle\langle\lambda_m|\otimes|\lambda_n\rangle\langle\lambda_n|$ means that one must perform joint projective measurements on the two photons of an entangled pair. Practically, this implies that the projective measurements must be done in coincidence. This can be done using single photon detectors and a counting module. The expectation values ρ_{mn} then take the following form:

$$\begin{aligned}\rho_{mn} =& \alpha_m^0\alpha_n^0\ \langle\lambda_m^0\lambda_n^0|\,\rho\,|\lambda_m^0\lambda_n^0\rangle + \alpha_m^1\alpha_n^1\ \langle\lambda_m^1\lambda_n^1|\,\rho\,|\lambda_m^1\lambda_n^1\rangle + \\ & \alpha_m^1\alpha_n^0\ \langle\lambda_m^1\lambda_n^0|\,\rho\,|\lambda_m^1\lambda_n^0\rangle + \alpha_m^0\alpha_n^1\ \langle\lambda_m^0\lambda_n^1|\,\rho\,|\lambda_m^0\lambda_n^1\rangle.\end{aligned} \tag{2.24}$$

In the above, we have used a compact notation for the projective measurement, where $|\lambda_m^0\lambda_n^0\rangle \equiv |\lambda_m^0\rangle\otimes|\lambda_n^0\rangle$. Note the order of the eigenstate in both the bra and ket in the expression of the expectation value: the first ket (bra) refers to a state (projection) of (on) particle A, while the second ket (bra) applies to particle B. For example, the expectation value $\langle\lambda_m^0\lambda_n^1|\,\rho\,|\lambda_m^0\lambda_n^1\rangle$ is obtained by projecting photons A and B on the state $|\lambda_m^0\rangle$ and $|\lambda_n^1\rangle$, respectively, and measuring in coincidence. The eigenvalues α_m and eigenvectors $|\lambda_m\rangle$ are known from the single qubit QST, we can thus write the expression of the different expectation values ρ_{mn} in terms of direct projective measurements. With four measurements per expectation value, one would in principle perform a total of 64 measurements. However, upon close examination of the expectation values, one

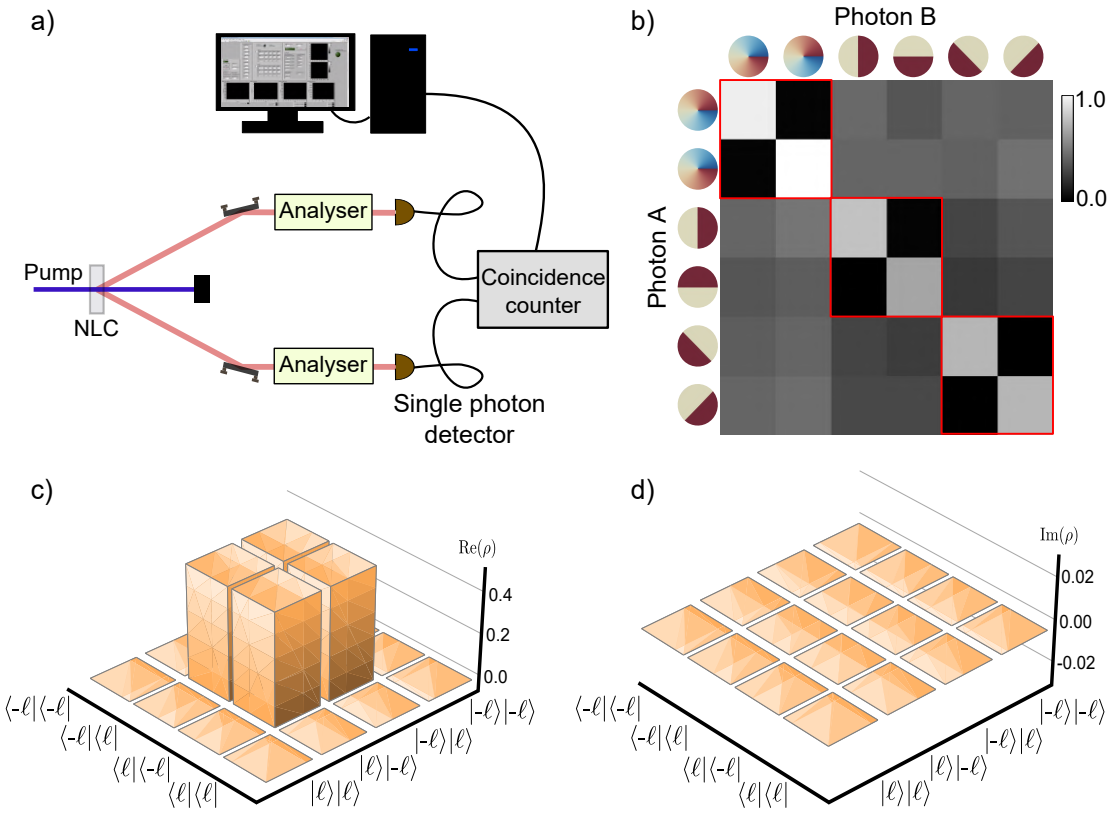


FIGURE 2.5: Quantum state tomography of a two-photon state. (a) shows an experimental setup to generate entangled two-photon states through spontaneous parametric down-conversion in a non-linear crystal (NLC). The down-converted photons travel to two OAM analysers and their quantum states are measured in coincidence. (b) Shows a two-qubit QST where the projected state of each photon in the entangled pair is indicated by their phase map. The colour of each box represents the normalised coincidence counts for a given set of projection on the two-photon state. Using the tomographic data, the density matrix is computed and its real and imaginary components are shown in (c) and (d). The sum of the measurements enclosed by the red squares define the expectation value of the identity (probability conservation)

realises that only a total of 36 measurements are necessary. This is because some of the expectation values share a common set of measurements. Recall from single qubit QST that the projectors of the identity matrix are the same as that of any single Pauli matrix. Therefore by measuring the expectation value ρ_{mn} for $m, n > 0$, one can compute ρ_{00}, ρ_{m0} and ρ_{0n}. This is what reduces the number of necessary projective measurements from 64 to 36.

Experimental implementation is, however, not without its own set of challenges. Engineering quantum states is a probabilistic process. A standard method of generating two-photon states that are correlated is through spontaneous parametric down conversion (SPDC), where a non-linear crystal is pumped with photons from a laser, as shown in Fig. 2.5 (a). An entangled pair is produced with a certain probability depending on the type of non-linear crystal used. This results in fluctuations in photon number

measured by the single photon detectors, resulting in experimental errors that affect the reconstruction of the quantum state. Statistical techniques can be employed to mitigate these errors, one commonly used being the maximum likelihood estimation [128]. The principles of the method are as follows:

1. One performs the tomographic measurements on the quantum state.
2. Guess a physical density matrix for the state (Hermitian with unit trace and non-negative eigenvalues).
3. Computationally perform a state tomography on the guessed density matrix.
4. Compute the difference between the guessed and experimental tomographic measurements: $\chi^2 = \left(\sum_{i=1}^{36} \frac{C^i_{\text{exp}} - C^i_{\text{guess}}}{\sqrt{C^i_{\text{exp}}+1}}\right)^2$, where the superscript i refers to the i^{th} tomographic projections. The experimental tomographic measurements are labelled C^i_{exp} while those simulated based on the guessed density matrix are labelled C^i_{guess}.
5. Update the guessed density matrix such that it minimises the χ^2 difference.

This procedure ensures that the reconstructed density matrices meet the criteria required to be physical; i.e., the density matrix is Hermitian with non-negative eigenvalues. An example of a state tomography of OAM entangled photon pairs is shown in Fig. 2.5(b). Using the maximum likelihood estimation, one reconstructs the real and imaginary components of the density matrix shown in Figs. 2.5(c) and (d), respectively.

2.5 Classical implementation of quantum state tomography

Given the mathematical similarities between quantum entangled states and vector beams, there has been an interest in using classical states of light to model local quantum entanglement dynamics [132–135]. This requires some commonality between the quantum and classical system in the way they are analysed in order to make a fair comparison. In the previous section we have identified QST as the tool of choice for quantum state reconstruction. Fortunately, the procedure behind QST of a bi-photon state can be directly applied to the vector beam [37, 136, 137]. This is because of the mathematical equivalence of the classical and quantum states. The only adaptation is in terms of the projective measurements required: now in series on one classical beam rather than on two photons. So let us go through the procedure of state tomography of a vector beam. Recall the expression of a vector beam

$$|\psi\rangle = \cos(\theta/2)\,|\ell\rangle\,|R\rangle + \exp(i\varphi)\sin(\theta/2)\,|-\ell\rangle\,|L\rangle. \tag{2.25}$$

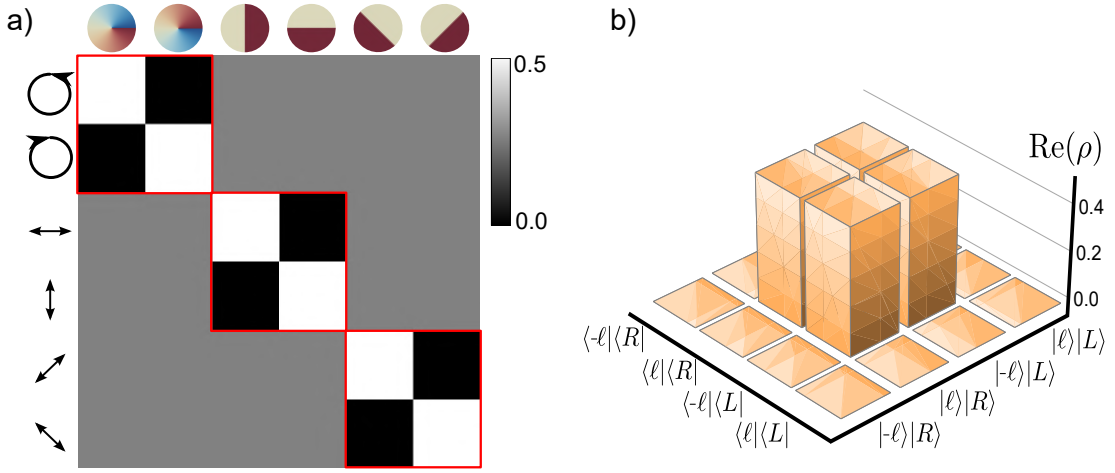


FIGURE 2.6: State tomography of a classical vector beam. (a) Shows the projective measurements on the polarisation and spatial mode degrees of freedom. (b) From these projections, the density matrix is reconstructed.

We have shown previously that the above state can be described as a point on the surface of a higher-order Poincaré sphere. We have demonstrated that the HOPS is constructed from the tensor product of the eigenstates of the individual subsystems. Here, the two systems correspond to degrees of freedom of a classical beam; these are hybrid states of OAM and polarisation. Previously we expressed the density matrix of a vector mode as

$$\rho = \left(\frac{1}{2}\sum_{m=0}^{3}\rho_m\sigma_m\right)^{\text{orbit}} \otimes \left(\frac{1}{2}\sum_{n=0}^{3}\rho_n\sigma_n\right)^{\text{spin}} = \frac{1}{4}\sum_{m,n=0}^{3}\rho_{mn}\ \sigma_m^{\text{orbit}} \otimes \sigma_n^{\text{spin}}. \tag{2.26}$$

The projective measurements necessary for a QST of the classical vector beam are the same as those of the bi-photon case, with the exception that the set of eigenstates correspond to polarisation and spatial modes, as depicted in Fig. 2.6. Let us return to the usual entanglement case, say bi-photons entangled in OAM: we have one degree of freedom and two photons. The QST is then based on projections in one degree of freedom on each of the two photons. In the classically entangled case we have two measurements on one intense beam of light. In the former the measurements are in general non-local, while in the latter they are local.

Consider the outcome of this process, shown in Fig. 2.6(a) for the classically entangled state $|\psi\rangle = (|\ell\rangle|R\rangle + |-\ell\rangle|L\rangle)/\sqrt{2}$. The joint measurements used to compute the expectation value of the identity operator $\sigma_0 \otimes \sigma_0$ are shown enclosed by one of the red squares. From these tomographic measurements, one computes the density matrix, whose real part is shown in Fig. 2.6(b).

2.6 Conclusion

In this Chapter, we have presented tools to tailor and measure classically entangled states of light. We have shown that one can produce arbitrary vector modes by manipulating either the dynamic or geometric phase of light. Dynamic phase control involves tailoring the spatial distribution of light by passing it through a material with either spatially varying thickness or refractive index. However rather than designing a new material for every application, we have discussed the dynamic phase control of light using birefringent liquid-crystal spatial light modulators. These allow one to locally control the refractive index across a pixelated display to produce arbitrary spatial modes, at the click of a button, using digital holograms. While SLMs are polarisation sensitive, we have shown that two orthogonal polarisation states can independently be tailored and superposed to produce a vector beam. Furthermore, we have presented a recent and compact approach to generate vector modes by manipulating the geometric phase of light through spatially varying polarisation transformations. This was followed by the introduction of one such geometric phase element, the q-plate, that maps circular polarisation to OAM. From appropriate choice of input state impinging on the q-plate, one can produce either scalar or vector vortex beams.

The generation of vector modes was complemented by means to quantitatively measure them. The first approach is through vector mode decomposition; that is, an arbitrary field is decomposed in an orthonormal basis of vector modes. We showed theoretically that the projections on the basis vector modes can be realised using a q-plate. This was demonstrated experimentally for vector modes carrying an OAM charge of $|\ell| = 1$. The second approach to measuring vector modes was through a state tomography. This approach exploits the non-separability of vector modes and adapts tools from quantum measurement of entangled states. Through a series of joint projections on the polarisation and spatial degrees of freedom, performed on the classical vector modes, one can reconstruct the density matrix, thus fully characterising the state. We have built the theory of quantum state tomography from the single to the pair of qubit and finally the classically entangled vector mode. In the following Chapter, we will make use of both classical and quantum state tomography to demonstrate the equivalence of quantum and classical entanglement decay through a one sided turbulent channel, thus raising awareness of the potential and the physical nature classical entanglement as a resource.

Chapter 3

Characterising quantum channels with classically entangled light

This Chapter contains extracts from a publication by **Bienvenu Ndagano** *et al.* "Characterizing quantum channels with non-separable states of classical light". *Nature Physics*, 13:397, 2017.

Here we demonstrate a simple approach to characterise a quantum channel using classical light. We exploit the non-separability property of vector beams to show that the state evolution of a classically entangled beam in a one-sided turbulent channel follows a one-to-one correspondence with that of an equivalent quantum entangled state. This proves that beyond the mathematical resemblance to its quantum counter part, classical entanglement does hold physical significance. Moreover, we show that the one-to-one correspondence between one-sided channels and entangled states, the so called Choi-Jamiolkowski isomorphism [138], is also valid for classical light fields with arbitrary degree of entanglement. Thus, a full characterisation of quantum channels can be obtained via state tomography of a classically entangled beams. This new technique enables one, for example, to determine the action of turbulence, and other channels, on pairs of spatial modes for quantum and classical states of light, and replaces the usual process tomography in both cases. Finally, we demonstrate the applicability of the tools in a proof-of-principle communication experiment employing classically entangled states, showing that the characterisation of the channel allows for information recovery and robust data transfer.

3.1 The equivalence of classical and quantum entanglement

Consider a typical scenario where quantum information is shared between two parties (Alice and Bob), as shown in Fig. 3.1. Alice generates two photons entangled in their spatial DoF, which we will take to be the OAM DoF. Her bi-photon state can then be written as: $|\Psi_\ell\rangle_{\text{in}} = |\ell\rangle_A |-\ell\rangle_B + |-\ell\rangle_A |\ell\rangle_B$. She sends one photon to Bob, which passes through the channel; in this study we will consider a free-space link through a turbulent atmosphere as our example, but the concept is not restricted to this particular case and can be adapted to different channels. It has been shown, theoretically and experimentally, that perturbations due to such a channel negatively affect the correlations between the photons, thereby decreasing the efficiency and security of the quantum communication link. In this scenario, photon A experiences the channel while photon B does not. The resulting state $|\Psi_\ell\rangle_{\text{out}}$ of the photon pair carries the complete information about the channel. This is due to the so-called Choi-Jamiolkowski isomorphism, and could be experimentally verified by teleporting states of single photons using the photon pair in state $|\Psi_\ell\rangle_{\text{out}}$ as an entanglement resource. The resulting teleportation channel would reproduce the same state changes as the turbulence channel [139].

We claim that this quantum scenario has a classical equivalent, depicted in Fig 3.1.(b). Here Alice prepares a classical beam that is non-separable in OAM and polarisation: $|\Psi_\ell\rangle_{\text{in}} = |\ell\rangle_A |R\rangle_B + |-\ell\rangle_A |L\rangle_B$, sending the entire beam to Bob through the same channel. In this formalism A and B now refer to the two degrees of freedom in the non-separable light field, and not to two photons in the entangled system. But polarisation is not affected by turbulence, so the DoF that experiences the deleterious effects of the channel is that of the spatial mode (A). In both cases only the states $|\ell\rangle_A$ and $|-\ell\rangle_A$ are affected.

The equivalence of the quantum and classical scenarios, together with the fact that the outgoing state in the quantum case contains the full information about the channel, strongly suggest that such non-separable states of light may be used to characterise the effect of the channel on the quantum state, an idea which we later validate theoretically and experimentally.

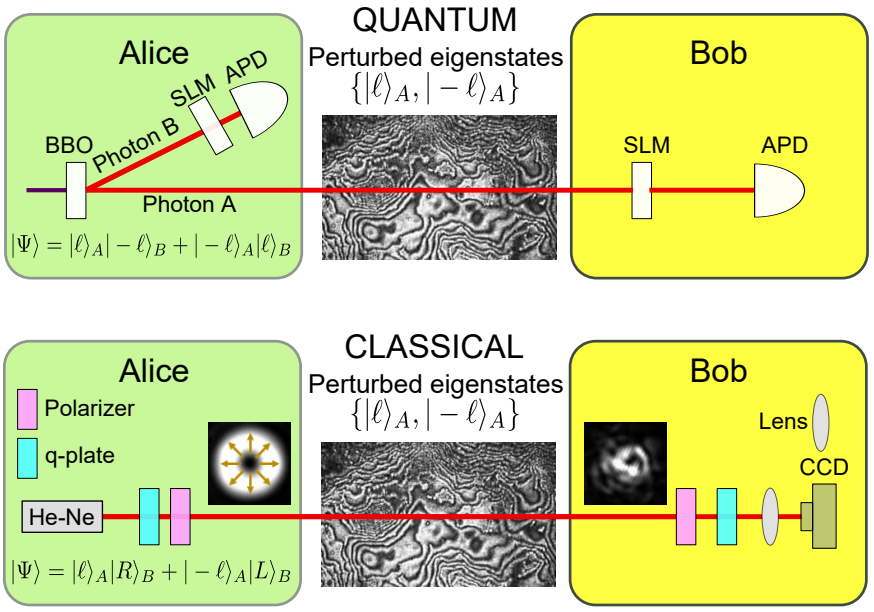


FIGURE 3.1: Illustration of the concept. (a) Alice generates two entangled photons using a SPDC process, and sends one photon (Photon A) to Bob through a free-space turbulent channel, which affects the quantum correlations due to perturbations to photon A. (b) Equivalently, Alice sends information to Bob using a classically entangled bright light field (laser beam). The spatial DoF (DoF A) is affected by the channel, while the polarisation (DoF B) is not. APD = avalanche photodiode, BBO = Beta Barium Borate (non-linear optical crystal), SLM = spatial light modulator and CCD = charge coupled device.

3.2 Channel tomography with classically entangled light

Our hybrid encoding space, described by the higher-order Poincaré sphere [38], is formed from the tensor product of the infinite dimensional OAM and the two-dimensional polarisation Hilbert spaces. We are interested in states of the form

$$|\Psi_\ell\rangle_{\text{in}} = \alpha\,|\ell\rangle_A\,|-\ell\rangle_B + \beta\,|-\ell\rangle_A\,|\ell\rangle_B\ , \tag{3.1a}$$

$$|\Psi_\ell\rangle_{\text{in}} = \alpha\,|\ell\rangle_A\,|R\rangle_B + \beta\,|-\ell\rangle_A\,|L\rangle_B\ , \tag{3.1b}$$

where $|\alpha|^2+|\beta|^2 = 1$. Equation 3.1a defines a two-photon entanglement system expressed in the OAM basis, $\{|-\ell\rangle, |\ell\rangle\}$, with each photon carrying ℓ quanta $\hbar$ of OAM [140]. Equation 3.1b defines a vector vortex mode, which here will be the classical equivalent to the system defined in Eq. 3.1a. The basis states $\{|L\rangle, |R\rangle\}$ correspond the left and right circular polarisation states, respectively.

We choose the concurrence as our measure of entanglement, as it has been shown to be effective in quantifying the degree of quantum and classical entanglement [136, 141].

For qubit pairs defined as in Eqs. 3.1a and 3.1b, the concurrence is given by:

$$\mathcal{C}(|\Psi_\ell\rangle_{\text{in}}) = 2|\alpha\beta| \ . \tag{3.2}$$

We consider an OAM state passing through turbulence which causes modal dispersion and thus broadens the OAM spectrum. Here, for each instance of the stochastically varying turbulence, the state evolution is a different unitary transformation that maps pure states onto pure states and takes the form:

$$|\ell\rangle \to \sum_{\ell'} p_{\ell-\ell'} \left|\ell'\right\rangle, \tag{3.3}$$

where $p_{\ell-\ell'}$ are the modal weightings. Thus, a given input vector vortex mode $|\Psi_\ell\rangle_{\text{in}}$ propagating through a turbulent channel will be transformed as follows:

$$\begin{aligned} |\Psi_\ell\rangle_{\text{in}} &\to \alpha \sum_{\ell'} p_{\ell-\ell'} \left|\ell'\right\rangle |R\rangle + \beta \sum_{\ell'} p_{-\ell-\ell'} \left|\ell'\right\rangle |L\rangle \\ = \alpha p_0 \,|\ell\rangle\,|R\rangle + \alpha p_{2\ell}\,|-\ell\rangle\,|R\rangle + \beta p_{-2\ell}\,|\ell\rangle\,|L\rangle + \beta p_0\,|-\ell\rangle\,|L\rangle + \sum(\ldots) \ . \end{aligned} \tag{3.4}$$

Note that we omit the subscripts A and B for simplicity of notation. Filtering for OAM values $-\ell$ and ℓ yields the un-normalised final state

$$|\Psi_\ell\rangle_{\text{out}} = \alpha p_0\,|\ell\rangle\,|R\rangle + \beta p_{-2\ell}\,|\ell\rangle\,|L\rangle + \alpha p_{2\ell}\,|-\ell\rangle\,|R\rangle + \beta p_0\,|-\ell\rangle\,|L\rangle. \tag{3.5}$$

Since in this state the polarisation serves as record of the original OAM value, (R, L) for $(\ell, -\ell)$, we can now read off the operator M that describes the action $|\Psi_\ell\rangle_{\text{in}} \to |\Psi_\ell\rangle_{\text{out}} = \text{M} \otimes \mathbb{I}\,|\Psi_\ell\rangle_{\text{in}}$ of the channel on the OAM DoF:

$$\text{M} = p_0\,|\ell\rangle\,\langle\ell| + p_{-2\ell}\,|\ell\rangle\,\langle-\ell| + p_{2\ell}\,|-\ell\rangle\,\langle\ell| + p_0\,|-\ell\rangle\,\langle-\ell| \, . \tag{3.6}$$

The one-to-one correspondence between the state (Eq. 3.5) of the vector beam and the Kraus operator (Eq. 3.6) for the OAM channel established here for classical light fields, is a manifestation of the Choi-Jamiolkowski isomorphism known to also connect the quantum OAM channel (same operator M) and the state of the qubit pair obtained from equation 3.1a. It follows that the matrix elements of the quantum channel operator, M, typically determined by process tomography requiring many measurements on single photons, can now be monitored by a state tomography of the classical output state $|\Psi_\ell\rangle_{\text{out}}$ in real time (single measurement of many photons).

3.3 Decay of classical entanglement in turbulence.

The entanglement of the final state (Eq. 3.5) is given by the concurrence $\mathcal{C}(|\Psi_\ell\rangle_{\text{out}}) = 2|\alpha\beta||p_0^2 - p_{2\ell}p_{-2\ell}|/p$, which, can be expressed in terms of the entanglement of the input state by

$$\mathcal{C}(|\Psi_\ell\rangle_{\text{out}}) = \mathcal{C}_{\text{ch}}\ \mathcal{C}(|\Psi_\ell\rangle_{\text{in}})\ , \tag{3.7}$$

where $0 \leq \mathcal{C}_{\text{ch}} = |p_0^2 - p_{2\ell}p_{-2\ell}|/p \leq 1$ equals the fraction of entanglement preserved by the channel and is given by the output concurrence obtained from an initially maximally entangled state with probability $p = (2|p_0|^2 + |p_{2\ell}|^2 + |p_{-2\ell}|^2)/2$. For example, in relatively strong turbulence, where $|p_{2\ell}p_{-2\ell}| \approx |p_0^2|$, the concurrence $\mathcal{C}(|\Psi_\ell\rangle_{\text{out}})$ vanishes, and with it all entanglement. The relation in Eq. 3.7 has been derived in [142] for entangled pairs of two-level systems. Note that for the channel under present investigation, the decay of the concurrence can be modelled as a function of the turbulence strength according to the following relation [143]

$$\mathcal{C}(|\Psi_\ell\rangle_{\text{out}}) = \frac{\text{SR}}{\text{SR}^2 - \text{SR} + 1}\ , \tag{3.8}$$

where SR is a measure of the turbulence strength known as the Strehl ratio.

The broadening of the OAM spectrum described by Eq. 3.4 leads to inter-modal coupling among vector modes, resulting in a loss of entanglement with increasingly strong perturbations. Within the subspace of vector modes with $|\ell| = 1$, this coupling can be analysed using the Bell basis [144], known as optical fibre modes in waveguide theory:

$$|\text{TM}\rangle_1 = \frac{1}{\sqrt{2}}(|1\rangle|R\rangle + |{-1}\rangle|L\rangle)\ , \tag{3.9}$$

$$|\text{TE}\rangle_1 = \frac{1}{\sqrt{2}}(|1\rangle|R\rangle - |{-1}\rangle|L\rangle)\ , \tag{3.10}$$

$$|\text{HE}^{\text{e}}\rangle_1 = \frac{1}{\sqrt{2}}(|1\rangle|L\rangle + |{-1}\rangle|R\rangle)\ , \tag{3.11}$$

$$|\text{HE}^{\text{o}}\rangle_1 = \frac{1}{\sqrt{2}}(|1\rangle|L\rangle - |{-1}\rangle|R\rangle)\ . \tag{3.12}$$

By way of example, consider a $|\text{TM}\rangle_1$ propagating in a strong turbulence regime. In the special case where $p_0 = p_{2\ell} = p_{-2\ell}$ (strong coupling), the final state reduces to

$$|\Psi_1\rangle_{\text{out}} = \frac{1}{\sqrt{2}}p_0\left[|1\rangle|R\rangle + |{-1}\rangle|L\rangle + |1\rangle|L\rangle + |{-1}\rangle|R\rangle\right], \tag{3.13}$$

$$= \frac{1}{\sqrt{2}}p_0\left[|\text{TM}\rangle_1 + |\text{HE}^{\text{e}}\rangle_1\right]\ , \tag{3.14}$$

$$= \frac{1}{\sqrt{2}}p_0\left(|1\rangle + |{-1}\rangle\right) \otimes \left(|R\rangle + |L\rangle\right)\ , \tag{3.15}$$

which is separable (not entangled) i.e., the spatial and polarisation DoFs can be factorised. Equivalently in the quantum case, perturbations incurred by one of the two photons (modal dispersion and projection onto a subspace) will transform an initial entangled state into a final factorisable (separable) state.

3.4 Experimental realisation

3.4.1 Classical and quantum setup

Here we demonstrate experimentally the equivalence between the evolution of classical and quantum entanglement in turbulence. Our classical experimental setup is illustrated in Fig. 3.2 and comprises creation, propagation and detection stages. In the creation step, the vector vortex mode is prepared either directly from a "spiral laser" [41], or by using wave plates and q-plates [62] to transform a linearly polarised Gaussian beam into a vector vortex mode. We passed our vector mode through a turbulent channel (turbulence phase screen) that was made to vary with time, and analysed the output beam with two detection systems: a vector mode sorter to uniquely detect each of the maximally entangled modes, thus evaluating the amount of inter-modal coupling, and a tomography detector [136]. Our two figures of merit here are the concurrence and fidelity:

- In general, the concurrence of an arbitrary qubit state (pure or mixed) can be computed from its density matrix ρ [141]

$$\mathcal{C}(\rho) = \max\{0, \sqrt{\lambda_1} - \sqrt{\lambda_2} - \sqrt{\lambda_3} - \sqrt{\lambda_4}\}, \tag{3.16}$$

  where λ_i are the eigenvalues in decreasing order of the Hermitian matrix $R = \rho(\sigma_2 \otimes \sigma_2)\rho^*(\sigma_2 \otimes \sigma_2)$, and σ_2 is the Pauli matrix $\sigma_2 = \left[\begin{smallmatrix} 0 & -i \\ i & 0 \end{smallmatrix}\right]$.

- The fidelity is a measure of the degree of similitude between an arbitrary state with density matrix ρ, and a target state with density matrix ρ_t. It is defined as

$$F(\rho, \rho_t) = \left[\mathrm{Tr}\left\{\sqrt{\sqrt{\rho_t}\rho\sqrt{\rho_t}}\right\}\right]^2. \tag{3.17}$$

The quantum experiment was performed as presented in Fig. 2.5 in Chapter 2. A 3 mm BBO crystal was pumped with a picosecond laser with wavelength of 355 nm and an average power of 350 mW to produce non-collinear, degenerate entangled photon pairs with type I phase matching via SPDC. Each photon was directed onto a SLM where the conjugate of the modes to be measured and the turbulence was encoded.

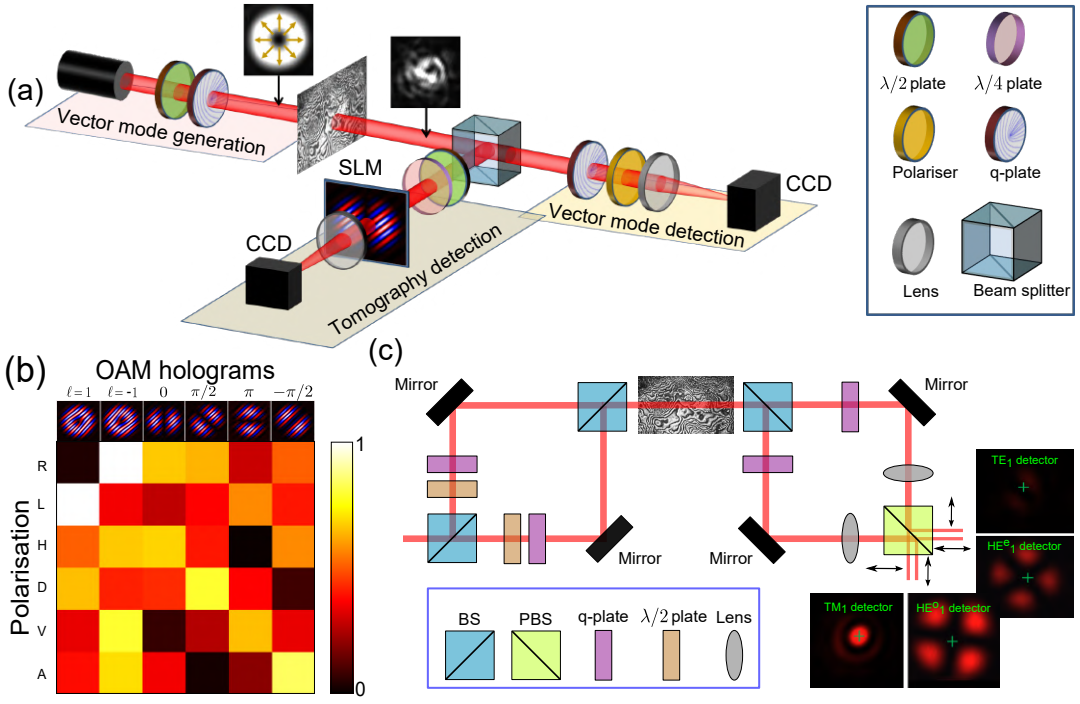


FIGURE 3.2: Experimental setup. (a) The entangled qubits were encoded using a q-plate and propagated through the turbulent conditions simulated with single Kolmogorov phase screens. The output state was analysed using a vector mode sorter that performs a decomposition into vector states. (b) Full state tomography of the perturbed state was performed by projecting polarisation states, selected with the quarter or half-wave plate, onto OAM states encoded on a spatial light modulator. The output of the projections were observed in the far-field using a camera. (c) Vector vortex modes are (de)multiplexed using two Mach-Zehnder interferometers, with the q-plates used to (de)encode hybrid qubits.

The modulated beams were then coupled into single mode fibres (SMF), which extract the Gaussian profile from the beams. Avalanche photodiodes were used to register the presence of photon pairs from the SMFs via a coincidence counter. A state tomography of the two photons was performed to determine the evolution of the concurrence as a function of the turbulence strength. To simulate one photon going through turbulence, we superimpose turbulence holograms on one of the SLMs used to analyse one of the photons in the entangled pair.

3.4.2 Modelling atmospheric turbulence

We modelled turbulence based on Kolmogorov's theory. We used the Strehl ratio (SR) as our measure of the turbulence strength, and is defined as follows:

$$\mathrm{SR} = \frac{1}{1 + 6.88(\omega_0/r_0)^2}, \tag{3.18}$$

where ω_0 is the beam size, r_0 is Fried's parameter, expressed in terms of the refractive index structure C_n^2, wavelength λ and propagation distance z as

$$r_0 = 0.185 \left(\frac{\lambda^2}{C_n^2 z} \right)^{3/5}. \tag{3.19}$$

The above expression in Eq. 3.18 was obtained by applying the quadratic structure function approximation [145] to the general definition of SR presented in [146]. To generate the turbulence phase screen, we multiply the Kolmogorov power spectral density with a random complex function, then inverse Fourier transform the product following the method detailed in [147].

3.5 Entanglement decay in turbulence

In Fig 3.3(a) we show the measured dependence of the concurrence of our quantum and classical states as a function of the degree of turbulence in the channel, together with the theoretical prediction from Eq. 3.8. We used a $|\mathrm{TM}\rangle_1$ vector mode and an $|\ell| = 1$ maximally entangled OAM state as our equivalent classical and quantum systems, respectively. The experimental results for both the classical and quantum cases are in excellent agreement with the theory. Hence, the agreement between the classical and quantum experiments validates the equivalence of the quantum and classical models depicted in Fig. 3.1. The inset in Fig 3.3(a) shows the variation in the measured fidelity of a $|\mathrm{TM}\rangle_1$ vector mode in turbulence, computed with respect to a maximally entangled state. Furthermore, by varying the concurrence of the input vector mode in Fig 3.3(b), we experimentally confirmed for the first time for spatial modes, the decay law of entanglement [142] as summarised for pure states in equation 3.7, i.e., that there is a linear relationship between $\mathcal{C}(|\Psi_\ell\rangle_{\mathrm{out}})$ and $\mathcal{C}(|\Psi_\ell\rangle_{\mathrm{in}})$. This provides physical meaning for the notion of entanglement at the classical level; that is, beyond the mathematical non-separability of the DoFs, nature does not distinguish between classical and quantum entanglement in one-sided channels.

The observed decay of entanglement with increasing turbulence, as predicted by Eq. 3.8, is explained by examining the effects of turbulence on the mode spectrum: for example, in the classical case, with increasing turbulence strength, the scattering among vector vortex modes is increased, as seen in Figs 3.4(a)-(e). This is due to the spreading of the OAM spectrum, as shown in Figs 3.4(f)-(g), which leads to crosstalk among vector vortex modes, as described by Eq. 3.5, and similarly for the quantum case.

Having characterised the impact of the channel on the states to be propagated, we used the setup to show a proof-of-principle data transmission over the channel. It has been

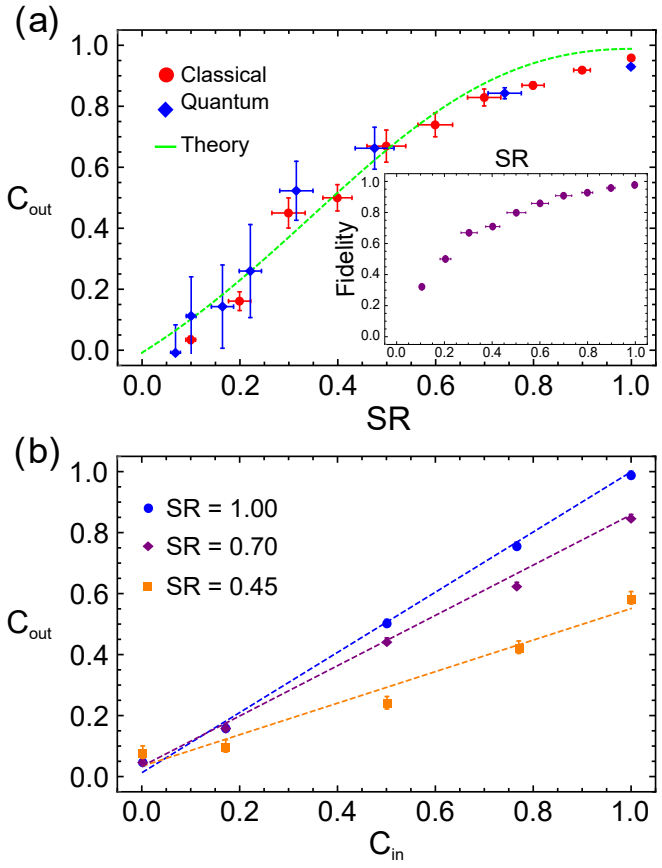


FIGURE 3.3: Evolution of classical entanglement in turbulence. (a) The measured concurrence variation after propagation through turbulence screens of various SR strengths (increasing from high to low SR values) for the classical (red markers) and quantum (blue markers) states, correctly follow the theoretical prediction for one of two entangled photons going through a turbulent channel (green dashed line). The fluctuations in SR arise from the statistical averaging of the turbulence screen for an encoded SR value. The inset shows the decay in fidelity of the output state with respect to a maximally entangled state, as a function of the turbulence strength. (b) The measured concurrence obeys the predicted linear mapping to the concurrence of the input state. Here we have shown this for three channels with SR = 1.00, 0.70 and 0.45. The error bars represent the standard errors in the averages over the multiple turbulence realisations.

recently shown that the non-separability of vector vortex beams can be used to encode two bits of information simultaneously on the entangled DoFs [144]. In our scheme, we (de)multiplexed the four maximally entangled vector modes as shown in Fig 3.2(c). This allowed us to perform a four-bit encoding scheme based on these states. The encoded image Fig 3.5(a) was transmitted through one particular instance of a turbulence channel with turbulence strength SR = 0.3. Without any correction, the received image shows significant amounts of distortion, resulting in a 64.2% correlation coefficient with respect to the encoded image [Fig 3.5(c)]. This is due to the intermodal coupling corrupting the encoded bits sequences, and resulting in state errors measured at the receiver's end. A practical advantage of studying the decoherence induced by a channel is the ability to mitigate perturbations through pre- or post-processing of the data. After propagation

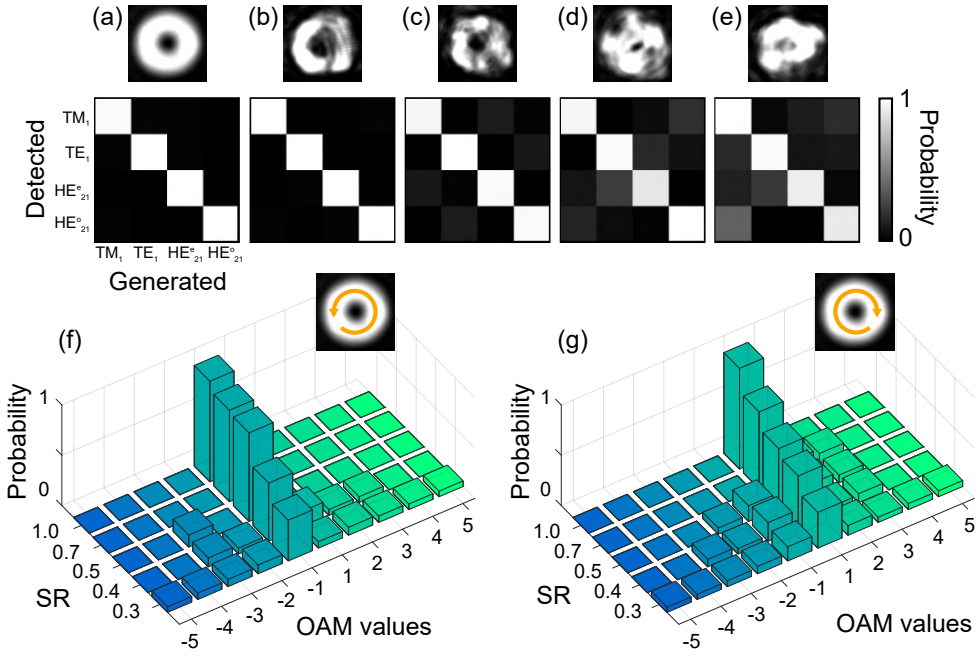


FIGURE 3.4: Evolution of the mode spectrum in turbulence. (a)-(e) Show vector mode dispersion for the four vector vortex modes of the $|\ell| = 1$ subspace for average SR values of 1.0, 0.7, 0.5, 0.4 and 0.3 respectively. The matrices show the evolution of the power distribution among the four vector detector for a given input mode. (f) and (g) Show the effect of the turbulence on the spatial DoF, measured by modal decomposition of the $|-1\rangle|L\rangle$ and $|1\rangle|R\rangle$ input qubit states, respectively. The scattering of the OAM eigenstates is observed through a redistribution of energy between OAM modes with increasing SR.

through a perturbing medium, the input and output states can be related by

$$|\Psi_\ell\rangle_{\text{out}} = \mathrm{M} \otimes \mathbb{I}\,|\Psi_\ell\rangle_{\text{in}}, \tag{3.20}$$

where M is the channel operator of the system that contains all the information about the crosstalk induced by the medium. The complete tomography data to determine the matrix $\mathrm{M} \otimes \mathbb{I}$ is graphically represented in Fig 3.5(b). Thus the perturbation can be cancelled by correcting the final state, $|\Psi_\ell\rangle_{\text{out}}$, with $\mathrm{M}^{-1} \otimes \mathbb{I}$ when processing the measurement data, or by physically implementing a conjugate filter (details of this filtering will be provided in the next Chapter). Using this correction technique, we obtained an image with an increased correlation coefficient of 98.9%, as shown in Fig 3.5(d).

3.6 Conclusion

The characterisation of quantum channels is a *sine qua non* to the implementation of practical quantum communication protocols. Using vector vortex modes, so-called

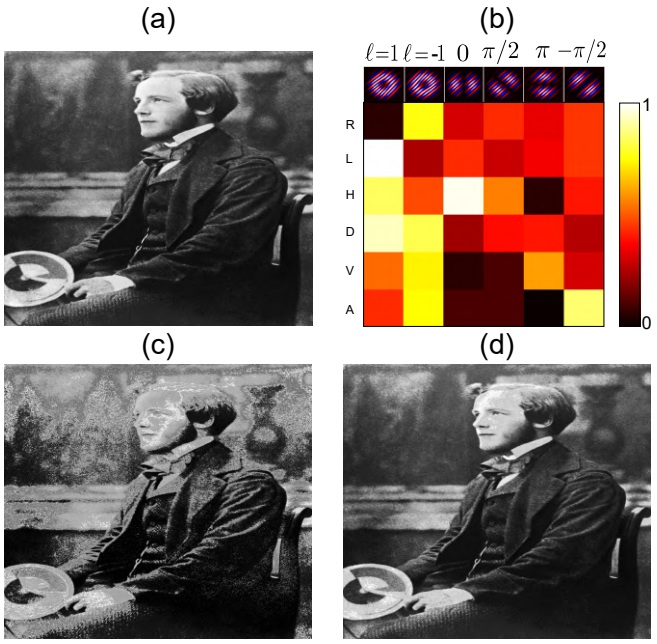


FIGURE 3.5: Experimental results for data transmission over turbulent channel. (a) Using a four-bit encoding technique with four multiplexed vector modes, a 425×513 pixels image of Maxwell was transmitted through a turbulent channel with SR = 0.3, and demultiplexed at the receiver's end. A threshold at 15% of the maximum received signal was applied to the data to filter noise signals. By characterising the channel with a full tomography of the classically entangled light, we obtained (b). (c) The channel perturbation resulted in a distorted image at the receiver's end with a correlation coefficient of 64.2%. (d) Correcting the image with the inverse channel matrix increased the correlation coefficient to 98.9%.

classically entangled light, and a pair of entangled photons we demonstrated that the evolution of two entangled DoFs, one of which is affected by atmospheric turbulence, is the same for classical and quantum light. We have shown this for OAM in atmospheric turbulence, but the approach can easily be generalised to other spatial modes and perturbations.

The decay of classical entanglement we observed demonstrates that vector vortex modes are not resilient to atmospheric turbulence. This is further supported by the measured decay in fidelity between the final and the original state, as shown in the inset of Fig 3.3(a). Both results are not in contradiction with the possibility to recover qubits encoded in two rotationally symmetric vector states [148] that was tested against the influence of turbulence [149]. This method uses a filter (post-selection) to eliminate all spatial crosstalk components generated by weak turbulence, resulting in the loss of photons. However, it does not provide a measure of resilience to turbulence as all modes can be recovered using this technique.

In the quantum realm, a channel tomography requires multiple measurements to be performed on an ensemble of systems, in our case on photons consecutively passing the

stochastic channel over an extended period of time – this is what here gives rise to mixed states despite the unitary evolution of each single photon. In fact, the unitary evolution of a single photon cannot be detected directly, just as the state of a single photon cannot. However, for classical light, these restrictions do not exist, allowing a channel tomography and error correction in real-time, implemented in quantum links. The resulting ability to detect the specific realisations of stochastic perturbations classically, enables an unravelling of the otherwise mixed quantum state dynamics in terms of pure states and to reinstall the original state of the photon.

We point out that this approach differs from the standard classical communications correction tools where multiple orthogonal modes are sent sequentially through the channel to infer the cross-talk matrix. Rather, our approach allows a single maximally entangled state to be sent, followed by a complete tomography measurement, in order to infer the evolution of the quantum state in real-time.

Chapter 4

Mitigating information loss in quantum key distribution with entangled photons through turbulence

This Chapter contains extracts from a publication by **Bienvenu Ndagano** and Andrew Forbes: "Characterization and mitigation of information loss in a six-state quantum-key-distribution protocol with spatial modes of light through turbulence". *Physical Review A*, 98:062330, 2018.

Here we study how turbulence affects the secret key rate of a six-state quantum key distribution protocol with OAM modes as the basis. We show theoretically and numerically that when appropriately scaling the size of higher OAM modes, those with higher OAM separation are more resilient to turbulence, enabling a more robust link. As a comparison, we simulated the decay of fidelity in turbulence in the context of the six-state QKD protocol, using OAM modes with $\ell = 2$, 4, 6, 8, 10 and 20. Next, we revisit the fact that turbulence results in the spread of information into multiple subspaces through modal scattering. During measurement, only a fraction of the total information content is recovered because only pre-agreed subspaces are probed by the receiver, resulting in a lower channel capacity. We show that more information can be recovered by increasing the space of post-selected modes. We parametrise the expression of the detection fidelity in the different subspaces as a function of OAM and turbulence strength, and derive an expression for the limit to which the recovery is possible. Finally, we outline a scheme whereby errors due to turbulence can be mitigated by probing the channel

with a classical beam. Using a process tomography to obtain the channel matrix using a bright classically entangled light source. The resultant conjugate channel operator is then used to implement in real-time a Procrustean filter on the quantum state, resulting in a concentration of entanglement and a higher secure key rate in the quantum transmission.

4.1 Quantum key distribution with entangled photons

The appeal of QKD lies in the ability to securely exchange information between two parties in the presence of external perturbations, solely by exploiting the laws of physics. These perturbations reduce the ability of the receiver, Bob, to correctly measure the states encoded by the sender, Alice. Some common sources of perturbations include measurements from an eavesdropper, dark counts in the detectors, or noise that is present in the quantum channel (atmospheric turbulence for example). The extent to which these perturbations affect Bob's measurements determine the secure key rate of the QKD link.

We considered a scenario where Alice generates a pair of entangled photons through spontaneous parametric down-conversion, retains one photon (Photon A) of each pair and sends the other (Photon B) to Bob through a turbulent channel, as shown in

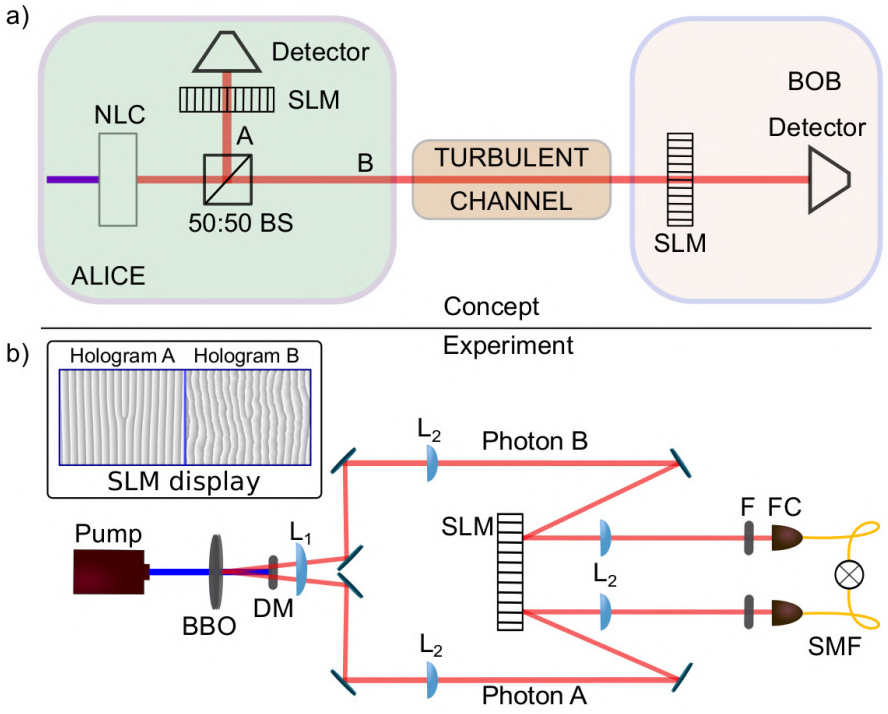


FIGURE 4.1: (a) Alice generates a pair of entangled photons (A and B) using a pumped non-linear crystal (NLC) and sends one of the photons to Bob through a turbulent channel. Alice and Bob enact a quantum key distribution protocol, whereby they perform joint measurements on the photon pair using spatial light modulators (SLMs) in order to build the key. (b) Shows the experimental realisation where one SLM is used to encode the spatial projections of both Alice and Bob. Turbulence is encoded as a phase screen, superimposed on the tomography holograms as shown on the inset. The plane of the BBO crystal was relayed onto the SLM and then the fibers using 4f imaging systems. F = 10 nm bandpass filters; L1 = 10 mm; L2 = 750 mm; FC = fiber coupler with 2 mm focal length lens integrated; SMF = single mode fiber; DM = dichroic mirror.

Fig. 4.1(a). In order to generate the secret key, Alice and Bob enact an entanglement-based variant of the 1984 Bennett & Brassard protocol (BB84) [150]. For every photon pair, Alice and Bob perform joint projective measurements onto states from a set of mutually unbiased bases (MUBs). While BB84 with qubits states is traditionally performed with two MUBs (four states in total), the six-state protocol uses three MUBs, a total of six states, hence the name. On one hand, the six-state protocol carries higher inherent losses compared to the original BB84, given that in the former, 2/3 of the photons are lost during sifting as opposed to 1/2 in the latter. On the other hand, using more MUBs enhances the tolerance to noise with a higher error rate threshold [151]. At the end of the transmission, Alice and Bob broadcast the measurement bases for each of the N generated pairs. Upon comparison, Alice and Bob discard measurement outcomes where the encoding and decoding bases disagree to distil a key that is further refined through error correction and privacy amplification [152].

The secret key rate, R, is the amount of information that can be securely exchanged between Alice and Bob in the presence of perturbations. The exact expression of R depends on the QKD protocol used. In the six-state protocol it is given by [153]

$$R = 1 + \frac{3}{2}Q\log_2\left(\frac{Q}{2}\right) + \left(1 - \frac{3}{2}Q\right)\log_2\left(1 - \frac{3}{2}Q\right) \tag{4.1}$$

where $Q = 1-F$ is the qubit error rate and F is the measurement fidelity, i.e., the ability of Bob to correctly distinguish the states sent by Alice. The secret key rate reaches its maximum $R_{\max} = 1$ for $Q = 0$ or $F = 1$. The QKD link between Alice and Bob is viable so long as the secret key rate is positive; this is satisfied for $Q < 0.126$ or $F > 0.874$. By comparison, the secret key rate in the original BB84 protocol is given by [153]

$$R = 1 + 2Q\log_2(Q) + 2(1 - Q)\log_2(1 - Q), \tag{4.2}$$

and admits a lower error threshold of $Q < 0.11$ and a higher fidelity threshold $F > 0.89$. We use the six-state protocol to demonstrate the importance of mode order and size, information retrieval and entanglement concentration schemes, with OAM as the spatial mode of choice. Although we use OAM as a topical example, the framework provided here can easily be extended to other spatial modes.

4.2 Turbulence-induced decay of QKD fidelity

4.2.1 Theoretical model

In the scenario depicted in Fig. 4.1(a), the entangled photons are initially correlated in OAM. Ideally Alice and Bob would like to share the following maximally entangled two-photon state

$$\left|\Phi^{+}\right\rangle_{AB} = \frac{1}{\sqrt{2}}\left(\left|\ell_1\right\rangle_A\left|\ell_2\right\rangle_B + \left|-\ell_1\right\rangle_A\left|-\ell_2\right\rangle_B\right). \tag{4.3}$$

In the presence of turbulence, the correlations between the two photons are weakened, resulting in a lower photon detection probability [154–156] and loss of entanglement and measurement fidelity with respect to the initial state [143, 147, 157]. This is because the OAM spectrum of photon B is altered as it propagates through the turbulent channel. From previous work it was found that the spectral broadening arising from turbulence perturbations is peaked around the initially transmitted state [154, 156–161]. Thus for simplicity we model the effect of turbulence as follows

$$\left|\ell\right\rangle \xrightarrow{\text{turbulence}} \sum_m b^{|\ell-m|}\left|m\right\rangle, \tag{4.4}$$

where $0 \leq b < 1$. The spectral broadening is symmetric about the initially transmitted OAM state $|\ell\rangle$. The two-photon state in Eq. 4.3 is then modified due to the turbulent channel acting on photon B, to produce

$$\begin{aligned}\left|\Phi\right\rangle_{AB} = \frac{1}{\sqrt{N}}\Big(&\sum_m b^{|\ell_2-m|}\left|\ell_1\right\rangle_A\left|m\right\rangle_B \\ &+ \sum_n b^{|-\ell_2-n|}\left|-\ell_1\right\rangle_A\left|n\right\rangle_B\Big),\end{aligned} \tag{4.5}$$

where

$$N = \sum_m b^{2|\ell_2-m|} + \sum_n b^{2|-\ell_2-n|} = 2\sum_m b^{2|\ell_2-m|}. \tag{4.6}$$

In the absence of turbulence, $b \to 0$ and the distribution is sharply peaked around the initial OAM state. Conversely, in very strong turbulence, the OAM spectrum flattens and $b \to 1^{-}$ (the negative superscript is used here to refer to b approaching 1 from the left).

To determine the effect of turbulence on the secure key rate of the QKD protocol, we chose to focus on the decay of measurement fidelity as a function of the turbulence strength; that is, the probability that, after turbulence, Alice and Bob measure their photons in the correlated state described in Eq. 4.3. Given that the target state is a

pure state, the fidelity takes the form [128]

$$F = \langle\Phi^+|\,\rho\,|\Phi^+\rangle = |\langle\Phi^+|\Phi\rangle|^2 = \frac{1}{\sum_m b^{2|\ell_2-m|}}. \tag{4.7}$$

In the two-dimensional case where Alice and Bob use states $|\pm\ell_1\rangle$ and $|\pm\ell_2\rangle$, respectively, the measurement fidelity within the post-selected subspaces is given by

$$F_\ell = \frac{1}{\sum_{m=\pm\ell_2} b^{2|\ell_2-m|}} = \frac{1}{1+b^{4|\ell_2|}}. \tag{4.8}$$

Note that the measurement fidelity is dependent on the turbulence strength: F_ℓ decreases as b increases. However, the fidelity is bounded below by $F_\ell = 0.5$. This is logical when one considers the overlap in Eq. 4.7. In the specific case where $|\langle\Phi^+|\Phi\rangle|^2 = 1/2$, the states $|\Phi\rangle$ and $|\Phi^+\rangle$ can be said to belong to mutually unbiased bases. Hence, no information can be extracted from the projection of $|\Phi\rangle$ onto $|\Phi^+\rangle$, and the mutual information between Alice and Bob, I_{AB}, vanishes.

4.2.2 Experimental realisation

The decay in fidelity is experimentally demonstrated in Fig. 4.2. Information is encoded into OAM modes with a transverse electric field expressed as [16]

$$U_\ell(r,\phi) = \sqrt{\frac{1}{\pi|\ell|!}}\frac{1}{\omega_0}\left(\frac{r\sqrt{2}}{\omega_0}\right)^{|\ell|}\exp\left(-\frac{r^2}{\omega_0^2}\right)\exp(i\ell\phi). \tag{4.9}$$

For ease of notation, we will refer to the OAM state in Eq. 4.9 with the ket $|\ell\rangle$. The projections performed by Alice and Bob in the six-states protocol are made into the following bases: $\{|-\ell\rangle,\ |\ell\rangle\}$, $\{(|\ell\rangle+|-\ell\rangle)/\sqrt{2},\ (|\ell\rangle-|-\ell\rangle)/\sqrt{2}\}$ and $\{(|\ell\rangle+i\,|-\ell\rangle)/\sqrt{2},\ (|\ell\rangle-i\,|-\ell\rangle)/\sqrt{2}\}$. Interestingly, the joint measurements in the six-state protocol coincide with those required for an over-complete quantum state tomography [128, 162], and are shown in Fig. 4.2(a). Projections in the same basis fully discriminate the states prepared by Alice, while measurements in conjugate bases produce a uniform probability distribution. These projective measurements can be used to reconstruct the density matrix of the state after the turbulence and compute the fidelity. Note that the region enclosed with red-dashed lines highlights a set of measurements that would be required in BB84.

We generated entangled photons through type-I spontaneous parametric down-conversion by pumping a 3 mm BBO crystal with a picosecond laser with wavelength 355 nm and average power 350 mW, as shown in Fig. 4.1(b). For each down-converted pump photon, a pair of entangled photons is emitted, each with a wavelength of 710 nm that were then

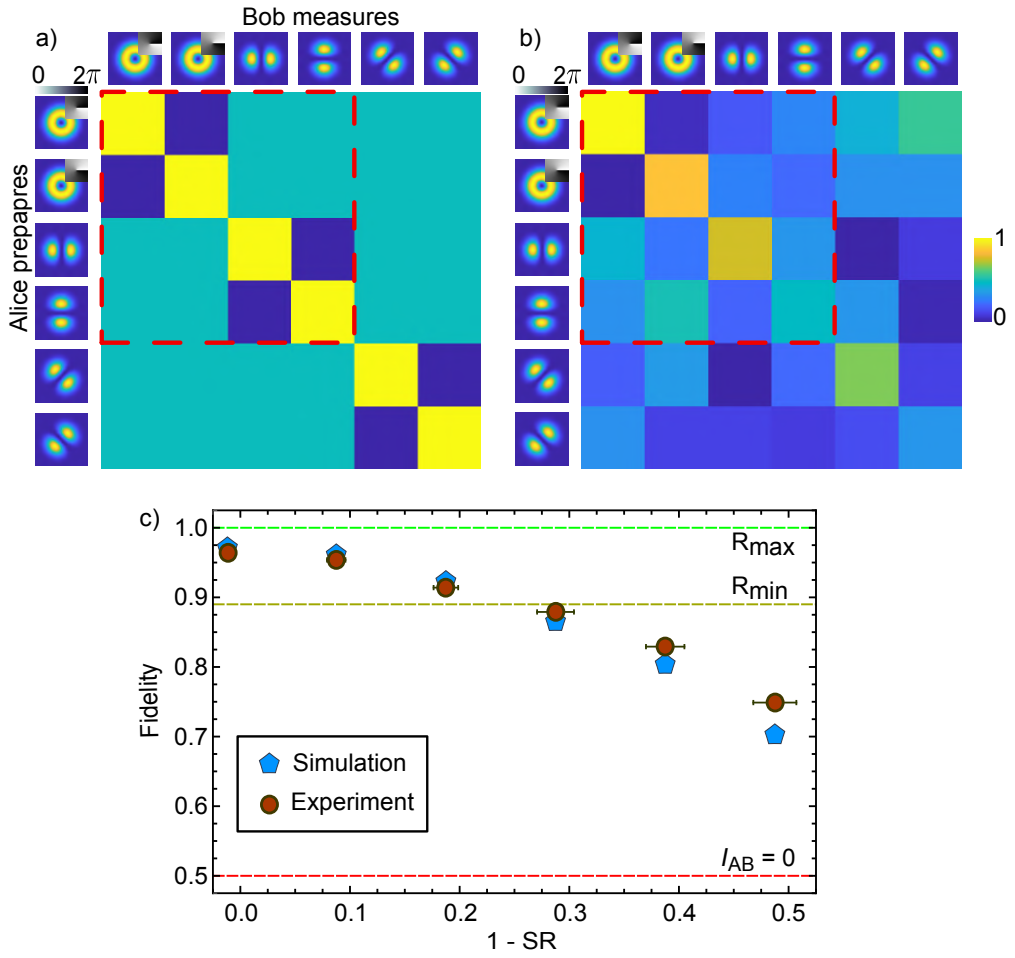


FIGURE 4.2: Fidelity decay in turbulence. Alice and Bob perform joint measurements on the two-photon state for an entanglement based six-state protocol with OAM states carrying $\hbar$ of OAM per photon. These tomographic measurements are shown (a) in the absence of turbulence (SR = 1) and (b) in the presence of turbulence with SR = 0.5 for a mode size $\omega_0 = 800$ μm. The regions enclosed by the red dashed lines (top left corner) show the measurements required for the traditional BB84. (c) Shows both the simulated and experimental measurements of the decay of fidelity as a function of turbulence for OAM states with $|\ell| = 1$ and post-selected beam width $\omega_0 = 200$ μm.

directed onto a spatial light modulators (SLM). On one half of the SLM, we encoded the spatial projections required for the six-state protocol. On the other half, the same projections were superimposed with turbulence phase screens to simulate one photon propagating through turbulence. The substitution of a turbulent channel by a single phase screen is justified by the fact that we have assumed a weak scintillation regime, i.e., phase-only perturbations. The down-converted photons were then passed through 10 nm bandpass filters and coupled into single-mode fibers connected to single-photon detectors (Excelitas SPCM-AQRH-13-FC) with dark count rates of 250 counts per second and a 70% photon detection efficiency. Using holograms encoded on the SLM, we performed a state tomography of the two-photon state as a function of turbulence.

We modelled turbulence based on Kolmogorov's theory. We used the Strehl ratio (SR) as our measure of the turbulence strength

$$\mathrm{SR} = \frac{1}{1 + 6.88(\omega_0/r_0)^2}, \tag{4.10}$$

where ω_0 is the beam size and r_0 is Fried's parameter, expressed in terms of the refractive index structure C_n^2, wavelength λ and propagation distance z as

$$r_0 = 0.185 \left(\frac{\lambda^2}{C_n^2 z}\right)^{3/5}. \tag{4.11}$$

The above expression in Eq. 4.10 was obtained by applying the quadratic structure function approximation [145] to the general definition of SR presented in [146]. To generate the turbulence phase screen, we multiply the Kolmogorov power spectral density with a random complex function, then inverse Fourier transform the product following the method detailed in [147]. The effects of turbulence on the projective measurements are, by means of example, graphically depicted in Fig. 4.2(b) for a single turbulence phase screen with strength SR = 0.5. Note that here the Strehl ratio is defined with respect to the Gaussian mode and only serves to define controlled turbulence conditions.

We chose to perform the experiment using two OAM states with $\ell = \pm 1$, as well as the corresponding MUBs. The fidelity measurement results, averaged over a total of 50 single turbulence phase screens per turbulence strength SR, are presented in Fig. 4.2(c). The uncertainty in the turbulence strength arises from the prior calibration measurements we performed to ensure the accuracy of the turbulence strength that was digitally encoded.

4.3 Effect of mode separation on the QKD fidelity

As predicted by Eq. 4.8, the measured fidelity decays with increasing turbulence strength. Interestingly, the fidelity in Eq. 4.8 is also seen to depend on the OAM used to encode the qubit information. For a given turbulence strength, states with higher helicity, ℓ, have higher fidelities, allowing for more robust quantum communication due to higher tolerance to noise. To illustrate the advantage of using higher values of OAM for robust QKD, we simulated the measurements that Alice and Bob would perform to build a key in the six-state protocol, using OAM modes with different topological charges.

The intensities of the OAM modes used are shown in Fig. 4.3 for $\ell = \{2, 4, 6, 8, 10, 20\}$. Each point on the graph corresponds to the fidelity of Bob's measurements at a given turbulence strength, averaged over 200 turbulence screens. Observe that the decay in fidelity is faster when using OAM states with lower OAM values, compared to those

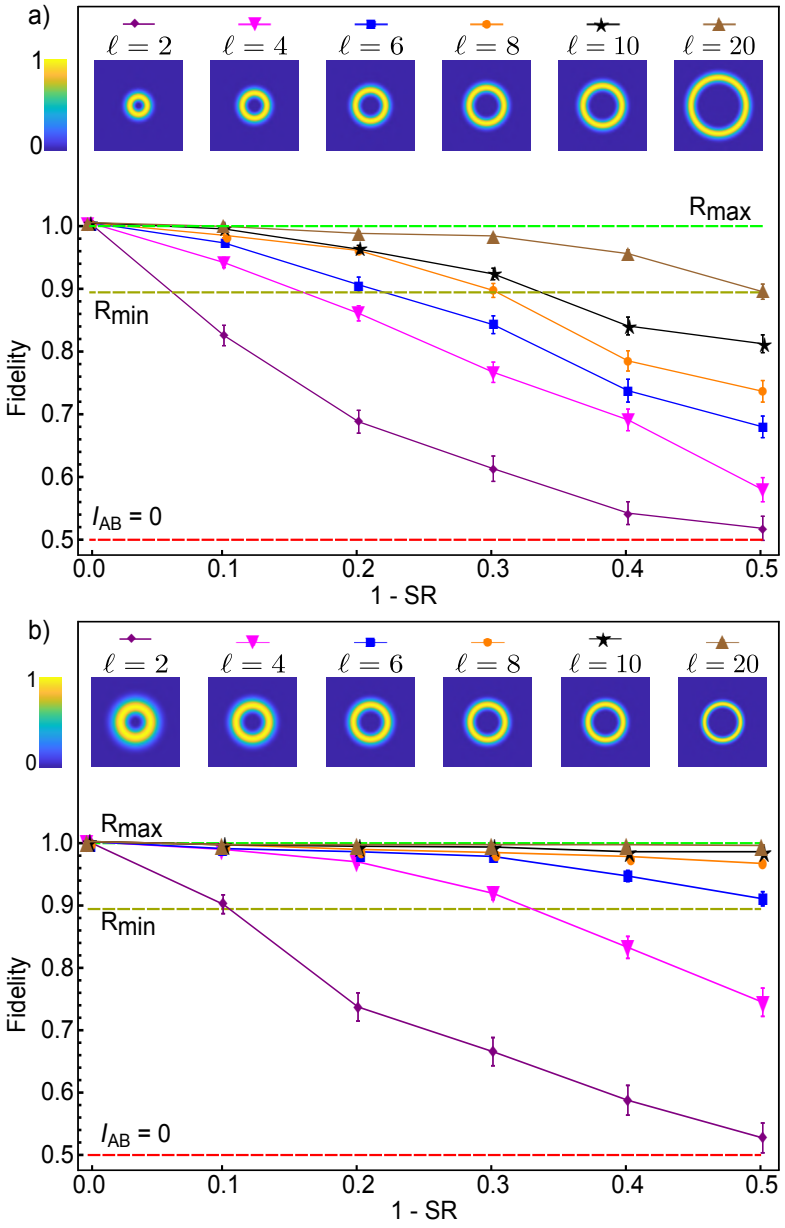


FIGURE 4.3: a) Simulated measurement of fidelity decay as a function of turbulence for OAM states with $\ell = 2$, 4, 6, 8, 10 and 20. The minimum secure key rate $R_{\min} = 0$ is attained for a fidelity of 0.89, while the mutual information I_{AB} vanishes for $F = 0.5$. b) Simulated measurement of fidelity decay as a function of turbulence for OAM states with $\ell = 2$, 4, 6, 8, 10 and 20 with the modes all renormalised to the same size.

with larger OAM values. This is indeed consistent with the expected behaviour of the fidelity deduced in Eq. 4.8. Note that the minimum fidelity for which the channel is still secure, that is $R > 0$, is chosen here to be $F = 0.89$. This is because for $F > 0.89$ the channel is viable for both the BB84 and the six-state protocol. The mutual information I_{AB} between Alice and Bob, given by

$$I_{AB} = 1 + Q\log_2(Q) + (1-Q)\log_2(1-Q), \tag{4.12}$$

vanishes for $Q = F = 0.5$.

It could be argued that the comparison between these modes is not a fair one due to the difference in mode size. Indeed, the size of an OAM mode depends on the OAM value according to the relation $\omega_\ell = \omega_0\sqrt{|\ell| + 1}$ [163]. The higher the OAM content, the larger the mode size. However, note that the strength of turbulence SR in Eq. 4.10 is inversely proportional to the square of the the mode size; given fixed turbulence conditions (that is we fix r_0), larger beams would experience higher turbulence compared to smaller beams, and hence will experience higher OAM scattering. The results shown in Fig. 4.3 thus show that despite experiencing higher turbulence, higher OAM modes still show more robustness compared to lower OAM modes due to their higher mode separation. To remove the dependence on beam size, we ran a second simulation where we normalised each OAM mode to the same size; that is, rather than encoding the same scale parameter ω_0 for all the modes, we assign each mode the OAM-dependent scale parameter $\omega_\ell = \omega_0/\sqrt{|\ell| + 1}$. This way, all OAM modes have identical beam size ω_0. The newly normalised states, together with the results of the simulation are shown in Fig. 4.3(b). Observe that the rescaled modes now have a smaller radius. Hence they would experience less turbulence that in the cases presented in Fig. 4.3(a). Indeed, reducing the beam size has increased the robustness to turbulence as shown in Fig. 4.3. Similarly to the previous simulation, modes with higher OAM content are even more resilient to turbulence.

Though QKD with higher order modes is desirable due to the reduced crosstalk, there are some design challenges that need to be considered. In the case of photon pairs produced by parametric down-conversion, as is the case here, the OAM correlation signal decays with increasing OAM index. This reduces the speed at which secure keys can be generated. A possible avenue that has been explored involves shaping the down-converted spectrum at the source. By changing the spatial profile of the pump laser, one is able to change the nature and amplitude of the spatial (OAM) correlations [164, 165]. In this manner, one could engineer the OAM spectrum so that higher order modes have higher correlation signals compared to the lower order modes.

4.4 Mitigating information loss

4.4.1 Recovery of information in additional subspaces

Atmospheric turbulence causes modal scattering, resulting in the broadening of the mode spectrum, transforming the maximally entangled qubit state in Eq. 4.3 into a high dimensional entangled state as described in Eq. 4.4. However, when implementing

the BB84 or six-state protocol, Alice and Bob post-select on a given OAM subspace, say $|\ell|$. The consequence of this post-selection is the loss of information and therefore the decay of entanglement. Could Bob extend the post-selected mode space to gain more information? Consider the scenario depicted in Fig. 4.4, where a quantum router that separates even and odd OAM modes [166] is placed after the turbulent channel but before Bob's detector. In this scenario, Alice projects her photon in the $|\ell| = 1$ subspace, while Bob makes his projections in both the $|\ell| = 1$ and $|\ell| = 2$ subspaces. Let $|\Phi\rangle_{ABo}$ and $|\Phi\rangle_{ABe}$ be the two-photon state shared by Alice and Bob at the detectors for odd and even $|\ell|$ respectively, as depicted in Fig. 4.4. Then

$$|\Phi\rangle_{ABo} = \frac{1}{\sqrt{\mathcal{N}_1}}(|1\rangle|1\rangle + |-1\rangle|-1\rangle) + \frac{b^2}{\sqrt{\mathcal{N}_1}}(|1\rangle|-1\rangle + |-1\rangle|1\rangle), \tag{4.13}$$

$$|\Phi\rangle_{ABe} = \frac{b}{\sqrt{\mathcal{N}_2}}(|1\rangle|2\rangle + |-1\rangle|-2\rangle) + \frac{b^3}{\sqrt{\mathcal{N}_2}}(|1\rangle|-2\rangle + |-1\rangle|2\rangle), \tag{4.14}$$

where $\mathcal{N}_1 = 2(1 + b^4)$ and $\mathcal{N}_2 = 2b^2(1 + b^4)$ are normalisation constants.

One can compute the fidelity between Alice and Bob within the respective subspaces and show that they are given by Eq. 4.8. Thus, for b sufficiently small (enough to guarantee that the secret key rate is positive) Bob can extract useful information by probing additional subspaces. However here the measurement in the higher OAM subspace will only occur at a rate proportional to b^2. The effect of turbulence on the photon detection probability is shown in Fig. 4.4(c). As a quantitative illustration, the probabilities were normalised with respect to the two measuring subspaces. Losses resulting from turbulence in the primary channel $|\pm1\rangle_A \otimes |\pm1\rangle_B$ are accompanied by gains in the other channel $|\pm1\rangle_A \otimes |\pm2\rangle_B$, up to a limit defined by the turbulence parameter b. In the range of acceptable values for b ($F > 0.874$), post-selecting on the additional OAM subspace allows a fraction of the decohered information to be recovered. We highlight that while we have normalised the detection probability to only the measured subspaces; that is, we have assumed that scattering is limited to those two subspaces, one should expect a lower fraction of photons recovered when accounting for the full high-dimensional space after scattering. In the above, photon loss during sifting is not accounted for (1/2 in BB84 and 2/3 for the six-state protocol). Nevertheless, post-selecting on additional subspaces would allow Bob to extract more information from the QKD link, at a rate inversely proportional to the turbulence strength.

We also considered the possibility that the quantum router in Fig. 4.4 could have been introduced by an eavesdropper to extract the photons with $|\ell| = 2$ that would have

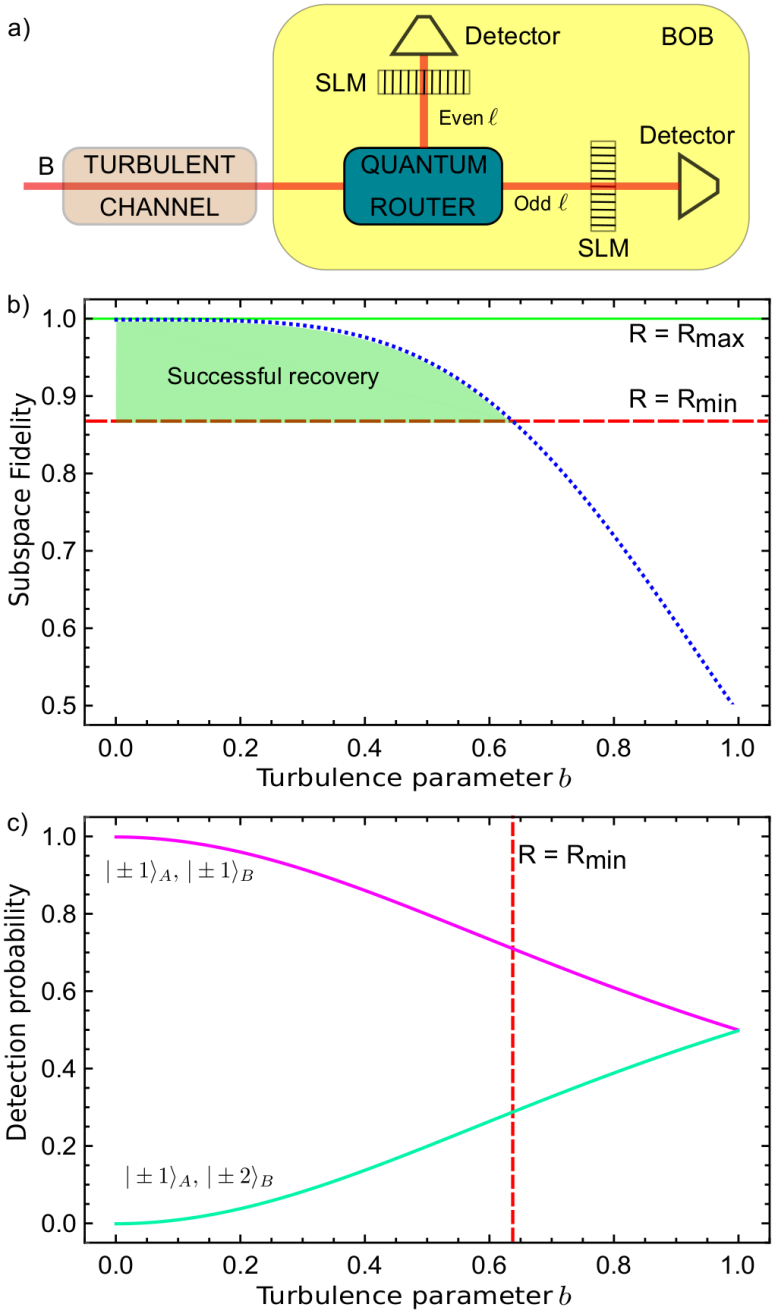


FIGURE 4.4: Recovering information in higher OAM subspaces. (a) To increase photon recovery during QKD, Bob uses a quantum router to separate photon states according to their parity, and post-selects two OAM subspaces: $|\ell| = 1$ and $|\ell| = 2$. (b) Shows the measurement fidelity of Alice and Bob, normalised to each of the two subspaces (dotted blue line). The range of turbulence parameter b for which information recovery is still possible is shown as the green shaded region enclosed by the R_{max}, R_{min} and the fidelity curve. (c) Shows the impact of turbulence on the relative photon detection probability in two measuring subspaces for Alice and Bob.

otherwise been discarded by Bob through post-selection. The eavesdropper, Eve, could for example attempt an intercept-and-resend strategy. This approach would however not be successful because of sifting losses: Eve would send photons to Bob with at least

a 50% error in BB84, and over 66% in the six-state protocol. Hence, probing additional subspaces would only benefit Bob and not the eavesdropper.

4.4.2 Conversion of noise to losses

The intermodal scattering incurred by an OAM state in the presence of turbulence can be represented as

$$|\Phi\rangle_{AB} = \mathbb{I} \otimes \hat{M} \left|\Phi^+\right\rangle_{AB}, \tag{4.15}$$

where $\hat{M}$ is an operator acting on Bob's qubit. In the context of QKD, it is not possible to obtain an exact picture of $\hat{M}$ by quantum state tomography given that multiple projections cannot be performed on a single photon. However, it has recently been shown that in a one-sided channel, the decay of entanglement of a quantum state is identical to the decay of non-separability in a classical vector beam [157]. As such, one could employ a non-separable classical beam, sometimes called classically entangled, to reconstruct the channel operator. Because of the abundance of photons in the classical beam, the necessary projections for the quantum state tomography can be realised simultaneously with high signal-to-noise ratio. This would allow for real-time measurement of the channel, and mitigation of errors on the quantum states measured. Importantly, this approach can be implemented optically as we outline next.

For a given realisation of turbulence, i.e., a single phase screen in this case, the channel operator $\hat{M}$ admits the following polar decomposition:

$$\hat{M} = \hat{U}|\hat{M}| = \hat{U}\left(\lambda_0|0\rangle\langle 0| + \lambda_1|1\rangle\langle 1|\right), \tag{4.16}$$

where $\hat{U}$ is a unitary operator and λ_i are the eigenvalues of the positive operator $|\hat{M}|$, with corresponding eigenstates $|i\rangle$. Note that if Alice and Bob encode information as shown in the previous sections, then the eigenstates $|i\rangle$ would correspond to superposition of the basis OAM states.

Given that $\lambda_i \leq 1$, implementing an inverse transformation is in general not always physically feasible; this is because the eigenvalues of $|\hat{M}|^{-1}$, $1/\lambda_i$, are larger than 1. Thus, implementing the inverse channel transformation would imply adding identical copies of the photons to the system, something that is prohibited by the no-cloning theorem [167]. Alternatively, one can engineer a conjugate filter $\tilde{M}$, given by

$$\tilde{M} = |\tilde{M}|\hat{U}^\dagger = \left(\lambda_1|0\rangle\langle 0| + \lambda_0|1\rangle\langle 1|\right)\hat{U}^\dagger, \tag{4.17}$$

such that $\tilde{M}\hat{M} = \lambda_0\lambda_1\mathbb{I}$. Alice and Bob can then distil the initial state $\left|\Phi^+\right\rangle_{AB}$ at a rate proportional to $\lambda_0\lambda_1$, thus increasing the measurement fidelity of the QKD link.

Interestingly, the state measured after applying the conjugate filter will have higher fidelity with respect to the initial state and, in our case, a higher degree of entanglement. This concentration of entanglement by means of local operations was first proposed in [168], where a set of maximally entangled singlet states could be filtered from an ensemble of non-maximally entangled states. This process was later extended to mixed states [169] and experimentally demonstrated in two and higher dimensions [106, 170–172]. In all these demonstrations, the entanglement concentration was achieved through Procrustean filtering, performed on both photons from an entangled pair. However, unlike the previous demonstrations, the method we present here achieves entanglement distillation with local operations performed on only one of the entangled parties.

Let us demonstrate the scheme using a particular example from our simulation. Alice prepares the entangled state $|\Phi^+\rangle_{AB}$ and sends one qubit to Bob through a turbulent channel. Simultaneously, Alice sends a vector beam $|\Psi\rangle$ through the same channel, as shown in Fig. 4.5(a). The initial quantum and classical states are expressed as follows

$$\left|\Phi^+\right\rangle_{AB} = \frac{1}{\sqrt{2}}\left(|\ell\rangle_A|\ell\rangle_B + |-\ell\rangle_A|-\ell\rangle_B\right) \tag{4.18}$$

$$|\Psi\rangle = \frac{1}{\sqrt{2}}\left(|\ell\rangle|R\rangle + |-\ell\rangle|L\rangle\right), \tag{4.19}$$

where $|R\rangle$ and $|L\rangle$ are right- and left-circular polarisation states.

In the presence of turbulence, the classical beam is transformed by a unitary phase screen, causing intermodal scattering. We assume that Alice and Bob post-select a particular OAM subspace for both the classical and quantum state. As a result of post-selection, Bob receives the following classical state

$$\begin{aligned}|\Psi_{\text{out}}\rangle = 0.53|\ell\rangle|R\rangle + 0.18e^{i\pi/3}|-\ell\rangle|R\rangle \\ + 0.24e^{i\pi/5}|\ell\rangle|L\rangle + 0.47e^{-i\pi/8}|-\ell\rangle|L\rangle.\end{aligned} \tag{4.20}$$

Note that the probabilities do not add to unity since we are projecting onto a particular OAM subspace. While the state could easily be normalised, we have purposely not done so to demonstrate the effect of post-selection. The channel operator then reads

$$\mathrm{M} = \begin{pmatrix} 0.47e^{-i\pi/8} & 0.18e^{i\pi/3} \\ 0.24e^{i\pi/5} & 0.53 \end{pmatrix}. \tag{4.21}$$

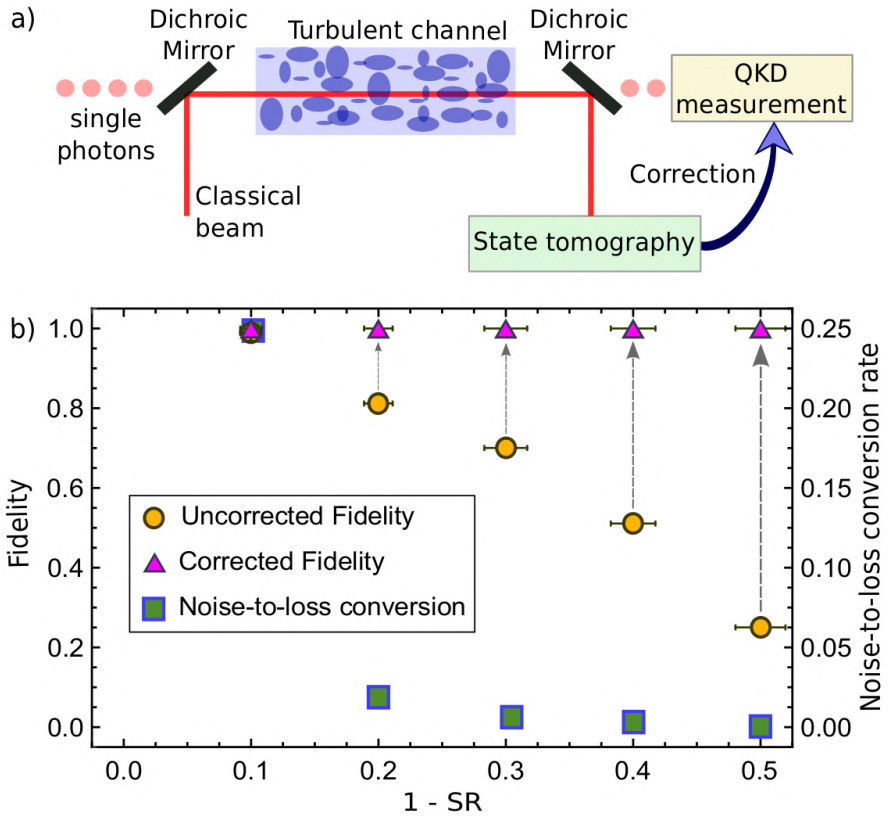


FIGURE 4.5: Noise to loss conversion scheme with classical light. (a) Single photons, together with a bright classical beam are sent through the same channel and analyzed separately. A state tomography of the classical beam is performed to reconstruct the channel operator. The classical data are subsequently used to perform a Procrustean filtering on the quantum state in real-time. (b) The detection fidelity is computed from the measured two-photon density matrix in the presence of turbulence (uncorrected data). The channel matrix is reconstructed using a bright classical source and used to engineer a filter that cancels out the effect of turbulence, increasing the fidelity to unit (corrected).

We denote V and D the matrix of eigenvectors and eigenvalues, respectively, of the operator $\mathrm{M}^{\dagger}\mathrm{M}$. The positive operator $|M|$, is computed as follows

$$|\mathrm{M}| = V\sqrt{D}V^{-1} = \begin{pmatrix} 0.5167 & 0.1069 + 0.0085i \\ 0.1069 - 0.0085i & 0.5494 \end{pmatrix}.$$

One can then show that the positive operator $|\mathrm{M}|$ admits the following spectral decomposition:

$$|\mathrm{M}| = 0.4246|0\rangle\langle 0| + 0.6415|1\rangle\langle 1|,$$

where

$$|0\rangle = \begin{pmatrix} 0.7584 \\ -0.6497 + 0.0519i \end{pmatrix}; \; |1\rangle = \begin{pmatrix} 0.6497 + 0.0519i \\ 0.7584 \end{pmatrix}.$$

Note that the above eigenvectors are represented in the OAM basis where $|-\ell\rangle = (1\ 0)^T$ and $|\ell\rangle = (0\ 1)^T$.

The unitary matrix U is given by

$$U = \mathrm{M}|\mathrm{M}|^{-1} = \begin{pmatrix} 0.8356 - 0.4211i & -0.0053 + 0.3527i \\ 0.1836 + 0.3012i & 0.9337 - 0.0615i \end{pmatrix}, \tag{4.22}$$

such that $U^\dagger U = \mathbb{I}$.

One can then read off the expression of the positive conjugate filter to apply in the correction

$$|\tilde{\mathrm{M}}| = 0.6415|0\rangle\langle 0| + 0.4246|1\rangle\langle 1|, \tag{4.23}$$

and show that $\tilde{\mathrm{M}}\mathrm{M} = (0.6415 \times 0.4246)\ \mathbb{I}$. The result of the correction in this case is a conversion of noise from crosstalk, into loss: the identity operator obtained by applying the conjugate filter shows that the effect of turbulence can be completely removed from the final quantum state, resulting in entanglement distillation. The corresponding constant term quantifies the photon losses during the filtering process. A simulation of the noise-to-loss conversion on the fidelity is shown in Fig. 4.5(b) for single phase screen at various turbulence strengths. The observed increase in fidelity post-filtering comes at the cost of reduced key generation rate, shown in Fig. 4.5(b).

4.5 Conclusion

Spatial modes have shown promising potential to realise high-bandwidth quantum communication beyond the qubit. In free-space, spatial modes are adversely affected by external perturbations during propagation, as a result of turbulence. Here we have considered a six-state protocol with OAM, showed the deleterious effects of turbulence on the secret key rate, and proposed two approaches to mitigate errors and losses. Unlike in previous studies, we have carefully accounted for mode-dependent size when comparing the decay in detection fidelity between OAM states. To mitigate the effects of turbulence, we have proposed two novel schemes. On one hand, we have shown that depending on the strength of turbulence, more information can be recovered by post-selecting a state space larger than the encoding one. However, the frequency of a viable detection in the additional subspaces increases with turbulence strength, a behaviour not desired given that detection fidelity decreases with increasing turbulence strength. On the other hand, we have introduced an entanglement concentration scheme based on a classical measurement of the channel. We exploited the fact that entanglement

dynamics of quantum and classically entangled states in a one-sided channel are indistinguishable to show that the classical beam can be used to probe the channel in real-time. Reconstruction of the channel matrix in real-time can be performed through a process tomography and used to perform Procrustean filtering on one party in the entangled pair shared by Alice and Bob. It is our opinion that the tools presented here will be useful in supplementing existing methods of turbulence mitigation for robust quantum (and classical) communication.

Chapter 5

Entanglement concentration by Hong-Ou-Mandel interference

This Chapter contains extracts from a publication by **Bienvenu Ndagano** and Andrew Forbes: "Entanglement distillation by Hong-Ou-Mandel interference with orbital angular momentum states". Applied Physics Letters: Photonics, **4**:016103, 2019.

In previous Chapters, we have demonstrated that spatial entanglement is susceptible to decay in the presence of external perturbations such as atmospheric turbulence. In Chapter 4, we have introduced methods to mitigate information loss, one of which involved Procrustean filtering, a common method to realise entanglement distillation [168]. In this Chapter, we address the issue of entanglement distillation on an ensemble of OAM entangled photons generated by spontaneous parametric down-conversion (SPDC), and perturbed by a one-sided weak turbulent channel. One of the photons in the entangled pair propagates through the turbulence, leading to a unitary scattering in a higher dimensional OAM space. As a result of post-selection on a particular OAM subspace, one measures a decay of the degree of entanglement despite the unitary nature of the channel operator. To distil entanglement, we interfere the non-maximally entangled photons in a Hong-Ou-Mandel (HOM) configuration [173, 174]. It has been shown that the HOM interference can be exploited to implement a filter for Bell states according to their intrinsic symmetry [175, 176]. By performing a state tomography of the quantum states after implementing the HOM filter, we obtained distilled entangled singlet states with fidelity $F \geq 0.90$, up from as low as $F = 0.03$.

5.1 The concept

Consider the OAM entangled two-photon state $|\Psi_\ell\rangle$ expressed as follows:

$$\left|\Psi_\ell^-\right\rangle = \frac{1}{\sqrt{2}}\left(|\ell\rangle_A\,|-\ell\rangle_B - |-\ell\rangle_A\,|\ell\rangle_B\right), \tag{5.1}$$

where the subscripts A and B label each of the photons in the entangled pair carrying $\ell\hbar$ quanta of OAM. Photon A is allowed to propagate through a turbulent channel that is unitary, causing a scattering of OAM states:

$$|\ell\rangle \xrightarrow{\text{turbulence}} \sum_{\ell'} c_{\ell-\ell'}\,|\ell'\rangle, \tag{5.2}$$

where $\sum_{\ell'}|c_{\ell'-\ell}|^2 = 1$. While the scattering certainly leads to the formation of higher-dimensional correlations, we will restrict the problem to a qubit subspace by projecting on the initial OAM state space; that is, we will consider the terms $\ell' = \pm\ell$ in Eq. 5.2. The perturbed qubit state after turbulence then becomes

$$|\Psi_\ell\rangle = \frac{1}{\sqrt{2}}\Big(c_0\,|\ell\rangle_A\,|-\ell\rangle_B - c_0\,|-\ell\rangle_A\,|\ell\rangle_B + c_{2\ell}\,|-\ell\rangle_A\,|-\ell\rangle_B - c_{-2\ell}\,|\ell\rangle_A\,|\ell\rangle_B\Big). \tag{5.3}$$

It is useful at this point to express $|\Psi_\ell\rangle$ in the Bell basis. This can be done by realising that the last two terms in Eq. 5.3 correspond to a state on a two-photon OAM Bloch sphere [27], where the poles are the Bell states $\left|\Phi_\ell^+\right\rangle$ and $\left|\Phi_\ell^-\right\rangle$, expressed as followed:

$$\left|\Phi_\ell^\pm\right\rangle = \frac{1}{\sqrt{2}}\left(|-\ell\rangle_A\,|-\ell\rangle_B \pm |\ell\rangle_A\,|\ell\rangle_B\right). \tag{5.4}$$

One then rewrites Eq. 5.3 in the Bell basis as follows:

$$|\Psi_\ell\rangle = c_0\left|\Psi_\ell^-\right\rangle + c_{2\ell}^+\left|\Phi_\ell^+\right\rangle + c_{2\ell}^-\left|\Phi_\ell^-\right\rangle, \tag{5.5}$$

where $c_{2\ell}^\pm = \left\langle\Phi_\ell^\pm|\Psi_\ell\right\rangle$.

After the turbulent channel, the photons enter a Hong-Ou-Mandel filter as show in Fig. 5.1(a). The aim of this filter is to distil the singlet state $\left|\Psi_\ell^-\right\rangle$ from the perturbed state $|\Psi_\ell\rangle$. The layout of the filter is shown as inset in Fig. 5.1(a), and consists of two mirrors and a 50:50 beam-splitter (BS). A general entangled state $|\Psi\rangle = \left(|\ell_1\rangle_A\,|-\ell_2\rangle_B \pm |-\ell_1\rangle_A\,|\ell_2\rangle_B\right)/\sqrt{2}$ is transformed by the HOM filter as follows

$$\begin{aligned}|\Psi\rangle \xrightarrow{\text{HOM filter}} &\frac{1}{2\sqrt{2}}\Big(i\,|\ell_1\rangle^1\,|-\ell_2\rangle^1 + i\,|\ell_1\rangle^2\,|-\ell_2\rangle^2 + |\ell_1\rangle^1\,|-\ell_2\rangle^2 + |\ell_1\rangle^2\,|-\ell_2\rangle^1\Big)\pm\\ &\frac{1}{2\sqrt{2}}\Big(i\,|-\ell_1\rangle^1\,|\ell_2\rangle^1 + i\,|-\ell_1\rangle^2\,|\ell_2\rangle^2 + |-\ell_1\rangle^1\,|\ell_2\rangle^2 + |-\ell_1\rangle^2\,|\ell_2\rangle^1\Big).\end{aligned} \tag{5.6}$$

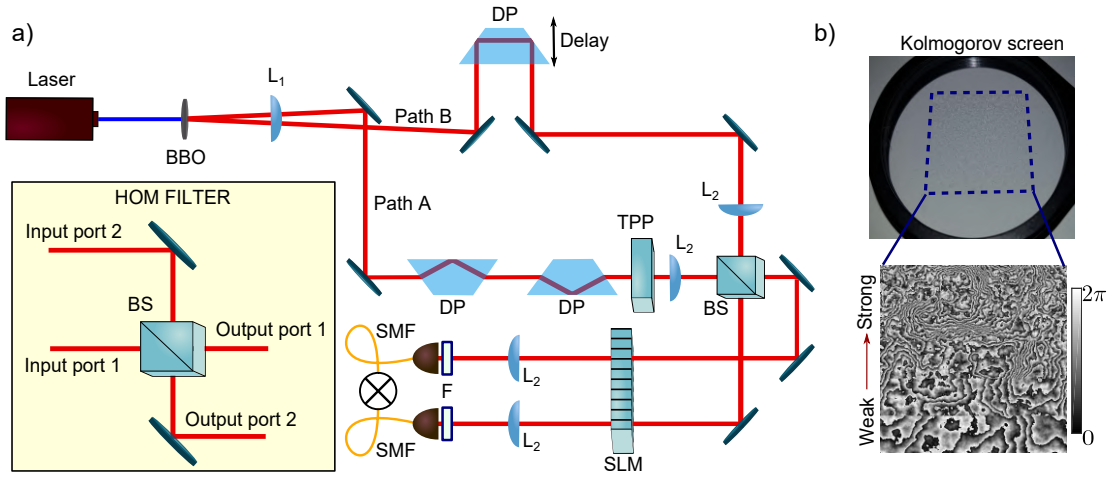


FIGURE 5.1: Experimental setup for entanglement distillation. By pumping a 3 mm thick, non-linear type-I BBO crystal with a 355 nm laser, we produced through SPDC, pairs of entangled photons with wavelength 710 nm. The photons are sent down two paths, one containing a delay line and another with two dove prisms (DP) to manipulate the SPDC state symmetry. A turbulence phase plate (TPP) in path A perturbs the state before the photon paths are recombined at a 50:50 beam-splitter (BS). Lenses L_1 ($f_1 = 100$ mm) and L_2 ($f_2 = 750$ mm) relay the plane of the BBO crystal onto the spatial light modulator (SLM). The two photons are probed using digital holograms encoded on the SLM, passed through 10 nm bandpass filters (F), and then coupled to single mode fibres (SMF). (b) Shows the range of phase fluctuations across the turbulence phase plate.

where the superscripts 1 and 2 label the output ports of the beam-splitter. One can then show that the filter transforms the states in Eq. 5.5 as follows

$$\left|\Psi_\ell^-\right\rangle \xrightarrow{\text{HOM filter}} \left|\Psi_\ell^-\right\rangle^{1,2}, \tag{5.7}$$

$$\left|\Phi_\ell^\pm\right\rangle \xrightarrow{\text{HOM filter}} \frac{i}{2}\left(\left|\Phi_\ell^\pm\right\rangle^{1,1} + \left|\Phi_\ell^\pm\right\rangle^{2,2}\right). \tag{5.8}$$

Note that the antisymmetric singlet state $\left|\Psi_\ell^-\right\rangle$ exhibit anti-bunching; no two photons are in the same output port. For the two symmetric states, however, photons bunch and exit in the same port of the beam-splitter. Therefore, conditioning the photon detection on coincidence between the two output ports automatically discards the contribution of symmetric states in Eq. 5.5, leading to the following distillation result:

$$\left|\Psi_\ell\right\rangle \xrightarrow{\text{HOM filter}} c_0 \left|\Psi_\ell^-\right\rangle^{1,2}. \tag{5.9}$$

In this manner, noise arising from turbulence is converted to losses, with the probability $|c_0|^2$ representing the fraction of singlets distilled. Given that only antisymmetric states exhibit anti-bunching after the HOM filter, the choice of initial singlet state is logical and necessary; that is because all symmetric states produce no coincidence signal after the HOM filter [177]. One can then conclude that the HOM filter projects onto singlet states.

Note that the above treatment would also be valid in the case of two photons going through two turbulence screens. This is because given a weak turbulence operator $\hat{M}_i$ acting on photon i we have, within a given OAM subspace,

$$\hat{M}_A \otimes \hat{M}_B \left|\Psi_\ell^-\right\rangle \rightarrow \tilde{c_0} \left|\Psi_\ell^-\right\rangle + (\cdots)_{\text{symmetric}}. \tag{5.10}$$

However, one should expect the fraction of distilled states to be even lower than in the case of one photon going through turbulence, with $|c_0| \geq |\tilde{c_0}|$.

In the case of strong turbulence where scintillations are significant, the HOM filter would distil singlets (at an even lower rate) but the nature of the original state before turbulence would be unknown. That is because strong turbulence would allow symmetry-breaking scattering that compromises the uniqueness of the two-photon interference peak signal; both symmetric and antisymmetric could, in principle, cause a coincidence detection after perturbation. It is this many-to-one mapping makes it impossible to deduce the state before the turbulence.

5.2 Experimental realisation

5.2.1 Production of antisymmetric states

We experimentally demonstrated our distillation scheme using the setup in Fig. 5.1(a). Pairs of entangled photons were produced through SPDC. We pumped a 3-mm type-I BB0 crystal with a 355 nm laser at 350 mW average power and 80 MHz repetition rate, producing the symmetric SPDC state

$$|\Psi\rangle_{\text{SPDC}} = \alpha_0 \left|0\right\rangle_A \left|0\right\rangle_B + \sum_{\ell>0} \alpha_\ell \left|\Psi_\ell^+\right\rangle_{AB}, \tag{5.11}$$

where $\left|\Psi_\ell^+\right\rangle_{AB} = \left(\left|\ell\right\rangle_A \left|-\ell\right\rangle_B + \left|-\ell\right\rangle_A \left|\ell\right\rangle_B\right)/\sqrt{2}$. Using a pair of dove prisms in the path of photon A, we controlled the symmetry of OAM subspaces by inducing an OAM-dependent phase in the SPDC state: $\left|\ell\right\rangle \rightarrow \exp(2i\ell\theta)\left|\ell\right\rangle$, where θ is the angle between the two dove prisms:

$$\left|\Psi_\ell^+\right\rangle \xrightarrow{\text{DPs}} \frac{\exp(2i\ell\theta)\left|\ell\right\rangle\left|-\ell\right\rangle + \exp(-2i\ell\theta)\left|-\ell\right\rangle\left|\ell\right\rangle}{\sqrt{2}}. \tag{5.12}$$

For $\theta = (2n+1)\pi/4\ell$ with $n \in \mathbb{N}$, one achieves the conversion to antisymmetric state in all the OAM subspaces. We set $\theta = \pi/4$ and obtained, up to a global phase, the

following selection rules:

$$\left|\Psi_\ell^+\right\rangle \xrightarrow{\theta=\pi/4} \begin{cases} \left|\Psi_\ell^-\right\rangle \text{ for odd } \ell, \\ \left|\Psi_\ell^+\right\rangle \text{ for even } \ell. \end{cases} \tag{5.13}$$

Photon A then propagates through turbulence. We considered a turbulent channel with weak scintillation, such that atmospheric perturbations can be summed to a unitary transformation, i.e, a single turbulence phase screen [147], and thus does not lead to a decay in purity. In our case, the turbulence phase screen was modelled based on the Kolmogorov's theory and printed on a glass plate with different zones of average phase fluctuations, as shown in Fig. 5.1(b). In the path of photon B we placed a delay line, consisting of a dove prism mounted on a piezo-controlled stage, to adjust the delay in arrival time of the two photons at the BS in the HOM filter. Photons exiting the HOM filter were then analysed using spatial filters encoded on a spatial light modulator (SLM), coupled to single-mode fibres and measured in coincidence.

5.2.2 Calibration of the Hong-Ou-Mandel filter

Initially, we calibrated the HOM filter by scanning for the characteristic dip of coincidence counts in the HOM interference. The aim is to demonstrate the efficacy of the distillation scheme by performing a quantum state tomography at points of zero and maximum visibility of the HOM dip; at zero visibility, the HOM filter is in the "OFF" state (out of the HOM interference region) while at maximum visibility it is in the "ON" state (lowest point in the HOM interference region). Using the digital holograms encoded on the SLM, we post-selected the $\ell = 0$ subspace (symmetric state) from the SPDC state and show the quantum interference signal in Fig. 5.2(a), in the presence and absence of turbulence. The visibility, $\mathcal{V}$, was computed from the coincidence counts inside (C_{in}) and outside the dip (C_{out}):

$$\mathcal{V}_{\text{dip}} = \frac{C_{\text{out}} - C_{\text{in}}}{C_{\text{out}} + C_{\text{in}}}. \tag{5.14}$$

We obtained, respectively, a visibility of 84.4% and 75.7% for the dip without and with turbulence. The decay in visibility that we measured can be attributed to the decay in signal-to-noise ratio resulting from turbulence-induced intermodal scattering that reduces the coincidence rates. We will show further that this does affect the distillation of singlet Bell states.

We extended the measurement of the HOM interference trace to the $\ell = \pm 1$ subspace where the SPDC state has been made antisymmetric. This is done by projecting the

photon pair on conjugate OAM states and scanning the piezo-controlled stage. Due to anti-bunching effect after the HOM filter, one would expect a HOM peak rather than a dip. This is because events with two-photons in one output port of the BS are in theory non-existent when the filter is in the ON state. Indeed we measured, as shown in Fig. 5.2(b), HOM peaks without and with turbulence with visibilities of 73.7% and 60.4%, respectively. In this case, the calculation of visibility was done differently and we will argue the formula we used.

The standard formula in Eq. 5.14 is adequate for fringes with an ideal minimum of zero; under this condition, the visibility is equal to unity. This is indeed the case for the HOM dip. Due to the bunching effect with the HOM filter ON, symmetric states attain, in principle, a minimum of zero coincidence counts. Therefore the visibility of the dip can be computed as in Eq. 5.14. For antisymmetric states, coincidence counts should in theory, increase two-fold when the HOM filter in ON, with no zero minimum. Under Eq. 5.14, this would lead to negative visibility values with absolute maximum less than unity. Rather, we choose to express the visibility of the HOM peak as follows:

$$\mathcal{V}_{\text{peak}} = \frac{C_{\text{out}} - (2C_{\text{out}} - C_{\text{in}})}{C_{\text{out}} + (2C_{\text{out}} - C_{\text{in}})} = \frac{-C_{\text{out}} + C_{\text{in}}}{3C_{\text{out}} - C_{\text{in}}}. \tag{5.15}$$

This way of computing the visibility effectively inverts the HOM trace about the minimum (HOM filter OFF), turning the HOM peak into a HOM dip with zero absolute minimum, whose visibility can be calculated as in Eq. 5.14. Assume a minimum of 1 for the HOM peak signal ($C_{\text{out}} = 1$). Switching the HOM filter to the ON state leads to a maximum coincidence signal of 2 ($C_{\text{in}} = 2$), resulting in a maximum visibility of $\mathcal{V}_{\text{peak}} = 1$.

5.3 Tomography of the distilled states

Having established the reference point for the HOM filter (determination of the dip/peak position), we demonstrated the effectiveness of the distillation process by performing a quantum state tomography of the two-photon state with the HOM filter OFF/ON. Figure. 5.3(a) graphically depicts the joint projective measurements performed within the $\ell = \pm 1$ OAM subspace, to realise an over-complete quantum state tomography [128] with the HOM filter in the OFF state. We selected 6 different locations on the surface of the turbulence plate to implement our distillation scheme. The choice of location was solely guided by our need to cover a range of turbulence conditions. With the HOM filter still in the OFF state, we performed a tomography of the two-photon state at the six different locations, as shown in Fig. 5.3(b). As expected, the measurement outcomes wildly deviate in the presence of turbulence. We then repeated the measurement with

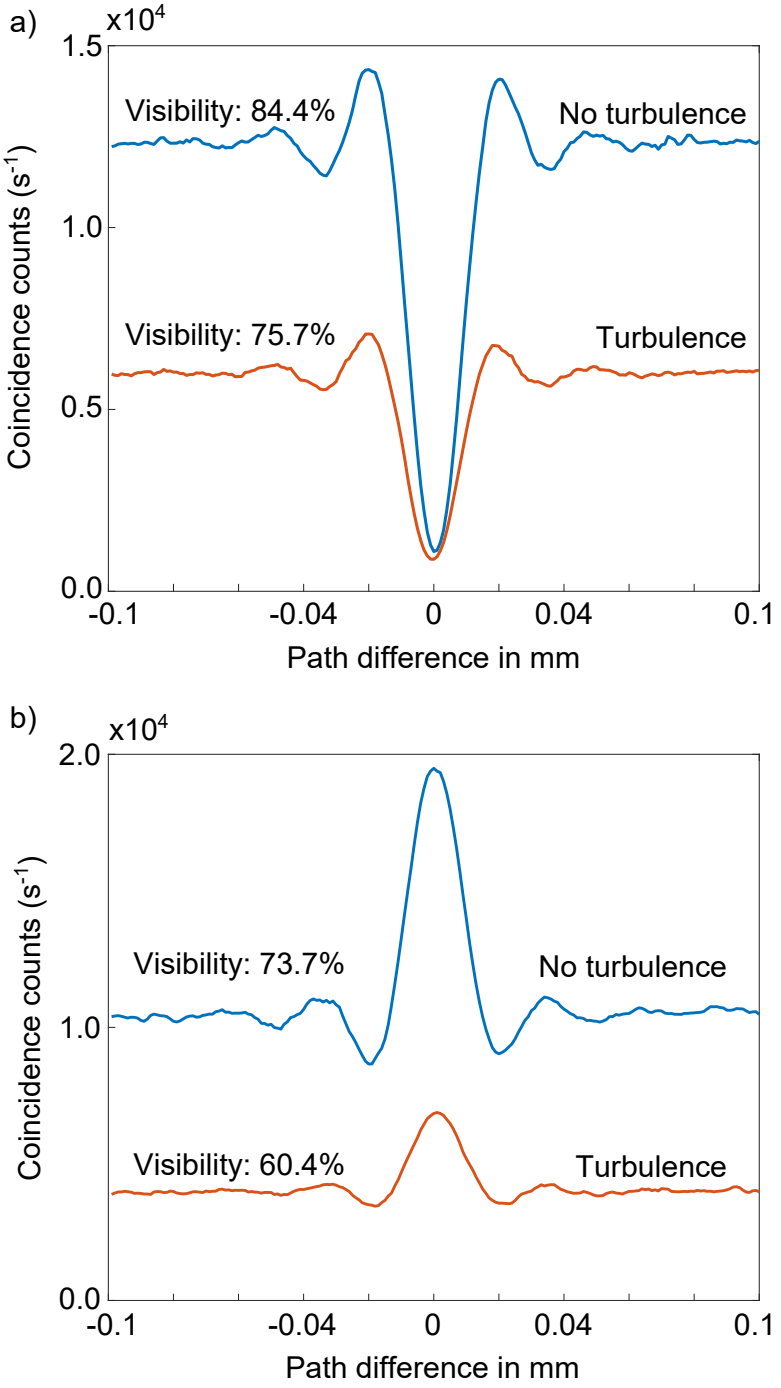


FIGURE 5.2: Hong-Ou-Mandel interference signal for (anti)symmetric states. Delaying one photon with respect to the other leads to (a) a dip and (b) a peak in coincidence counts for the symmetric ($\ell = 0$) and antisymmetric $\ell = \pm 1$ states, respectively. In the presence of turbulence, the visibility of the HOM interference decays in both subspaces, together with the coincidence counts.

the HOM filter in the ON state. Observe that with respect to the reference shown in Fig. 5.3(c), the tomographic measurements at the previous 6 locations [Fig. 5.3(d)] are qualitatively similar, indicating that the HOM filter is indeed distilling maximally entangled states.

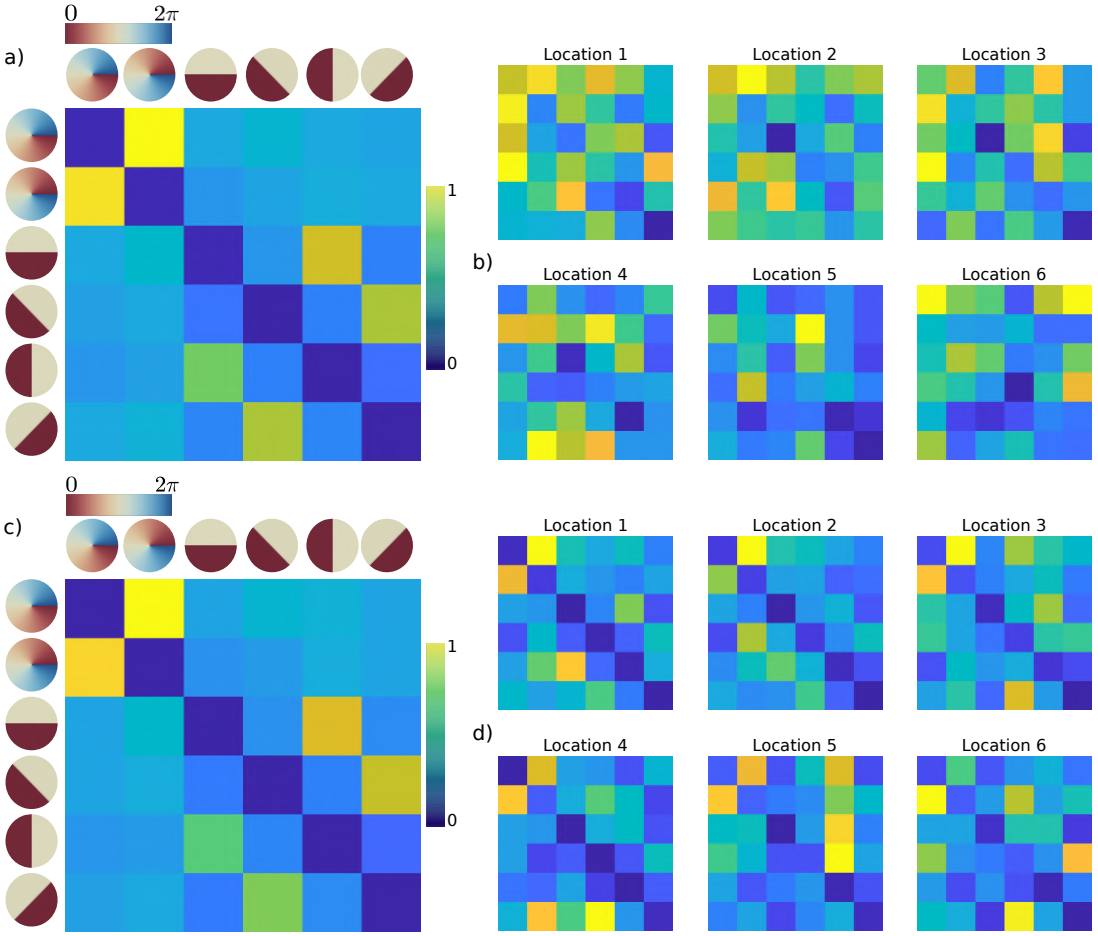


FIGURE 5.3: Quantum state tomography of two-photon state with HOM filter OFF/ON. (a) Shows the normalised tomographic measurement performed with the HOM filter OFF in the absence of turbulence. (b) We introduced the turbulence plate in the path of photon A and show the effect of turbulence on the state tomography measurement outcomes. We repeated the measurements, this time with the HOM filter ON (c) in the absence of turbulence and (d) for the same locations across the turbulence plate.

To each of these tomographic measurements, we can attach a quantitative measure to numerically demonstrate the efficacy of the HOM filter. Our figure of merit here is the fidelity, F, of the reconstructed two-photon density matrix ρ, with respect to the maximally entangled singlet state $\rho_T = |\Psi_\ell^-\rangle\langle\Psi_\ell^-|$:

$$F = \mathrm{tr}\left(\sqrt{\sqrt{\rho_T}\rho\sqrt{\rho_T}}\right)^2 = \langle\Psi_\ell^-|\,\rho\,|\Psi_\ell^-\rangle. \tag{5.16}$$

For each of the reference measurements in Figs. 5.3(a) and 5.3(c), the measured fidelity was in excess of 99%

When post-selecting the antisymmetric space $\ell = \pm 1$, we show that with the HOM filter OFF, the fidelity with respect to the maximally entangled singlet state decays as

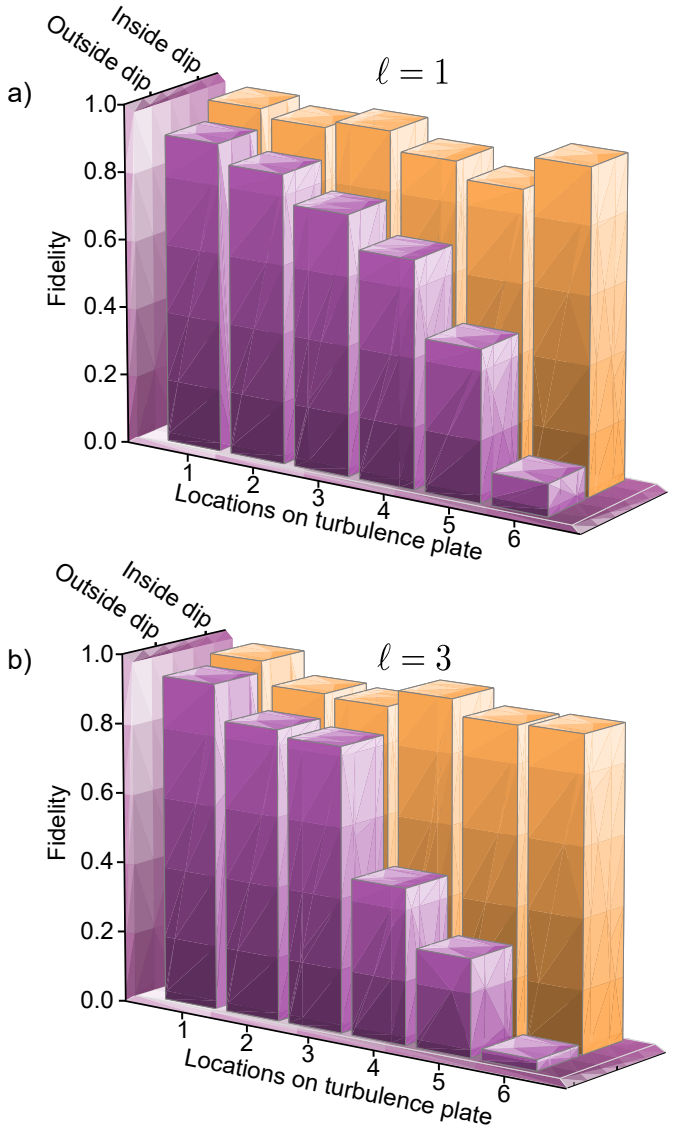


FIGURE 5.4: Distillation of singlet states. With the HOM filter in the OFF state (outside the dip) the fidelity of the measured state with respect to the singlet Bell state decays with increasing perturbations of the turbulence phase plate. Switching the filter to the ON state results in the distillation of states with high-fidelity with respect to the singlet Bell state. This is shown within the (a) $\ell = \pm 1$ and (b) $\ell = \pm 3$ subspaces.

shown in Fig 5.4(a), from 0.90 down to 0.095. However, with the HOM filter ON, the fidelity remains constant with $F > 0.85$ and consistently above the results with the filter OFF. We performed a similar set of measurements with the next antisymmetric subspace $\ell = \pm 3$. States within this subspace are more resilient to turbulence due to their larger separation in OAM space [178]. Using the same locations as before yielded relatively high fidelities without any significant spread. Therefore we chose another set of locations across the turbulence phase plate and compared the results with the HOM filter OFF and ON as shown in Fig. 5.4(b). Similarly to the previous case, with the HOM filter OFF we measured a decay of fidelity from 0.95 down to 0.032. When switching the

filter to the ON state, the fidelity remained consistently high for the various locations, with $F > 0.9$.

The distillation scheme we have demonstrated enables current and future quantum technologies. Turbulence makes it impractical to employ spatial modes for long distance quantum communication, with the measurement fidelity decaying with increasing turbulence. Our scheme enables one to recover, with high fidelity, information that would have otherwise been lost. The resilience of our scheme to a range of turbulence would enable robust quantum communication over significant distances. Furthermore, high-fidelity entangled states are critical resources to build a quantum repeater, a fundamental building block of quantum networks [179]. Our distillation scheme can be readily implemented with current technologies.

5.4 Conclusion

We have demonstrated an entanglement distillation scheme based on quantum interference of two entangled photons. The distillation process is realised by a Hong-Ou-Mandel filter that causes symmetric and antisymmetric Bell states to respectively bunch and anti-bunch upon exiting the filter through a 50:50 beam-splitter. By conditioning the detection system on coincidence between the output ports of the HOM filter, we have shown theoretically and experimentally the distillation of antisymmetric singlet states. The entanglement concentration process was tested for a coherent superposition of symmetric and antisymmetric state, produced by perturbing a singlet state with a one-sided weak turbulent channel. We have illustrated our distillation scheme by filtering OAM singlets carrying $\ell = \pm\hbar$ and $\ell = \pm 3\hbar$ quanta of OAM from an ensemble of non-maximally entangled pure states. When compared to a singlet Bell state, we have experimentally demonstrated the distillation of states with average fidelity higher than 90%, from an ensemble with average fidelity as low as 3%. The states distilled can reliably be used further in other quantum processes.

Chapter 6

A deterministic detector for vector vortex modes

This Chapter contains extracts from a publication by **Bienvenu Ndagano** *et al.* "A deterministic detector for vector vortex states". *Scientific Reports*, 7:13882, 2017.

Realising high-dimensional quantum communication remains challenging. One of the important issues to address and which is crucial to QKD, is the efficient detection of the prepared photon. It is well known that scalar spatial modes can be detected probabilistically with holographic filters that can be encoded on a spatial light modulator (SLM) [18], and deterministically with mode sorters [180]. In contrast, the detection of vector vortex modes is rather more complex, with tools existing at the many photon level [70, 71] but none to date for the deterministic detection at the single photon level. Here we introduce a new detection scheme that, deterministically and without dimension dependent photon loss, can detect all basis elements in our high-dimensional vector mode space. We achieve this through a two step process: using polarisation as a marker, we first sort the vector modes in two paths according to their intramodal phase (0 or π) through interference. The OAM carried by the photon in each path is then mapped to position using refractive OAM mode sorters [180–183]. The mapping of vector mode to position allows for the deterministic detection of higher dimensional state spaces, a feature particularly beneficial to QKD as it allows for high sifting rates. Likewise with classical communication where an improvement to signal-to-noise ratio over existing detection methods would be expected because the received signal is no longer distributed across many detectors. To demonstrate the detector, we present a simple prepare-and-measure QKD BB84 protocol using vector modes – and their mutually unbiased OAM scalar modes – within the $|\ell| = 1$ and $|\ell| = 10$ subspaces.

6.1 High dimensional encoding with vector vortex modes

Early QKD demonstrations were performed using the polarisation DoF, namely, states in the space spanned by left-circular $|L\rangle$ and right-circular polarisation $|R\rangle$, i.e., $\mathcal{H}_\sigma = \text{span}\{|L\rangle, |R\rangle\}$, and later using the spatial mode of light as a DoF, e.g., OAM with $\mathcal{H}_\ell = \text{span}\{|\ell\rangle, |-\ell\rangle\}$. Using entangled states in both DoFs allows one to access a large state space, $\mathcal{H}_{\sigma,\ell} = \mathcal{H}_\sigma \otimes \mathcal{H}_\ell$, described by the higher-order Poincaré sphere (HOPS) [38, 40], as shown graphically in Fig. 6.1 (a)-(d). Employing multiple OAM values the final state space is a direct sum of the subspaces $\mathcal{H}_{\sigma,\ell}$ for different ℓ:

$$\mathcal{H}_M = \bigoplus_{\ell \in M} \mathcal{H}_{\sigma,\ell}\,, \tag{6.1}$$

where $M \subset \mathbb{N}$ and the direct sum $\bigoplus$ of vector spaces A_i is given by $\bigoplus_i A_i = \{\sum_i \alpha_i |a_i\rangle : |a_i\rangle \in A_i, \alpha_i \in \mathbb{C}\}$. The dimension of $\mathcal{H}_M$ equals the sum of the dimensions of the subspaces $\mathcal{H}_{\sigma,\ell}$, i.e. $d = 4N$, with $N = |\Omega|$ being the number of different values of $|\ell|$ (the distinct subspaces or spheres). This opens the way to infinite dimensional encoding using such hybrid states. For example, using only the $|\ell|$ subspace of OAM leads to a four-dimensional space spanned by $\{|\ell, L\rangle, |-\ell, L\rangle, |\ell, R\rangle, |-\ell, R\rangle\}$. It is precisely in this four-dimensional subspace that, here, we define our vector and scalar modes: a vector mode set, $|\psi\rangle_{\ell,\theta}$, which forms four local Bell states with entangled internal degrees of freedom, and a mutually unbiased scalar mode set, $|\phi\rangle_{\ell,\theta}$, defined as

$$|\psi\rangle_{\ell,\theta} = \frac{1}{\sqrt{2}}(|R\rangle|\ell\rangle + e^{i\theta}|L\rangle|-\ell\rangle), \tag{6.2}$$

$$|\phi\rangle_{\ell,\theta} = \frac{1}{\sqrt{2}}\left(|R\rangle + e^{i(\theta-\frac{\pi}{2})}|L\rangle\right)|\ell\rangle, \tag{6.3}$$

where $\theta = 0$ or π is the intramodal phase. For a given $|\ell|$ OAM subspace, there exists a set of four orthogonal modes in both the vector basis (Eq. 6.2) and its mutually unbiased counterpart (Eq. 6.3), such that $|\langle\psi|\phi\rangle|^2 = 1/d$ with $d = 4$. Both mode sets can be generated by manipulating the dynamic or geometric phase of light [18, 41, 157, 184]. Here we employ geometric phase control through a combination of q-plates [62, 63] and wave plates to create all vector modes in the four-dimensional subspace defined by a fixed $|\ell|$. For the purpose of demonstration, we use vector and scalar modes in the $\ell = \pm 1$ and $\ell = \pm 10$ OAM subspaces, shown graphically in Figs. 6.1 (e) and (f) respectively. Table 6.1 details the combination of wave-plate and q-plates required to generate the vector modes in Fig. 6.1, given an input, horizontally polarised, Gaussian laser beam. For example, to produce a $|\psi\rangle_{-10,\pi}$ state, the horizontally polarised Gaussian laser beam is passed through HWP1 oriented at $\pi/4$ radians, then a q-plate with $q = 5$ and finally through HWP2 oriented at 0 radian.

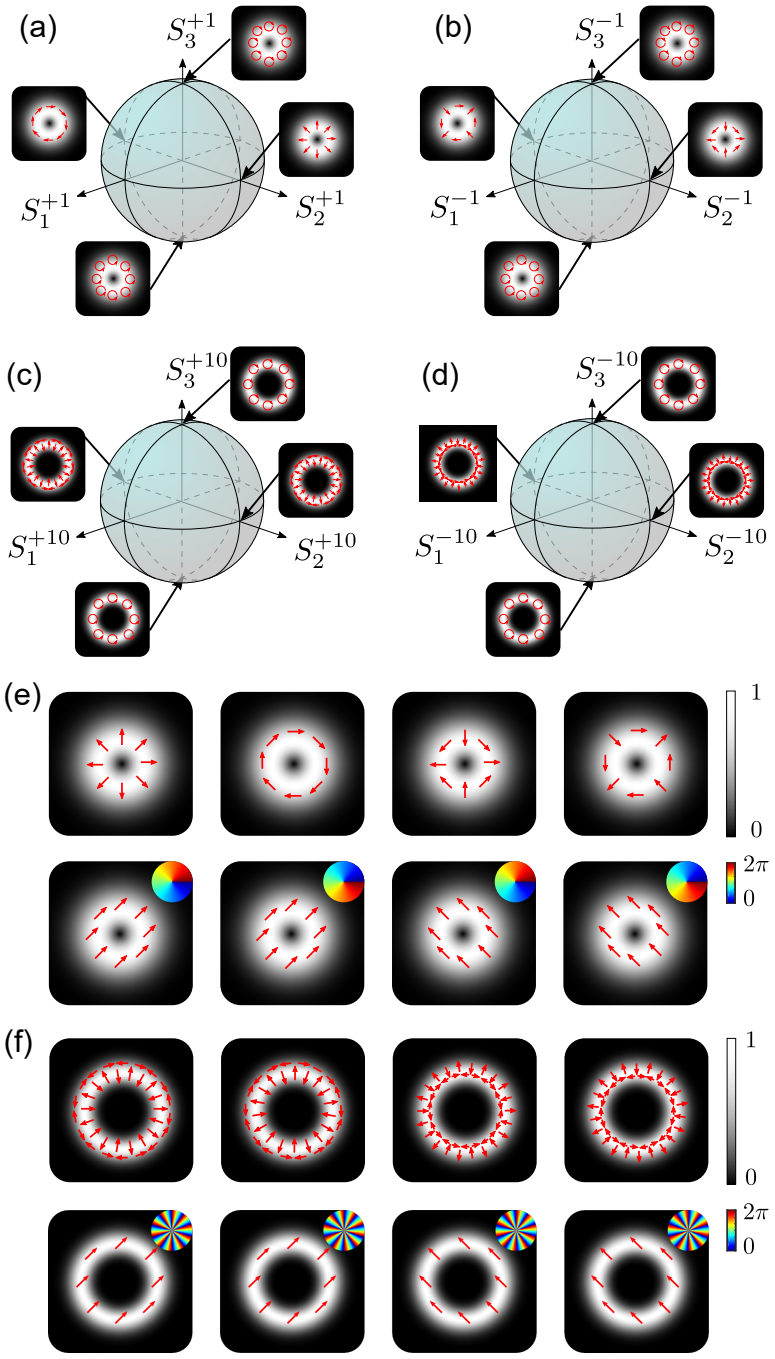


FIGURE 6.1: High–order Poincaré sphere (HOPS). We show the HOPS for the cases: (a) $\ell = 1$, (b) $\ell = -1$, (c) $\ell = 10$ and (d) $\ell = -10$. (e) and (f) show mutually unbiased vector and scalar vortex modes from, the $\ell = \pm 1$ and $\ell = \pm 10$ subspaces, respectively. The insets show the azimuthally varying phase profile of the scalar/OAM modes. Observe that the modes corresponding to the maximally entangled local local Bell states occur on the equator of the HOPS.

TABLE 6.1: Requirements for the generation of each of the four local local Bell states in the two subspaces of $|\ell| = 1$ and $|\ell| = 10$. The input state is a linearly polarised Gaussian beam and all angles are defined with respect to the horizontal axis. The experimental arrangements of the wave plates and q-plates is shown in Fig. 6.2(a).

Bell State	HWP1 angle (γ_1)	HWP2 angle (γ_2)	q
$\|\psi\rangle_{1,0}$	0	-	0.5
$\|\psi\rangle_{1,\pi}$	$\pi/4$	-	0.5
$\|\psi\rangle_{-1,0}$	0	0	0.5
$\|\psi\rangle_{-1,\pi}$	$\pi/4$	0	0.5
$\|\psi\rangle_{10,0}$	0	-	5
$\|\psi\rangle_{10,\pi}$	$\pi/4$	-	5
$\|\psi\rangle_{-10,0}$	0	0	5
$\|\psi\rangle_{-10,\pi}$	$\pi/4$	0	5

6.2 Deterministic detection

We now introduce a new scheme to deterministically detect the vector vortex modes, as detailed in Fig. 6.2(a), that has a number of practical advantages for classical and quantum communication. Consider a vector mode as defined in Eq. 6.2. The sorting of the different vector modes is achieved through a combination of geometric phase control and multi-path interference. First, a polarisation grating [185] based on geometric phase acts as a beam splitter for left- and right-circularly polarised photons, creating two paths (a and b)

$$|\psi\rangle_{\ell,\theta} \rightarrow \frac{1}{\sqrt{2}}\left(|R\rangle_a |\ell\rangle_a + e^{i\theta}|L\rangle_b |-\ell\rangle_b\right), \tag{6.4}$$

where the subscript a and b refer to the polarisation-marked paths. The photon paths a and b are interfered at a 50:50 BS, resulting in the following state after the BS:

$$|\psi'\rangle_{\ell,\theta} = \frac{1+e^{i(\delta+\theta+\frac{\pi}{2})}}{2}|\ell\rangle_c |R\rangle_c + i\frac{1+e^{i(\delta+\theta-\frac{\pi}{2})}}{2}|-\ell\rangle_d |L\rangle_d \tag{6.5}$$

where the subscripts c and d refer to the output ports of the beam splitter and δ is the dynamic phase difference between the two paths. Note that the polarisation of the two paths is automatically reconciled in each of the output ports of the beam splitter due to the difference of parity in the number of reflections for each input arm. Also note that at this point it is not necessary to retain the polarisation kets in the expression of the photon state since the polarisation information is contained in the path. In our setup we set $\delta = \pi/2$, reducing the state in Eq. 6.5 to

$$|\psi'\rangle_{\ell,\theta} = \frac{1-e^{i\theta}}{2}|\ell\rangle_c + i\frac{1+e^{i\theta}}{2}|-\ell\rangle_d \tag{6.6}$$

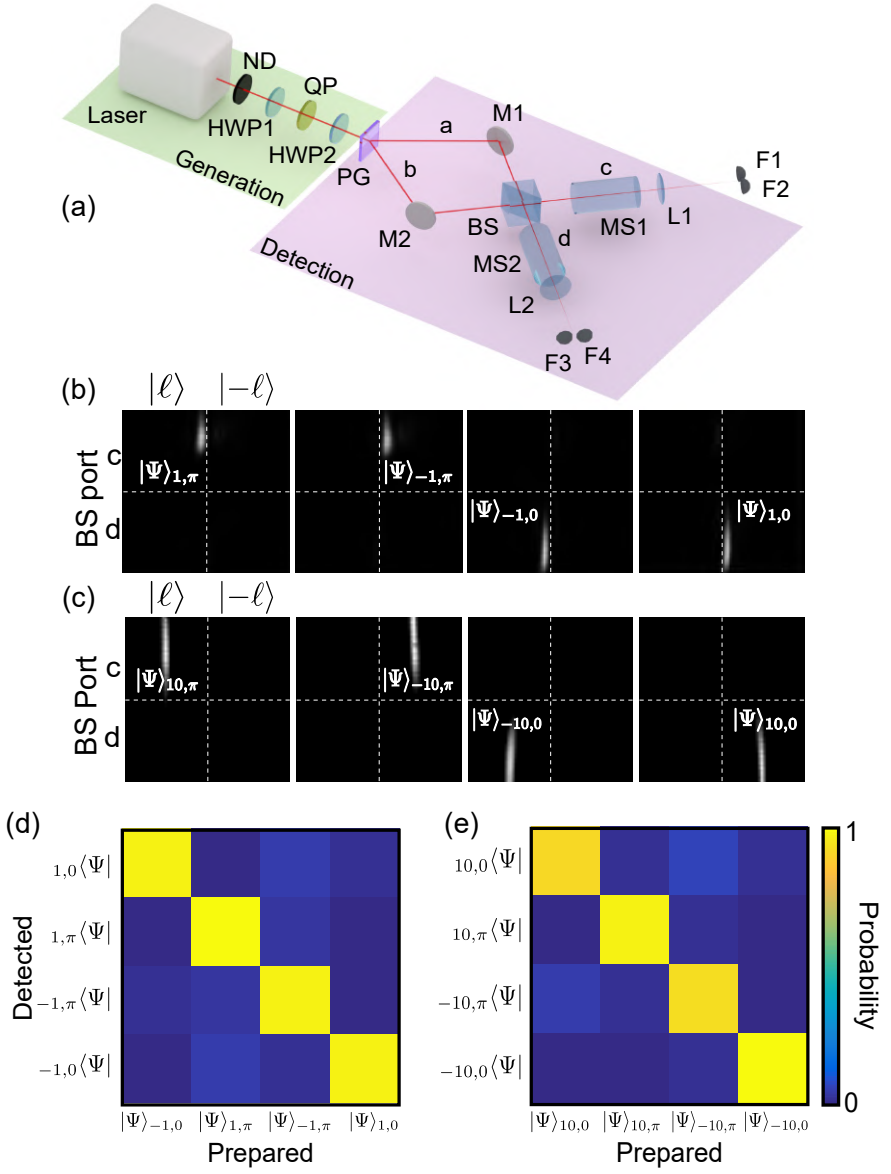


FIGURE 6.2: Deterministic detection of vector vortex modes. (a) A vector beam is generated by shaping attenuated light from a He-Ne laser with geometric phase optics: half-wave plates (HWP1 and HWP2) and a q-plate (QP). A polarisation grating (PG) maps circular polarisation to two paths, a and b, which are then interfered at a 50:50 beam-splitter (BS). Subsequently the OAM states are measured using mode sorters (MS1 and MS2) that map OAM to position. The output ports (c or d) of the BS and the lateral locations ($|\ell\rangle$ or $|-\ell\rangle$) deterministically indicate the Bell state being measured by the detectors F1–F4. Experimental results from the spatial sorting of vector modes are shown in (b) for $\ell = \pm 1$ and (c) for $\ell = \pm 10$, with crosstalk matrices for these subspaces shown in (d) and (e). M1 and M2 are mirrors; L1 and L2 are lenses, and F1–F4 are multimode fibers.

The measurement system is completed by passing each of the outputs in c and d through a mode sorter to path split the positive and negative ℓ states, and collecting these photons using 4 fibres coupled to photodiodes F_i. The mode sorters are refractive (lossless) aspheres that map OAM to position [180–183]. The first optical element of the

sorter unwraps the OAM modes while the second acts a phase corrector by stopping the unwrapping process. The result is a transformation from an azimuthal to linear phase with a gradient proportional to the OAM charge incident on the sorter. The modes map according to

$$|\psi\rangle_{\ell,0} \rightarrow i\,|-\ell\rangle_d \rightarrow \mathrm{F}_4, \tag{6.7}$$

$$|\psi\rangle_{\ell,\pi} \rightarrow |\ell\rangle_c \rightarrow \mathrm{F}_2, \tag{6.8}$$

$$|\psi\rangle_{-\ell,0} \rightarrow i\,|\ell\rangle_d \rightarrow \mathrm{F}_3, \tag{6.9}$$

$$|\psi\rangle_{-\ell,\pi} \rightarrow |-\ell\rangle_c \rightarrow \mathrm{F}_1. \tag{6.10}$$

where the indices c and d label the output ports of the BS. For example, the Bell state $|\psi\rangle_{\ell,0}$, which is known as radially polarised light at the classical level, is directed to path d and detector F3 ($|-\ell\rangle$), thus making the detection deterministic, and likewise for all the other states. This is shown in Fig. 6.2(b) and (c) for the two subspaces $\ell = \pm 1$ and $\ell = \pm 10$, where all the vector modes under study are mapped to unique positions at the detector plane. While it is trivial to measure such vector states at the classical level with many photons [70, 71, 144], with our approach each single photon Bell state is detected with, in principle, unit probability at the single photon level. Figure 6.2 (d) and (e) shows the probability of detection of single photons for different HOPS local Bell states ($\ell = \pm 1$ and $\ell = \pm 10$). The depicted results validates our proposal as a highly efficient method to sort local Bell states with in principle unit probability. Observe that the detected states are in excellent agreement with the generated local Bell states for all cases. In classical optics such non–separable states, also known as vector vortex beams, have been widely studied. Under this regime our detection apparatus also works but with a $d\times$ signal-to-noise as the incoming signal is not distributed across d detectors, where d is the number of classical modes in the set.

Finally, Fig. 6.3 shows the results for the detection of photons in superpositions of our vector basis. This task is performed by changing the angle γ_1 of the HWP1 and measuring the intensity in each output port of the setup. The experimental results (data points) are in excellent agreement with theory (dashed curves), validating that arbitrary superpositions may also be detected with high fidelity. Note that the detection of the mutually unbiased scalar mode works in an analogous manner, with the exception that the BS is removed since there is no need to resolve intermodal phases to recover the vector nature of the mode.

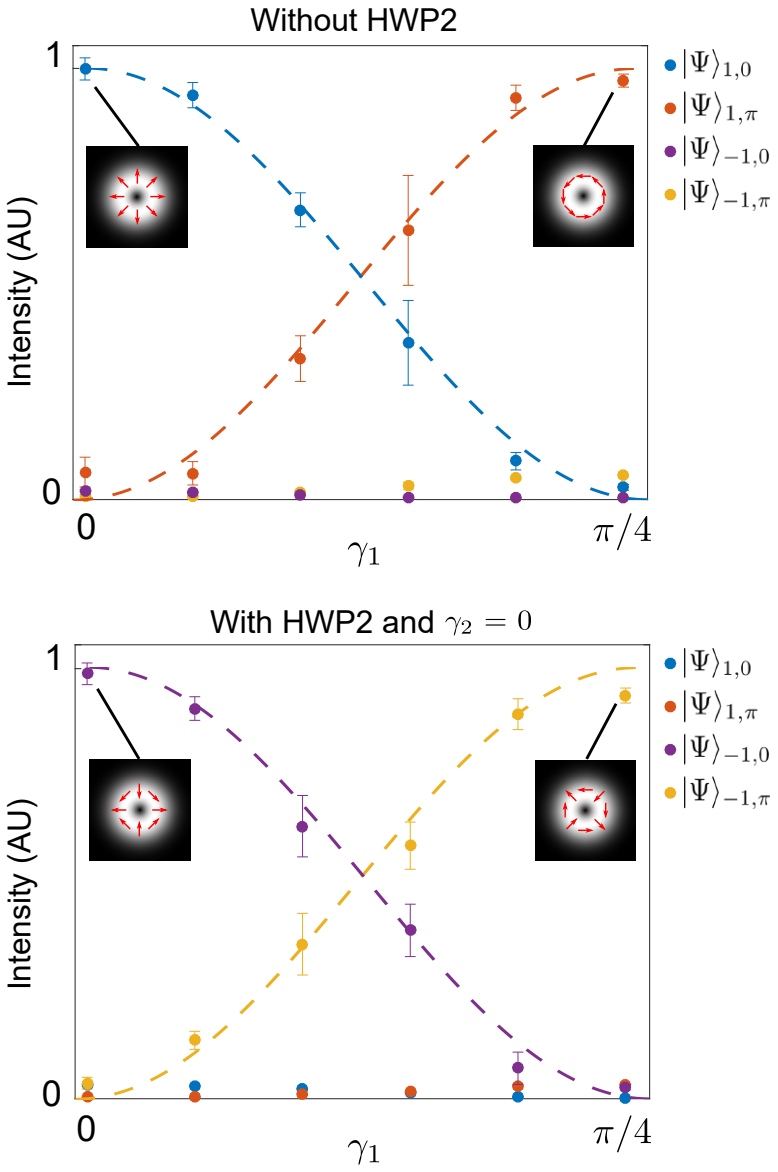


FIGURE 6.3: Detection of superpositions of vector states. The two graphs show detection (normalised intensity) of superpositions of states from our vector basis. The superpositions were created by changing the HWP angle γ_1 (cp. Table 6.1). Each point was generated by averaging 30 measurements. The dashed lines represent the theoretical curve.

6.3 Deterministic and filter based detection

The advantage of our approach is graphically depicted in Fig. 6.4(a), where we plot, as a function of the dimension, the photon efficiency of the detection: defined as $1 - S$ where S is the fraction of photons whose information is lost due to measurement approach. Since a filter can only probe one spatial mode at the time, the measurement of a d-dimensional state will return a positive detection with an average probability $\leq 1/d$. In two dimensions, and assuming unit detection efficiency for every input state, two modes

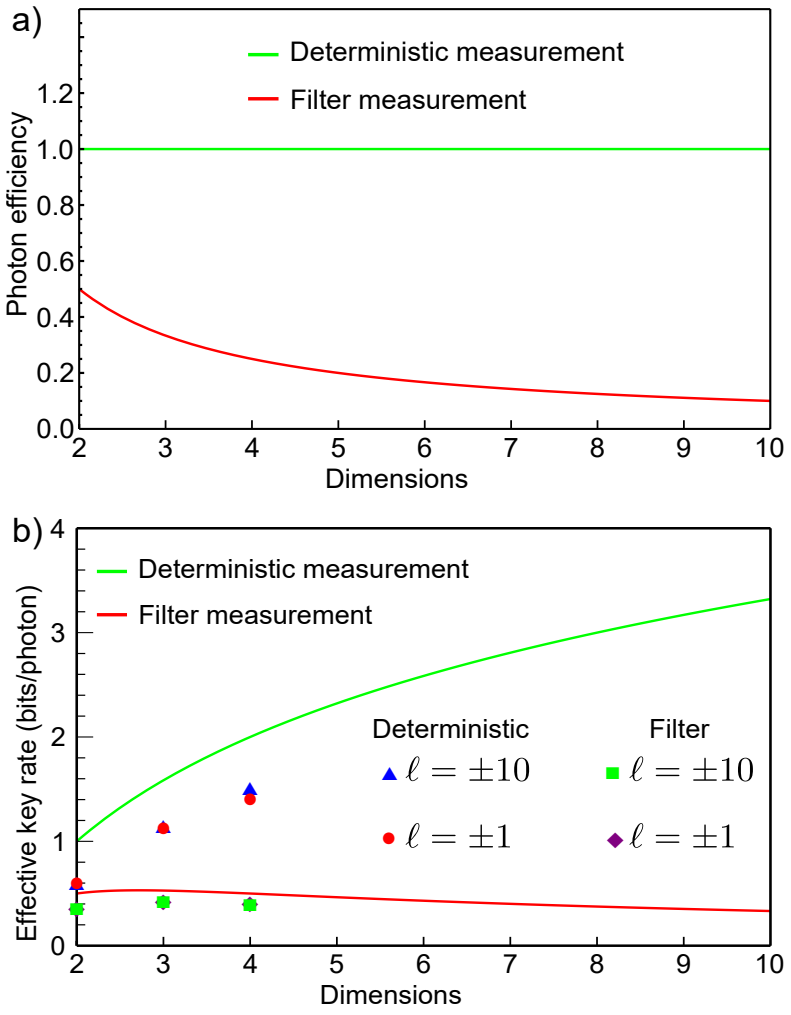


FIGURE 6.4: (a) Photon efficiency as a function of dimension for a deterministic and filter-based measurement scheme. (b) Effective key rate as a function of dimension shown experimentally (data points) for two measurement approaches, namely, filtering and deterministic detection. Data points show measurements in the subspaces of $\ell = \pm 1$ and $\ell = \pm 10$ for $d = 2$,3 and 4. The measurement fidelities for $\ell = \pm 1$ and $\ell = \pm 10$ were measured to be 0.96 and 0.97, respectively. The solid curves are theoretical bounds on the effective key rate assuming a fidelity of 1.

can be detected using a single detector by inferring the detection probabilities; given that the probability of a detection in detector A is p_A, the probability of detection in detector B is thus $1 - p_A$.

Our system on the other hand does not suffer any dimension dependent loss. This would make it particularly beneficial to both classical communication through mode-division multiplexing with higher signal-to-noise ratio, as well as high efficiency quantum communication in the form of high-dimensional quantum key distribution. The latter is graphically illustrated in Fig. 6.4(b) where we plotted theoretical and experimental data of the photon information capacity as a function of the dimension. By photon information capacity we mean the d-dimensional effective key rate as defined in [153],

taking into account detection efficiency. Note that the filter-based detection has key rates well below the qubit (d=2) maximum of 1 bit per photon.

6.4 Application to quantum key distribution

We performed a four-dimensional prepare-and-measure BB84 QKD protocol [150] using the mutually unbiased vector and scalar modes given earlier, namely, a vector mode set, $|\psi\rangle_{\ell,\theta}$, and a mutually unbiased scalar mode set, $|\phi\rangle_{\ell,\theta}$. For a given $|\ell|$ OAM subspace, there exists a set of four orthogonal modes in both the vector basis (Eq. 6.2) and its mutually unbiased counterpart (Eq. 6.3). Our four vector modes for QKD then become:

$$|00\rangle_v = \frac{1}{\sqrt{2}}(|R\rangle|\ell\rangle + |L\rangle|-\ell\rangle), \tag{6.11}$$

$$|01\rangle_v = \frac{1}{\sqrt{2}}(|R\rangle|\ell\rangle - |L\rangle|-\ell\rangle), \tag{6.12}$$

$$|10\rangle_v = \frac{1}{\sqrt{2}}(|L\rangle|\ell\rangle + |R\rangle|-\ell\rangle), \tag{6.13}$$

$$|11\rangle_v = \frac{1}{\sqrt{2}}(|L\rangle|\ell\rangle - |R\rangle|-\ell\rangle), \tag{6.14}$$

with corresponding mutually unbiased bases (MUB)

$$|00\rangle_s = |D\rangle|-\ell\rangle, \tag{6.15}$$

$$|01\rangle_s = |D\rangle|\ell\rangle, \tag{6.16}$$

$$|10\rangle_s = |A\rangle|-\ell\rangle, \tag{6.17}$$

$$|11\rangle_s = |A\rangle|\ell\rangle, \tag{6.18}$$

where the subscripts s and v refer to, respectively, the scalar and vector mode basis, while D and A are the diagonal and anti-diagonal polarisation states.

Light from our source was attenuated to an average photon number of $\mu = 0.008$ per pulse. Note that while such weak coherent states cannot be used for QKD without photon splitting strategies, it is a suitable demonstration of the detection scheme, which is our aim here. Alice prepared an initial state in either the vector or scalar basis and transmitted it to Bob, who made his measurements as detailed in the previous section with deterministic vector and scalar mode detectors. Through optical projection onto both the vector and scalar bases as illustrated in Fig. 6.5(a), we determined the crosstalk matrices shown theoretically in Fig. 6.5 (b) and experimentally in (c) and (d), relating the input and measured modes within, respectively, the subspaces $\ell = \pm 1$ and $\ell = \pm 10$.

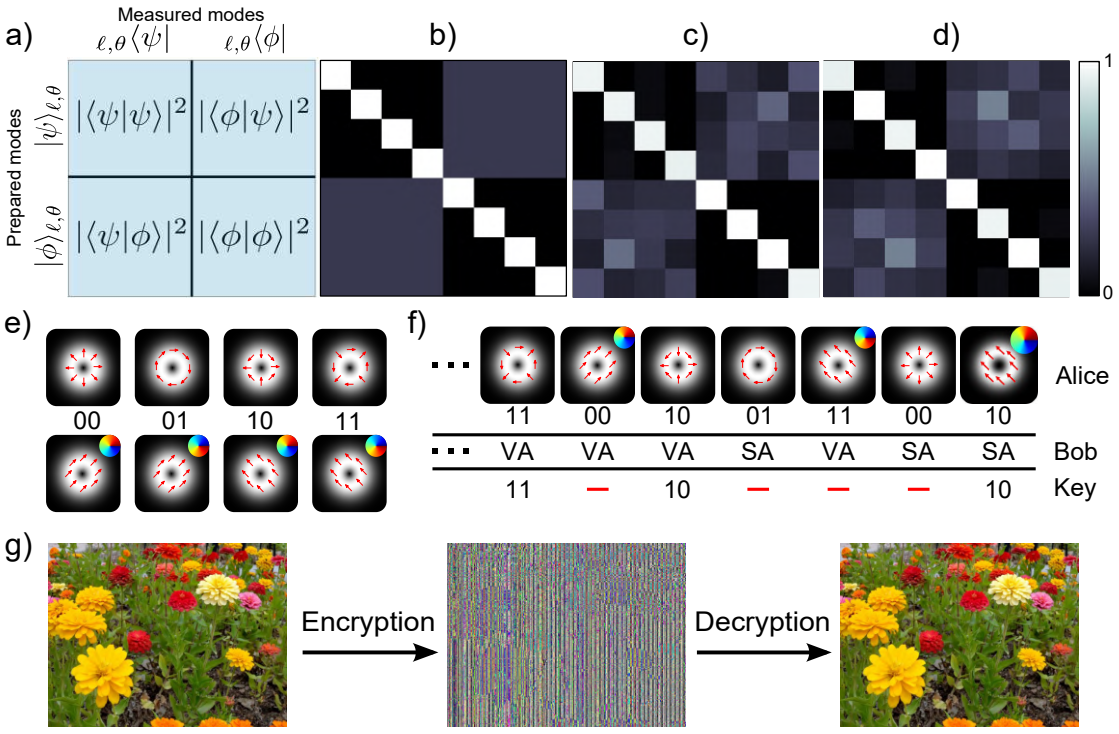


FIGURE 6.5: High dimensional QKD with vector modes. (a) Schematic of the inner product measurements performed between the vector states and their mutually unbiased counterparts, (b) theoretical scattering probabilities among the vector and scalar modes following the measurement procedure in (a), and experimental results for the (c) $\ell = \pm 1$ and (d) $\ell = \pm 10$ subspaces. (e) Alice and Bob agree on bit values for the vector and scalar modes. (f) Alice sends a random sequence of vector and scalar modes, which Bob randomly measures using either a vector analyser (VA) or a scalar analyser (SA). Alice and Bob, upon communication of the encoding and decoding bases through a classical channel, discard bit values for modes prepared and measured in complementary bases. (g) Shows a simple encryption/decryption of an image using a 98 bit long key, sifted from a total of 200 transmitted bits. Photo courtesy photos-public-domain.com.

The average fidelity of detection, measured for modes prepared and detected in identical bases, is $F = 0.965 \pm 0.004$ while the overlap between modes from mutually unbiased bases is $|\langle\phi|\psi\rangle|^2 = 0.255 \pm 0.004$, in good agreement with the theoretical value of 0.25.

For each mode, Alice and Bob assign the bit values $00, 01, 10$ and 11, as shown in Fig. 6.5(e). During the transmission, Alice randomly prepares her photon and Bob randomly measures the photon with either the vector or scalar analyser (the scalar analyser is the vector analyser discussed earlier but without the beam splitter). At the end of the transmission, Alice and Bob reconcile the prepare and measure bases and discard measurements in complementary bases, as illustrated in Fig. 6.5(f). We performed this transmission using a sequence of 100 modes and retained a sifted key of 49 spatial modes (98 bits), which was used to encrypt and decrypt a picture as shown in Fig. 6.5(g).

From the measured crosstalk matrices in Fig. 6.5(c) and (d), we performed a security

analysis on our QKD scheme in dimensions $d = 4$ for the two OAM subspaces (± 1 and ± 10). The results of the analysis are summarised in Table 6.2. From the measured detection fidelity F, we computed the mutual information between Alice and Bob in d-dimensions as follows [25]

$$I_{AB} = \log_2(d) + F\log_2(F) + (1-F)\log_2\left(\frac{1-F}{d-1}\right). \tag{6.19}$$

The measured I_{AB} for $d = 4$ is nearly double ($1.7\times$) that of the maximum achievable with only qubit states (1). Assuming a third party, Eve, uses an ideal quantum cloning machine to extract information, the associated cloning fidelity, F_E, in d-dimensions is given by [25]

$$F_E = \frac{F}{d} + \frac{(d-1)(1-F)}{d} + \frac{2\sqrt{(d-1)F(1-F)}}{d}. \tag{6.20}$$

With increasing dimensions, the four-dimensional protocol reduces the efficiency of Eve's cloning machine to as low as 0.38 well below the maximum limit in a two-dimensional protocol (0.5). Thus, increasing the dimensionality of QKD protocols does indeed have, in addition to higher mutual information capacity, higher robustness to cloning based attacks. We emphasise here that we take the case of cloning based attacks was used to illustrate a proof-of-concept; that is, increasing the dimensionality of quantum protocols provides added security benefits.

The mutual information shared between Alice and Bob, conditioned on Bob's error – that is, Bob making a wrong measurement is as a result of Eve extracting the correct information – is computed in d-dimension as follows [186]

$$I_{AE} = \log_2(d) + (F + F_E - 1)\log_2\left(\frac{F + F_E - 1}{F}\right) + (1-F_E)\log_2\left(\frac{1-F_E}{(d-1)F}\right). \tag{6.21}$$

The consequent measured quantum error rate of $Q = 1 - F = 0.04$ is well below the 0.11 and 0.18 bounds for unconditional security against coherent attacks in two and four dimensions [186], respectively. The lower bound on the secret key rate, given by [153]

$$R = \log_2(d) + 2F\log_2(F) + 2(1-F)\log_2\left(\frac{1-F}{d-1}\right), \tag{6.22}$$

yields a value as high as 1.52 bits per photon, well above the Shannon limit of one bit per photon achievable with qubit states. While the security of the protocol can be increased with privacy amplification, the measured four-dimensional secret key rate demonstrates the potential of such entangled modes for high bandwidth quantum communication.

We emphasise that the above demonstration serves to outline the benefits of this basis set for QKD, which is now feasible given the deterministic detector proposed here. Our

TABLE 6.2: Summary of the security analysis on the high dimensional protocol showing the experimental and theoretical values of the detection fidelity (F), mutual information I_{AB} between Alice and Bob, Eve's cloning fidelity (F_E) and mutual information with Alice I_{AE}, as well as the quantum error rate Q and information capacity per photon R in bits per photon.

	$d = 4$ ($\ell = \pm 1$)	$d = 4$ ($\ell = \pm 10$)	
Measures	experiment	experiment	ideal
F	0.96	0.97	1.00
I_{AB}	1.69	1.76	2.00
F_E	0.44	0.41	0.25
I_{AE}	0.17	0.13	0.00
Q	0.04	0.03	0.00
R	1.39	1.52	2.00

work highlights that the deterministic detection of vector vortex modes would result in higher sift rates when compared to filter based methods [104], crucial for maintaining the benefits of increased dimensions in the state space. In the case where filters are used to distinguish a single basis element from all others, the probability to choose the filter that corresponds to the sent signal state is given by $2/d$. As such, using a filter based detection, the sifting loss grows with the dimension d, unlike with a deterministic detector which would be unaffected by the larger state space. For example, in the demonstration shown in Fig. 6.5, filtering one mode at the time would only yield a raw key that is, on average, 50 bits long; that is because a maximum of two vector modes can be distinguished in a single shot measurement using a q-plate as a filter [71].

6.5 Conclusion

In this work we presented a deterministic measurement scheme where many and single photon local Bell states in the form of vector vortex modes were sorted and detected with, in principle, unit detection probability. Since each mode maps to a unique position in the spatial domain, such a detection will not suffer from any dimension-dependent loss. In QKD, where photon loss as a result of the measurement procedure affects the efficiency of the transmission, our scheme makes it possible to increase the dimensionality without compromising on the sifting rate. We point out that our scheme would likewise increase the signal-to-noise of classical mode-division multiplexing communication systems: rather than distribute the signal across d modes, each with $1/d$ of the signal, we can achieve full signal on each mode with a factor d greater signal-to-noise ratio [187]. A major advantage we offer is that all modes in our Hilbert space are eigenmodes of free-space [149, 188] and optical fibre [70], thus facilitating long distance applications outside the laboratory environment.

Chapter 7

Conclusion

The tools we have provided in the present Thesis were designed to realise the potential of spatial modes in enabling quantum processes. It is however important to place our findings in the context of current research trends. Figure 7.1 is a map of the major advancements that have been realised in the context of entanglement engineering and control using photons. The goal in the field is to realise multipartite entanglement in high dimension. However, progress in meeting both criteria is scarce and non-trivial. To date, much work has been aimed in realising either multipartite qubit entanglement or high-dimensional bipartite entanglement.

In Chapter 1, we have introduced the concept of entanglement at both the quantum and classical level. The central idea was that at the heart of entanglement lies non-separability between the state that are said to be entangled. However this non-separability is not unique to quantum systems. Indeed classical states of light can and do exhibit non-separability in their degrees of freedom. Due to the local nature of these classical correlations, such non-separable states are said to be classically entangled. The concept of classical entanglement is fascinating and intriguing, as one ponders on the similarities between quantum and classically entangled states within the domain of local processes. Can we find analogies between these two flavours of entanglement?

The first affirmative answer was given in Chapter 2 where we provided means to generate and measure classically entangled states. We showed that through dynamic and geometric phase control, one could tailor and quantitatively measure arbitrary non-separable states of classical light. In addition, we presented the concept of quantum state tomography applied to classical light. Quantum state tomography is, as its name suggests, a technique traditionally associated with the measurement of quantum states and is a particularly powerful tool to reconstruct the density matrix of entangled states. We

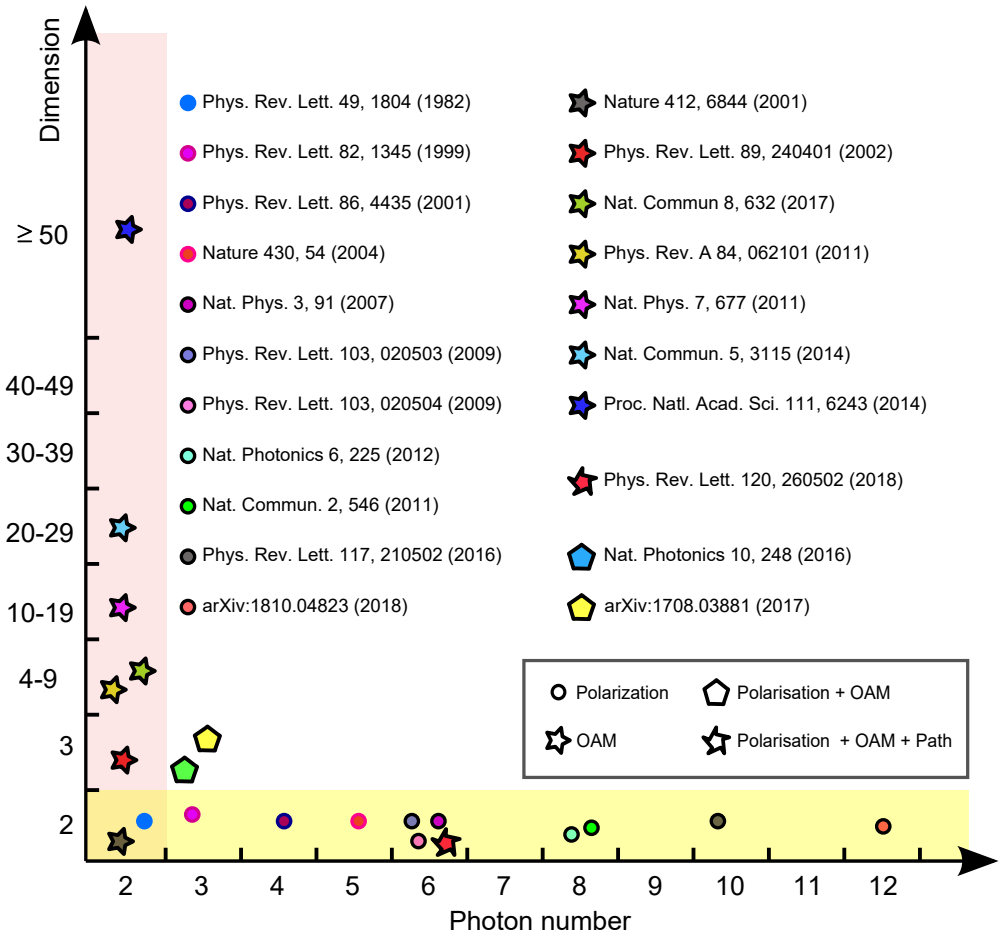


FIGURE 7.1: Historical trends in photonic entanglement engineering and control.

applied the procedure to classical light and show the reconstruction of the density matrix of classically entangled vector beams. This provided the tools to explore analogies between classical and quantum entanglement in the next Chapter.

Though photonic entanglement with spatial mode is full of promises, such entangled states are fragile and decay in the presence of external perturbations such as atmospheric turbulence. And while a characterisation of the perturbations would assist in designing error correction strategies, the sparsity of entangled photons pairs in quantum experiments makes establishing a working link through the perturbations very difficult. In Chapter 3, we circumvented this hurdle using bright classical light. We showed that the decay of classical and quantum entanglement in a one-sided turbulent channel are equivalent and indistinguishable, opening the door to the characterisation of the quantum link with bright classical sources. In addition, we show that the decay of entanglement in the channel for an arbitrary input state can be predicted if one knows the dynamics of the maximally entangled classical beam. The ability to predict bipartite entanglement dynamics using classical light places our findings firmly in the bottom left of the plot in Fig. 7.1.

In Chapter 4 we explored means to mitigate the effects of turbulence on the quantum link we studied in Chapter 3. Particularly, we showed that employing entangled states with larger mode separation increases the robustness of the quantum link as they experience less crosstalk. And while this has been shown for two-dimensional states, it can equally be applied to high-dimensional ones to realise quantum communication with more bits per photon. Furthermore we showed that by implementing a high-dimensional detection on a perturbed qubit state, one is able recover photons and information that would have otherwise been lost as a result of post-selection. Lastly, we demonstrated the concentration of entanglement by Procrustean filtering on one party in the entangled pair. This involved probing the perturbing channel with classically entangled light as shown in Chapter 3 and performing local projections on one party in the entangled pair. With regards to Fig. 7.1, the tools we present here further our ability to realise robust quantum communication with entangled bipartite quantum states in two and higher dimensions,

Chapter 5 further explored the idea of entanglement concentration after turbulence. Unlike the Procrustean filtering presented in Chapter 4, we introduced a 'blind' passive method to distil entanglement by quantum state interference. This approach uses the Hong-Ou-Mandel effect to filter singlet Bell states from an ensemble of photons with near-zero degree of entanglement. The distillation scheme we have demonstrated enables current and future quantum technologies. Turbulence makes it impractical to employ spatial modes for long distance quantum communication, with the measurement fidelity decaying with increasing turbulence. Our scheme enables one to recover, with high fidelity, information that would have otherwise been lost. The resilience of our scheme to a range of turbulence strengths would enable robust quantum communication over significant distances. Furthermore, high-fidelity entangled states are critical resources to build a quantum repeater, a fundamental building block of quantum networks [179]. Our distillation scheme can be readily implemented with current technologies. In distilling singlet states in high-dimensions, our scheme (with respect to Fig. 7.1) would also allow for high-dimensional state engineering and control in the presence of noise.

Finally in Chapter 6, we tackled the problem of dimension-dependent losses in the context of quantum key distribution with spatial modes. In particular, we considered single photons encoded in a vector vortex mode basis, for which only probabilistic vector mode detectors were available. We introduced a detector that deterministically maps vector modes to distinct positions at the detector plane with, in principle, unit efficiency. Unlike probabilistic filter-based detectors, our scheme does not suffer from dimension-dependent losses, allowing us to take full advantage of the larger Hilbert space of vector modes to realise a four-dimensional quantum key distribution protocol. This was demonstrated

with vector modes in the $\ell = \pm 1$ and $\ell = \pm 10$ OAM subspaces. An outdoor demonstration of this protocol has been realised by Sit *et al.* using a filter-based detection [24]. Using our approach would, in principle, have allowed Sit *et al.* to double their photon sifting rates. With regards to Fig. 7.1, this presents significant advantages to efficiently implement high-dimensional communication with two-photon entangled vector vortex states [189].

Bibliography

[1] S. Barnett, *Quantum information*, vol. 16. Oxford University Press, 2009.

[2] J. L. O'Brien, "Optical Quantum Computing," *Science*, vol. 318, p. 1567, 2007.

[3] J. L. O'Brien, A. Furusawa, and J. Vučković, "Photonic quantum technologies," *Nature Photonics*, vol. 3, p. 687, 2009.

[4] E. Conover, "Google moves toward quantum supremacy with 72-qubit computer," *Science News*, 2018.

[5] X.-S. Ma, T. Herbst, T. Scheidl, D. Wang, S. Kropatschek, W. Naylor, B. Wittmann, A. Mech, J. Kofler, E. Anisimova, V. Makarov, T. Jennewein, R. Ursin, and A. Zeilinger, "Quantum teleportation over 143 kilometres using active feed-forward.," *Nature*, vol. 489, p. 269, 2012.

[6] J. Yin, Y. Cao, Y.-H. Li, S.-K. Liao, L. Zhang, J.-G. Ren, W.-Q. Cai, W.-Y. Liu, B. Li, H. Dai, G.-B. Li, Q.-M. Lu, Y.-H. Gong, Y. Xu, S.-L. Li, F.-Z. Li, Y.-Y. Yin, Z.-Q. Jiang, M. Li, J.-J. Jia, G. Ren, D. He, Y.-L. Zhou, X.-X. Zhang, N. Wang, X. Chang, Z.-C. Zhu, N.-L. Liu, Y.-A. Chen, C.-Y. Lu, R. Shu, C.-Z. Peng, J.-Y. Wang, and J.-W. Pan, "Satellite-based entanglement distribution over 1200 kilometers," *Science*, vol. 356, p. 1140, 2017.

[7] A. Zeilinger, "Quantum teleportation, onwards and upwards," *Nature Physics*, vol. 14, p. 3, 2018.

[8] F. Töppel, A. Aiello, C. Marquardt, E. Giacobino, and G. Leuchs, "Classical entanglement in polarization metrology," *New Journal of Physics*, vol. 16, p. 073019, 2014.

[9] E. Karimi and R. W. Boyd, "Classical entanglement?," *Science*, vol. 350, p. 1172, 2015.

[10] P. Ghose and A. Mukherjee, "Entanglement in classical optics," *Reviews in Theoretical Science*, vol. 2, p. 274, 2014.

[11] L. J. Pereira, A. Z. Khoury, and K. Dechoum, "Quantum and classical separability of spin-orbit laser modes," *Physical Review A*, vol. 90, p. 053842, 2014.

[12] R. A. Beth, "Mechanical Detection and Measurement of the Angular Momentum of Light," *Physical Review*, vol. 50, p. 115, 1936.

[13] U. Fano, "Description of States in Quantum Mechanics by Density Matrix and Operator Techniques," *Reviews of Modern Physics*, vol. 29, p. 74, 1957.

[14] J. B. Altepeter, E. R. Jeffrey, and P. G. Kwiat, "Photonic state tomography," *Advances in Atomic, Molecular, and Optical Physics*, vol. 52, p. 105, 2005.

[15] S. Franke-Arnold, L. Allen, and M. Padgett, "Advances in optical angular momentum," *Laser and Photonics Reviews*, vol. 2, p. 299, 2008.

[16] A. M. Yao and M. J. Padgett, "Orbital angular momentum: origins, behavior and applications," *Advances in Optics and Photonics*, vol. 3, p. 161, 2011.

[17] A. E. Willner, H. Huang, Y. Yan, Y. Ren, N. Ahmed, G. Xie, C. Bao, L. Li, Y. Cao, Z. Zhao, J. Wang, M. P. J. Lavery, M. Tur, S. Ramachandran, A. F. Molisch, N. Ashrafi, and S. Ashrafi, "Optical communications using orbital angular momentum beams," *Advances in Optics and Photonics*, vol. 7, p. 66, 2015.

[18] A. Forbes, A. Dudley, and M. McLaren, "Creation and detection of optical modes with spatial light modulators," *Advances in Optics and Photonics*, vol. 8, p. 200, 2016.

[19] H. Rubinsztein-Dunlop, A. Forbes, M. V. Berry, M. R. Dennis, D. L. Andrews, M. Mansuripur, C. Denz, C. Alpmann, P. Banzer, T. Bauer, E. Karimi, L. Marrucci, M. Padgett, M. Ritsch-Marte, N. M. Litchinitser, N. P. Bigelow, C. Rosales-Guzmán, A. Belmonte, J. P. Torres, T. W. Neely, M. Baker, R. Gordon, A. B. Stilgoe, J. Romero, A. G. White, R. Fickler, A. E. Willner, G. Xie, B. McMorran, and A. M. Weiner, "Roadmap on structured light," *Journal of Optics*, vol. 19, p. 013001, 2017.

[20] A. E. Willner, Y. Ren, G. Xie, Y. Yan, L. Li, Z. Zhao, J. Wang, M. Tur, A. F. Molisch, and S. Ashrafi, "Recent advances in high-capacity free-space optical and radio-frequency communications using orbital angular momentum multiplexing," *Philosophical Transactions of the Royal Society A*, vol. 375, p. 20150439, 2017.

[21] A. Mair, A. Vaziri, G. Weihs, and A. Zeilinger, "Entanglement of the orbital angular momentum states of photons.," *Nature*, vol. 412, p. 313, 2001.

[22] M. Krenn, M. Malik, M. Erhard, and A. Zeilinger, "Orbital angular momentum of photons and the entanglement of Laguerre–Gaussian modes," *Philosophical Transactions of the Royal Society A*, vol. 375, p. 20150442, 2017.

[23] M. Erhard, R. Fickler, M. Krenn, and A. Zeilinger, "Twisted photons: New quantum perspectives in high dimensions," *Light: Science and Applications*, vol. 7, p. 17111, 2018.

[24] A. Sit, F. Bouchard, R. Fickler, J. Gagnon-Bischoff, H. Larocque, K. Heshami, D. Elser, C. Peuntinger, K. Gunthner, B. Heim, C. Marquardt, G. Leuchs, R. W. Boyd, and E. Karimi, "High-dimensional intracity quantum cryptography with structured photons," *Optica*, vol. 4, p. 1006, 2017.

[25] M. Mirhosseini, O. S. Magaña-Loaiza, M. N. O'Sullivan, B. Rodenburg, M. Malik, M. P. Lavery, M. J. Padgett, D. J. Gauthier, and R. W. Boyd, "High-dimensional quantum cryptography with twisted light," *New Journal of Physics*, vol. 17, p. 033033, 2015.

[26] F. Bouchard, R. Fickler, R. W. Boyd, and E. Karimi, "High-dimensional quantum cloning and applications to quantum hacking," *Science Advances*, vol. 3, p. e1601915, 2017.

[27] M. J. Padgett and J. Courtial, "Poincaré-sphere equivalent for light beams containing orbital angular momentum.," *Optics Letters*, vol. 24, p. 430, 1999.

[28] J. S. Bell, "On the problem of hidden variables in quantum mechanics," World Scientific, 2001.

[29] J. F. Clauser, M. A. Horne, A. Shimony, and R. A. Holt, "Proposed Experiment to Test Local Hidden-Variable Theories," *Physical Review Letters*, vol. 23, p. 880, 1969.

[30] A. Aspect, J. Dalibard, and G. Roger, "Experimental Test of Bell's Inequalities Using Time- Varying Analyzers," *Physical Review Letters*, vol. 49, p. 1804, 1982.

[31] Z. Y. Ou and L. Mandel, "Violation of bell's inequality and classical probability in a two-photon correlation experiment," *Physical Review Letters*, vol. 61, p. 50, 1988.

[32] Y. H. Shih and C. O. Alley, "New type of einstein-podolsky-rosen-bohm experiment using pairs of light quanta produced by optical parametric down conversion," *Physical Review Letters*, vol. 61, p. 2921, 1988.

[33] T. E. Kiess, Y. H. Shih, A. V. Sergienko, and C. O. Alley, "Einstein-Podolsky-Rosen-Bohm experiment using pairs of light quanta produced by type-II parametric down-conversion," *Physical Review Letters*, vol. 71, p. 3893, 1993.

[34] P. G. Kwiat, K. Mattle, H. Weinfurter, A. Zeilinger, A. V. Sergienko, and Y. Shih, "New High-Intensity Source of Polarization-Entangled Photon Pairs," *Physical Review Letters*, vol. 75, p. 4337, 1995.

[35] Q. Zhan, "Cylindrical vector beams: from mathematical concepts to applications," *Advances in Optics and Photonics*, vol. 1, p. 1, 2009.

[36] B. Ndagano, I. Nape, M. A. Cox, C. Rosales-Guzman, and A. Forbes, "Creation and Detection of Vector Vortex Modes for Classical and Quantum Communication," *Journal of Lightwave Technology*, vol. 36, p. 292, 2018.

[37] B. Ndagano, H. Sroor, M. McLaren, C. Rosales-Guzmán, and A. Forbes, "Beam quality measure for vector beams," *Optics Letters*, vol. 41, p. 3407, 2016.

[38] G. Milione, H. I. Sztul, D. A. Nolan, and R. R. Alfano, "Higher-order Poincaré sphere, stokes parameters, and the angular momentum of light," *Physical Review Letters*, vol. 107, p. 053601, 2011.

[39] A. Holleczek, A. Aiello, C. Gabriel, C. Marquardt, and G. Leuchs, "Classical and quantum properties of cylindrically polarized states of light," *Optics Express*, vol. 19, p. 9714, 2011.

[40] G. Milione, S. Evans, D. A. Nolan, and R. R. Alfano, "Higher Order Pancharatnam-Berry Phase and the Angular Momentum of Light," *Physical Review Letters*, vol. 108, p. 190401, 2012.

[41] D. Naidoo, F. S. Roux, A. Dudley, I. Litvin, B. Piccirillo, L. Marrucci, and A. Forbes, "Controlled generation of higher-order Poincaré sphere beams from a laser," *Nature Photonics*, vol. 10, p. 327, 2016.

[42] S. Iwahashi, Y. Kurosaka, K. Sakai, K. Kitamura, N. Takayama, and S. Noda, "Higher-order vector beams produced by photonic-crystal lasers.," *Optics Express*, vol. 19, p. 119163, 2011.

[43] X. Cai, J. Wang, M. J. Strain, B. Johnson-Morris, J. Zhu, M. Sorel, J. L. O'Brien, M. G. Thompson, and S. Yu, "Integrated Compact Optical Vortex Beam Emitters," *Science*, vol. 338, p. 363, 2012.

[44] D. Naidoo, M. Fromager, K. Äit-Ameur, and A. Forbes, "Radially polarized cylindrical vector beams from a monolithic microchip laser," *Optical Engineering*, vol. 54, p. 111304, 2015.

[45] W. Shu, Y. Liu, Y. Ke, X. Ling, Z. Liu, B. Huang, H. Luo, and X. Yin, "Propagation model for vector beams generated by metasurfaces," *Optics Express*, vol. 24, p. 21177, 2016.

[46] P. Miao, Z. Zhang, J. Sun, W. Walasik, S. Longhi, N. M. Litchinitser, and L. Feng, "Orbital angular momentum microlaser," *Science*, vol. 353, p. 464, 2016.

[47] J. A. Davis, D. E. McNamara, D. M. Cottrell, and T. Sonehara, "Two-dimensional polarization encoding with a phase-only liquid-crystal spatial light modulator," *Applied Optics*, vol. 39, p. 1549, 2000.

[48] V. Arrizón, U. Ruiz, R. Carrada, and L. González, "Pixelated phase computer holograms for the accurate encoding of scalar complex fields," *Journal of the Optical Society of America A*, vol. 24, p. 3500, 2007.

[49] C. Rosales-Guzmán and A. Forbes, *How to shape light with spatial light modulators*. SPIE Press, 2017.

[50] M. Mirhosseini, O. S. Magaña-Loaiza, C. Chen, B. Rodenburg, M. Malik, and R. W. Boyd, "Rapid generation of light beams carrying orbital angular momentum," *Optics Express*, vol. 21, p. 30196, 2013.

[51] L. Gong, Y. Ren, W. Liu, M. Wang, M. Zhong, Z. Wang, and Y. Li, "Generation of cylindrically polarized vector vortex beams with digital micromirror device," *Journal of Applied Physics*, vol. 116, p. 183105, 2014.

[52] Y.-X. Ren, Z.-X. Fang, L. Gong, K. Huang, Y. Chen, and R.-D. Lu, "Digital generation and control of Hermite–Gaussian modes with an amplitude digital micromirror device," *Journal of Optics*, vol. 17, p. 125604, 2015.

[53] M. A. A. Neil, F. Massoumian, R. Juskaitis, and T. Wilson, "Method for the generation of arbitrary complex vector wave fronts.," *Optics Letters*, vol. 27, p. 1929, 2002.

[54] C. Maurer, A. Jesacher, S. Fürhapter, S. Bernet, and M. Ritsch-Marte, "Tailoring of arbitrary optical vector beams," *New Journal of Physics*, vol. 9, p. 78, 2007.

[55] I. Moreno, J. A. Davis, T. M. Hernandez, D. M. Cottrell, and D. Sand, "Complete polarization control of light from a liquid crystal spatial light modulator," *Optics Express*, vol. 20, p. 364, 2012.

[56] M. Beijersbergen, L. Allen, H. van der Veen, and J. Woerdman, "Astigmatic laser mode converters and transfer of orbital angular momentum," *Optics Communications*, vol. 96, p. 123, 1993.

[57] M. W. Beijersbergen, R. P. C. Coerwinkel, M. Kristensen, and J. P. Woerdman, "Helical-Wave-Front Laser-Beams Produced With a Spiral Phaseplate," *Optics Communications*, vol. 112, p. 321, 1994.

[58] Z. Bomzon, V. Kleiner, and E. Hasman, "Pancharatnam–Berry phase in space-variant polarization-state manipulations with subwavelength gratings.," *Optics Letters*, vol. 26, p. 1424, 2001.

[59] G. Biener, A. Niv, V. Kleiner, and E. Hasman, "Formation of helical beams by use of Pancharatnam–Berry phase optical elements," *Optics Letters*, vol. 27, p. 1875, 2002.

[60] S. Pancharatnam, *Generalized theory of interference and its applications - Part II. Partially coherent pencils*, vol. 44. 1956.

[61] M. V. Berry, "Quantal Phase Factors Accompanying Adiabatic Changes," *Proceedings of the Royal Society of London A*, vol. 392, p. 45, 1984.

[62] L. Marrucci, C. Manzo, and D. Papro, "Optical spin-to-orbital angular momentum conversion in inhomogeneous anisotropic media," *Physical Review Letters*, vol. 96, p. 163905, 2006.

[63] L. Marrucci, E. Karimi, S. Slussarenko, B. Piccirillo, E. Santamato, E. Nagali, and F. Sciarrino, "Spin-to-orbital conversion of the angular momentum of light and its classical and quantum applications," *Journal of Optics*, vol. 13, p. 064001, 2011.

[64] R. C. Devlin, A. Ambrosio, N. A. Rubin, J. P. B. Mueller, and F. Capasso, "Arbitrary spin-to–orbital angular momentum conversion of light," *Science*, vol. 358, p. 896, 2017.

[65] R. C. Devlin, M. Khorasaninejad, W. T. Chen, J. Oh, and F. Capasso, "Broadband high-efficiency dielectric metasurfaces for the visible spectrum.," *Proceedings of the National Academy of Sciences of the United States of America*, vol. 113, p. 10473, 2016.

[66] C. Rosales-Guzmán, B. Ndagano, and A. Forbes, "A review of complex vector light fields and their applications," *Journal of Optics*, vol. 20, p. 123001, 2018.

[67] T. Kaiser, D. Flamm, S. Schröter, and M. Duparré, "Complete modal decomposition for optical fibers using CGH-based correlation filters.," *Optics Express*, vol. 17, p. 9347, 2009.

[68] D. Flamm, D. Naidoo, C. Schulze, A. Forbes, and M. Duparré, "Mode analysis with a spatial light modulator as a correlation filter," *Optics Letters*, vol. 37, p. 2478, 2012.

[69] C. Schulze, A. Dudley, D. Flamm, M. Duparré, and A. Forbes, "Measurement of the orbital angular momentum density of light by modal decomposition," *New Journal of Physics*, vol. 15, p. 073025, 2013.

[70] B. Ndagano, R. Brüning, M. McLaren, M. Duparré, and A. Forbes, "Fiber propagation of vector modes," *Optics Express*, vol. 23, p. 17330, 2015.

[71] G. Milione, M. P. Lavery, H. Huang, Y. Ren, G. Xie, T. A. Nguyen, E. Karimi, L. Marrucci, D. A. Nolan, R. R. Alfano, *et al.*, "4× 20 gbit/s mode division multiplexing over free space using vector modes and a q-plate mode (de) multiplexer," *Optics Letters*, vol. 40, p. 1980, 2015.

[72] K. Vogel and H. Risken, "Determination of quasiprobability distributions in terms of probability distributions for the rotated quadrature phase," *Physical Review A*, vol. 40, p. 2847, 1989.

[73] E. Wigner, "On the quantum correction for thermodynamic equilibrium," *Physical Review*, vol. 40, p. 749, 1932.

[74] M. Hillery, R. F. O'Connell, M. O. Scully, and E. P. Wigner, "Distribution functions in physics: fundamentals," *Physics Reports*, vol. 106, p. 121, 1984.

[75] W. Band and J. L. Park, "The empirical determination of quantum states," *Foundations of Physics*, vol. 1, p. 133, 1970.

[76] A. Royer, "Measurement of quantum states and the wigner function," *Foundations of Physics*, vol. 19, p. 3, 1989.

[77] G. Birkhoff and J. Von Neumann, "The logic of quantum mechanics," *Annals of Mathematics*, p. 823, 1936.

[78] F. Mallet, M. Castellanos-Beltran, H. Ku, S. Glancy, E. Knill, K. Irwin, G. Hilton, L. Vale, and K. Lehnert, "Quantum state tomography of an itinerant squeezed microwave field," *Physical Review Letters*, vol. 106, p. 220502, 2011.

[79] M. Crispino, G. Di Giuseppe, F. De Martini, P. Mataloni, and H. Kanatsoulis, "Towards a fock-states tomographic reconstruction," *Fortschritte der Physik: Progress of Physics*, vol. 48, p. 589, 2000.

[80] A. Lvovsky and M. Raymer, *Continuous-Variable Quantum-State Tomography of Optical Fields and Photons*. World Scientific, 2007.

[81] D. Gross, Y.-K. Liu, S. T. Flammia, S. Becker, and J. Eisert, "Quantum state tomography via compressed sensing," *Physical Review Letters*, vol. 105, p. 150401, 2010.

[82] M. Ghalaii, M. Afsary, S. Alipour, and A. Rezakhani, "Quantum imaging as an ancilla-assisted process tomography," *Physical Review A*, vol. 94, p. 042102, 2016.

[83] K. J. Resch, P. Walther, and A. Zeilinger, "Full characterization of a three-photon greenberger-horne-zeilinger state using quantum state tomography," *Physical Review Letters*, vol. 94, p. 070402, 2005.

[84] V. Man'ko and O. Man'ko, "Spin state tomography," *Journal of Experimental and Theoretical Physics*, vol. 85, p. 430, 1997.

[85] K. Sanaka, K. Kawahara, and T. Kuga, "New high-efficiency source of photon pairs for engineering quantum entanglement," *Physical Review Letters*, vol. 86, p. 5620, 2001.

[86] W. J. Munro, D. F. James, A. G. White, and P. G. Kwiat, "Maximizing the entanglement of two mixed qubits," *Physical Review A*, vol. 64, p. 030302, 2001.

[87] D. F. V. James, P. G. Kwiat, W. J. Munro, and A. G. White, "Measurement of qubits," *Physical Review A*, vol. 64, p. 052312, 2001.

[88] Y. Nambu, K. Usami, Y. Tsuda, K. Matsumoto, and K. Nakamura, "Generation of polarization-entangled photon pairs in a cascade of two type-i crystals pumped by femtosecond pulses," *Physical Review A*, vol. 66, p. 033816, 2002.

[89] I. Marcikic, H. De Riedmatten, W. Tittel, H. Zbinden, and N. Gisin, "Long-distance teleportation of qubits at telecommunication wavelengths," *Nature*, vol. 421, p. 509, 2003.

[90] J. L. O'Brien, G. J. Pryde, A. G. White, T. C. Ralph, and D. Branning, "Demonstration of an all-optical quantum controlled-not gate," *Nature*, vol. 426, p. 264, 2003.

[91] T. Yamamoto, M. Koashi, Ş. K. Özdemir, and N. Imoto, "Experimental extraction of an entangled photon pair from two identically decohered pairs," *Nature*, vol. 421, p. 343, 2003.

[92] H. Häffner, W. Hänsel, C. Roos, J. Benhelm, M. Chwalla, T. Körber, U. Rapol, M. Riebe, P. Schmidt, C. Becher, *et al.*, "Scalable multiparticle entanglement of trapped ions," *Nature*, vol. 438, p. 643, 2005.

[93] D. Leibfried, E. Knill, S. Seidelin, J. Britton, R. B. Blakestad, J. Chiaverini, D. B. Hume, W. M. Itano, J. D. Jost, C. Langer, *et al.*, "Creation of a six-atom 'schrödinger cat'state," *Nature*, vol. 438, p. 639, 2005.

[94] T. Dunn, I. Walmsley, and S. Mukamel, "Experimental determination of the quantum-mechanical state of a molecular vibrational mode using fluorescence tomography," *Physical Review Letters*, vol. 74, p. 884, 1995.

[95] A. Aspect, P. Grangier, and G. Roger, "Experimental tests of realistic local theories via bell's theorem," *Physical Review Letters*, vol. 47, p. 460, 1981.

[96] A. Aspect, J. Dalibard, and G. Roger, "Experimental test of bell's inequalities using time-varying analyzers," *Physical Review Letters*, vol. 49, p. 1804, 1982.

[97] D. Bouwmeester, J.-W. Pan, K. Mattle, M. Eibl, H. Weinfurter, and A. Zeilinger, "Experimental quantum teleportation," *Nature*, vol. 390, p. 575, 1997.

[98] P. G. Kwiat, E. Waks, A. G. White, I. Appelbaum, and P. H. Eberhard, "Ultrabright source of polarization-entangled photons," *Physical Review A*, vol. 60, p. R773, 1999.

[99] A. Chefles, "12 quantum states: Discrimination and classical information transmission. a review of experimental progress," in *Quantum state estimation*, p. 467, Springer, 2004.

[100] Ö. Bayraktar, M. Swillo, C. Canalias, and G. Björk, "Quantum-polarization state tomography," *Physical Review A*, vol. 94, p. 020105, 2016.

[101] A. Mair, A. Vaziri, G. Weihs, and A. Zeilinger, "Entanglement of the orbital angular momentum states of photons," *Nature*, vol. 412, p. 313, 2001.

[102] J. Leach, B. Jack, J. Romero, M. Ritsch-Marte, R. Boyd, A. Jha, S. Barnett, S. Franke-Arnold, and M. Padgett, "Violation of a bell inequality in two-dimensional orbital angular momentum state-spaces," *Optics Express*, vol. 17, p. 8287, 2009.

[103] S. Gröblacher, T. Jennewein, A. Vaziri, G. Weihs, and A. Zeilinger, "Experimental quantum cryptography with qutrits," *New Journal of Physics*, vol. 8, p. 75, 2006.

[104] M. Mafu, A. Dudley, S. Goyal, D. Giovannini, M. McLaren, M. J. Padgett, T. Konrad, F. Petruccione, N. Lütkenhaus, and A. Forbes, "Higher-dimensional orbital-angular-momentum-based quantum key distribution with mutually unbiased bases," *Physical Review A*, vol. 88, p. 032305, 2013.

[105] D. Collins, N. Gisin, N. Linden, S. Massar, and S. Popescu, "Bell inequalities for arbitrarily high-dimensional systems," *Physical Review Letters*, vol. 88, p. 040404, 2002.

[106] A. Dada, J. Leach, G. Buller, M. Padgett, and E. Andersson, "Experimental high-dimensional two-photon entanglement and violations of generalized Bell inequalities," *Nature Physics*, vol. 7, p. 677, 2011.

[107] D. Giovannini, J. Romero, J. Leach, A. Dudley, A. Forbes, and M. J. Padgett, "Characterization of high-dimensional entangled systems via mutually unbiased measurements," *Physical Review Letters*, vol. 110, p. 143601, 2013.

[108] M. Cramer, M. B. Plenio, S. T. Flammia, R. Somma, D. Gross, S. D. Bartlett, O. Landon-Cardinal, D. Poulin, and Y.-K. Liu, "Efficient quantum state tomography," *Nature Communications*, vol. 1, p. 149, 2010.

[109] N. Bent, H. Qassim, A. Tahir, D. Sych, G. Leuchs, L. Sánchez-Soto, E. Karimi, and R. Boyd, "Experimental realization of quantum tomography of photonic qudits via symmetric informationally complete positive operator-valued measures," *Physical Review X*, vol. 5, p. 041006, 2015.

[110] A. I. Lvovsky and M. G. Raymer, "Continuous-variable optical quantum-state tomography," *Reviews of Modern Physics*, vol. 81, p. 299, 2009.

[111] M. Paris and J. Řeháček, "Quantum estimation theory," *Lecture Notes in Physics*, vol. 649, 2004.

[112] G. M. D'Ariano, M. G. Paris, and M. F. Sacchi, "Quantum tomography," *Advances in Imaging and Electron Physics*, vol. 128, p. 206, 2003.

[113] D. F. James, P. G. Kwiat, W. J. Munro, and A. G. White, "On the measurement of qubits," in *Asymptotic Theory Of Quantum Statistical Inference: Selected Papers*, p. 509, World Scientific, 2005.

[114] M. Schlosshauer, "Decoherence, the measurement problem, and interpretations of quantum mechanics," *Reviews of Modern physics*, vol. 76, p. 1267, 2005.

[115] S. Luo, "Using measurement-induced disturbance to characterize correlations as classical or quantum," *Physical Review A*, vol. 77, p. 022301, 2008.

[116] G. M. D'Ariano and H. Yuen, "Impossibility of measuring the wave function of a single quantum system," *Physical Review Letters*, vol. 76, p. 2832, 1996.

[117] A. G. White, D. F. James, P. H. Eberhard, and P. G. Kwiat, "Nonmaximally entangled states: Production, characterization, and utilization," *Physical Review Letters*, vol. 83, p. 3103, 1999.

[118] N. Brunner, S. Pironio, A. Acin, N. Gisin, A. A. Méthot, and V. Scarani, "Testing the dimension of hilbert spaces," *Physical Review Letters*, vol. 100, p. 210503, 2008.

[119] M. Hendrych, R. Gallego, M. Mičuda, N. Brunner, A. Acín, and J. P. Torres, "Experimental estimation of the dimension of classical and quantum systems," *Nature Physics*, vol. 8, p. 588, 2012.

[120] J. Ahrens, P. Badziag, A. Cabello, and M. Bourennane, "Experimental device-independent tests of classical and quantum dimensions," *Nature Physics*, vol. 8, p. 592, 2012.

[121] L. M. Johansen, "Quantum theory of successive projective measurements," *Physical Review A*, vol. 76, p. 012119, 2007.

[122] A. S. Agatston, W. R. Janowitz, F. J. Hildner, N. R. Zusmer, M. Viamonte, and R. Detrano, "Quantification of coronary artery calcium using ultrafast computed tomography," *Journal of the American College of Cardiology*, vol. 15, p. 827, 1990.

[123] L. P. Hughston, R. Jozsa, and W. K. Wootters, "A complete classification of quantum ensembles having a given density matrix," *Physics Letters A*, vol. 183, p. 14, 1993.

[124] K. Banaszek, G. D'ariano, M. Paris, and M. Sacchi, "Maximum-likelihood estimation of the density matrix," *Physical Review A*, vol. 61, p. 010304, 1999.

[125] S. R. White, "Density matrix formulation for quantum renormalization groups," *Physical Review Letters*, vol. 69, p. 2863, 1992.

[126] R. T. Thew, K. Nemoto, A. G. White, and W. J. Munro, "Qudit quantum-state tomography," *Physical Review A*, vol. 66, p. 012303, 2002.

[127] R. Schmied, "Quantum state tomography of a single qubit: comparison of methods," *Journal of Modern Optics*, vol. 63, p. 1744, 2016.

[128] B. Jack, J. Leach, H. Ritsch, S. Barnett, and M. Padgett, "Precise quantum tomography of photon pairs with entangled orbital angular momentum," *New Journal of Physics*, vol. 811, p. 103024, 2009.

[129] D. Flamm, C. Schulze, D. Naidoo, S. Schroter, A. Forbes, and M. Duparre, "All-digital holographic tool for mode excitation and analysis in optical fibers," *Journal of Lightwave Technology*, vol. 31, p. 1023, 2013.

[130] C. Schulze, S. Ngcobo, M. Duparré, and A. Forbes, "Modal decomposition without a priori scale information.," *Optics Express*, vol. 20, p. 27866, 2012.

[131] A. Dudley, Y. Li, T. Mhlanga, M. Escuti, and A. Forbes, "Generating and measuring nondiffracting vector Bessel beams.," *Optics Letters*, vol. 38, p. 3429, 2013.

[132] Y. Bromberg, Y. Lahini, R. Morandotti, and Y. Silberberg, "Quantum and Classical Correlations in Waveguide Lattices," *Physical Review Letters*, vol. 102, p. 253904, 2009.

[133] R. Keil, A. Szameit, F. Dreisow, M. Heinrich, S. Nolte, and A. Tünnermann, "Photon correlations in two-dimensional waveguide arrays and their classical estimate," *Physical Review A*, vol. 81, p. 023834, 2010.

[134] R. Keil, F. Dreisow, M. Heinrich, A. Tünnermann, S. Nolte, and A. Szameit, "Classical characterization of biphoton correlation in waveguide lattices," *Physical Review A*, vol. 83, p. 013808, 2011.

[135] B. Ndagano, B. Perez-Garcia, F. S. Roux, M. McLaren, C. Rosales-Guzman, Y. Zhang, O. Mouane, R. I. Hernandez-Aranda, T. Konrad, and A. Forbes, "Characterizing quantum channels with non-separable states of classical light," *Nature Physics*, vol. 13, p. 397, 2017.

[136] M. McLaren, T. Konrad, and A. Forbes, "Measuring the nonseparability of vector vortex beams," *Physical Review A*, vol. 92, p. 023833, 2015.

[137] H. Sroor, N. Lisa, D. Naidoo, I. Litvin, and A. Forbes, "Purity of vector vortex beams through a birefringent amplifier," *Physical Review Applied*, vol. 9, p. 044010, 2018.

[138] M. Jiang, S. Luo, and S. Fu, "Channel-state duality," *Physical Review A*, vol. 87, p. 022310, 2013.

[139] W. Dür, M. Hein, J. I. Cirac, and H.-J. Briegel, "Standard forms of noisy quantum operations via depolarization," *Physical Review A*, vol. 72, p. 052326, 2005.

[140] L. Allen, M. W. Beijersbergen, R. J. C. Spreeuw, and J. P. Woerdman, "Orbital angular momentum of light and the transformation of Laguerre-Gaussian laser modes," *Physical Review A*, vol. 45, p. 8185, 1992.

[141] W. K. Wootters, "Entanglement of formation and concurrence.," *Quantum Information & Computation*, vol. 1, p. 27, 2001.

[142] T. Konrad, F. de Melo, M. Tiersch, C. Kasztelan, A. Aragão, and A. Buchleitner, "Evolution equation for quantum entanglement," *Nature Physics*, vol. 4, p. 99, 2008.

[143] F. S. Roux, T. Wellens, and V. N. Shatokhin, "Entanglement evolution of twisted photons in strong atmospheric turbulence," *Physical Review A*, vol. 92, p. 012326, 2015.

[144] G. Milione, T. A. Nguyen, J. Leach, D. A. Nolan, and R. R. Alfano, "Using the nonseparability of vector beams to encode information for optical communication," *Optics Letters*, vol. 40, p. 4887, 2015.

[145] J. C. Leader, "Atmospheric propagation of partially coherent radiation*," *Journal of the Optical Society of America*, vol. 68, p. 175, 1978.

[146] L. C. Andrews and R. L. Phillips, *Laser Beam Propagation through Random Media*, vol. 1. SPIE, 2nd ed., 2005.

[147] A. H. Ibrahim, F. S. Roux, M. McLaren, T. Konrad, and A. Forbes, "Orbital-angular-momentum entanglement in turbulence," *Physical Review A*, vol. 88, p. 012312, 2013.

[148] V. D'Ambrosio, E. Nagali, S. P. Walborn, L. Aolita, S. Slussarenko, L. Marrucci, and F. Sciarrino, "Complete experimental toolbox for alignment-free quantum communication," *Nature Communications*, vol. 3, p. 961, 2012.

[149] O. J. Farías, V. D'Ambrosio, C. Taballione, F. Bisesto, S. Slussarenko, L. Aolita, L. Marrucci, S. P. Walborn, and F. Sciarrino, "Resilience of hybrid optical angular momentum qubits to turbulence," *Scientific Reports*, vol. 5, p. 8424, 2015.

[150] C. H. Bennett and G. Brassard, "Quantum Cryptography: Public Key Distribution, and Coin-Tossing," *International Conference on Computers, Systems, and Signal Processing*, vol. 1, p. 175, 1984.

[151] D. Bruß, "Optimal Eavesdropping in Quantum Cryptography with Six States," *Physical Review Letters*, vol. 81, p. 3018, 1998.

[152] C. Bennett, G. Brassard, C. Crepeau, and U. Maurer, "Generalized privacy amplification," *IEEE Transactions on Information Theory*, vol. 41, p. 1915, 1995.

[153] A. Ferenczi and N. Lütkenhaus, "Symmetries in quantum key distribution and the connection between optimal attacks and optimal cloning," *Physical Review A*, vol. 85, p. 052310, 2012.

[154] C. Paterson, "Atmospheric turbulence and orbital angular momentum of single photons for optical communication," *Physical Review Letters*, vol. 94, p. 153901, 2005.

[155] C. Gopaul and R. Andrews, "The effect of atmospheric turbulence on entangled orbital angular momentum states," *New Journal of Physics*, vol. 9, p. 94, 2007.

[156] G. A. Tyler and R. W. Boyd, "Influence of atmospheric turbulence on the propagation of quantum states of light carrying orbital angular momentum," *Optics Letters*, vol. 34, p. 142, 2009.

[157] B. Ndagano, I. Nape, B. Perez-Garcia, S. Scholes, R. I. Hernandez-Aranda, T. Konrad, M. P. J. Lavery, and A. Forbes, "A deterministic detector for vector vortex states," *Scientific Reports*, vol. 7, p. 13882, 2017.

[158] J. A. Anguita, M. A. Neifeld, and B. V. Vasic, "Turbulence-induced channel crosstalk in an orbital angular momentum-multiplexed free-space optical link," *Applied Optics*, vol. 47, p. 2414, 2008.

[159] B. Rodenburg, M. P. J. Lavery, M. Malik, M. N. O'Sullivan, M. Mirhosseini, D. J. Robertson, M. Padgett, and R. W. Boyd, "Influence of atmospheric turbulence on states of light carrying orbital angular momentum," *Optics Letters*, vol. 37, p. 3735, 2012.

[160] C. Chen, H. Yang, S. Tong, and Y. Lou, "Changes in orbital-angular-momentum modes of a propagated vortex Gaussian beam through weak-to-strong atmospheric turbulence," *Optics Express*, vol. 24, p. 6959, 2016.

[161] R. Neo, M. Goodwin, J. Zheng, J. Lawrence, S. Leon-Saval, J. Bland-Hawthorn, and G. Molina-Terriza, "Measurement and limitations of optical orbital angular momentum through corrected atmospheric turbulence," *Optics Express*, vol. 24, p. 2919, 2016.

[162] M. Agnew, J. Leach, M. McLaren, F. S. Roux, and R. W. Boyd, "Tomography of the quantum state of photons entangled in high dimensions," *Physical Review A*, vol. 84, p. 062101, 2011.

[163] W. Li, G. Feng, and S. Zhou, "The M^2 factor matrix of a paraxial Laguerre–Gaussian beam," *Journal of Modern Optics*, vol. 60, p. 704, 2013.

[164] E. Kovlakov, S. Straupe, and S. Kulik, "Quantum state engineering with twisted photons via adaptive shaping of the pump beam," *arXiv:1807.09804*, 2018.

[165] S.-L. Liu, Z.-Y. Zhou, S.-K. Liu, Y.-H. Li, Y. Li, Chen-Yang, Z.-h. Xu, Z.-d. Liu, G.-C. Guo, and B.-S. Shi, "Coherent manipulation of a three-dimensional maximally entangled state," *arXiv:1807.07257*, 2018.

[166] M. Erhard, M. Malik, and A. Zeilinger, "A quantum router for high-dimensional entanglement," *Quantum Science and Technology*, vol. 2, p. 014001, 2017.

[167] W. K. Wootters and W. H. Zurek, "A single quantum cannot be cloned," *Nature*, vol. 299, p. 802, 1982.

[168] C. H. Bennett, H. J. Bernstein, S. Popescu, and B. Schumacher, "Concentrating partial entanglement by local operations," *Physical Review A*, vol. 53, p. 2046, 1996.

[169] R. T. Thew and W. J. Munro, "Entanglement manipulation and concentration," *Physical Review A*, vol. 63, p. 030302, 2001.

[170] P. G. Kwiat, S. Barraza-Lopez, A. Stefanov, and N. Gisin, "Experimental entanglement distillation and 'hidden'non-locality," *Nature*, vol. 409, p. 1014, 2001.

[171] N. A. Peters, J. B. Altepeter, D. Branning, E. R. Jeffrey, T.-C. Wei, and P. G. Kwiat, "Maximally entangled mixed states: creation and concentration," *Physical Review Letters*, vol. 92, p. 133601, 2004.

[172] A. Vaziri, J.-W. Pan, T. Jennewein, G. Weihs, and A. Zeilinger, "Concentration of Higher Dimensional Entanglement: Qutrits of Photon Orbital Angular Momentum," *Physical Review Letters*, vol. 91, p. 227902, 2003.

[173] C. K. Hong, Z. Y. Ou, and L. Mandel, "Measurement of subpicosecond time intervals between two photons by interference," *Physical Review Letters*, vol. 59, p. 2044, 1987.

[174] Y. Zhang, S. Prabhakar, C. Rosales-Guzmán, F. S. Roux, E. Karimi, and A. Forbes, "Hong-Ou-Mandel interference of entangled Hermite-Gauss modes," *Physical Review A*, vol. 94, p. 033855, 2016.

[175] Y. Zhang, F. S. Roux, T. Konrad, M. Agnew, J. Leach, and A. Forbes, "Engineering two-photon high-dimensional states through quantum interference," *Science Advances*, vol. 2, p. e1501165, 2016.

[176] Y. Zhang, M. Agnew, T. Roger, F. S. Roux, T. Konrad, D. Faccio, J. Leach, and A. Forbes, "Simultaneous entanglement swapping of multiple orbital angular momentum states of light," *Nature Communications*, vol. 8, p. 632, 2017.

[177] S. Prabhakar, C. Mabena, T. Konrad, and F. S. Roux, "Turbulence and the Hong-Ou-Mandel effect," *Physical Review A*, vol. 97, p. 013835, 2018.

[178] M. Malik, M. O'Sullivan, B. Rodenburg, M. Mirhosseini, J. Leach, M. P. J. Lavery, M. J. Padgett, and R. W. Boyd, "Influence of atmospheric turbulence on optical communications using orbital angular momentum for encoding.," *Optics Express*, vol. 20, p. 13195, 2012.

[179] H. J. Kimble, "The quantum internet," *Nature*, vol. 453, p. 1023, 2008.

[180] G. C. G. Berkhout, M. P. J. Lavery, J. Courtial, M. W. Beijersbergen, and M. J. Padgett, "Efficient Sorting of Orbital Angular Momentum States of Light," *Physical Review Letters*, vol. 105, p. 153601, 2010.

[181] R. Fickler, R. Lapkiewicz, S. Ramelow, and A. Zeilinger, "Quantum entanglement of complex photon polarization patterns in vector beams," *Physical Review A*, vol. 89, p. 060301, 2014.

[182] M. P. J. Lavery, D. J. Robertson, A. Sponselli, J. Courtial, N. K. Steinhoff, G. A. Tyler, A. E. Willner, and M. J. Padgett, "Efficient measurement of an optical orbital-angular-momentum spectrum comprising more than 50 states," *New Journal of Physics*, vol. 15, p. 013024, 2013.

[183] A. Dudley, T. Mhlanga, M. Lavery, A. McDonald, F. S. Roux, M. Padgett, and A. Forbes, "Efficient sorting of Bessel beams," *Optics Express*, vol. 21, p. 165, 2013.

[184] T. H. Lu, T. D. Huang, J. G. Wang, L. W. Wang, and R. R. Alfano, "Generation of flower high-order Poincaré sphere laser beams from a spatial light modulator," *Scientific Reports*, vol. 6, p. 39657, 2016.

[185] J. Kim, Y. Li, M. N. Miskiewicz, C. Oh, M. W. Kudenov, and M. J. Escuti, "Fabrication of ideal geometric-phase holograms with arbitrary wavefronts," *Optica*, vol. 2, p. 958, 2015.

[186] N. J. Cerf, M. Bourennane, A. Karlsson, and N. Gisin, "Security of Quantum Key Distribution Using d-Level Systems," *Physical Review Letters*, vol. 88, p. 127902, 2002.

[187] G. Ruffato, M. Massari, and F. Romanato, "Diffractive optics for combined spatial- and mode- division demultiplexing of optical vortices: design, fabrication and optical characterization," *Scientific Reports*, vol. 6, p. 24760, 2016.

[188] M. A. Cox, C. Rosales-Guzmán, M. P. J. Lavery, D. J. Versfeld, and A. Forbes, "On the resilience of scalar and vector vortex modes in turbulence," *Optics Express*, vol. 24, p. 18105, 2016.

[189] V. D'Ambrosio, G. Carvacho, F. Graffitti, C. Vitelli, B. Piccirillo, L. Marrucci, and F. Sciarrino, "Entangled vector vortex beams," *Physical Review A*, vol. 94, p. 030304, 2016.